Computer Simulation Studies of Structure and Ion Transport in NASICON Fast Ion Solids

by

Supriya Roy

A thesis
submitted for the degree of

Doctor of Philosophy

Department of Physics
Indian Institute of Technology Guwahati
Guwahati 781039, India

September 2013

Computer Simulation Studies of Structure and Ion Transport in NASICON Fast Ion Solids

by

Supriya Roy

A thesis
submitted for the degree of
Doctor of Philosophy

Supervisor:
Dr. Padma Kumar Padmanabhan

Department of Physics
Indian Institute of Technology Guwahati
Guwahati 781039, India

September 2013

Certificate

It is certified that the work contained in the thesis entitled "*Computer Simulation Studies of Structure and Ion Transport in NASICON Fast Ion Solids*" by Mr. Supriya Roy, a student of the Department of Physics, IIT Guwahati was carried out under my supervision and has not been submitted elsewhere for award of any degree.

Dr. Padma Kumar Padmanabhan

Dedicated to my parents

Acknowledgements

First of all I want to thank my supervisor Dr. Padma Kumar Padmanabhan. It has been a wonderful and memorable experience to work under his guidance. He always encouraged my efforts and motivated me in positive directions in Ph.D life. I appreciate the way he made sure that I was making my progress in my research work without putting any extra pressure on me. He helped me to resolve the problems regarding my research works and never minded even if it was very ordinary. He always gave me freedom to work and encouraged me if I try something new, which gave me a lots of confidence. He helped me to develop right approach towards research work and advised me to never get disappointed with the negative results as there may be some important understandings behind those results. Apart form that he is a nice human being. His frankness, ego-less attitude always allowed me to discuss any academic or non-academic problems. I am grateful to him for his patience in some phase of my research life when I had really tough times.

I am thankful to my doctoral committee members, Dr. S. Ghosh, Prof. A Srinivasan, Dr. A. N. Panda and Dr. C. Y. Kadolkar for their valuable support and suggestions during my research period.

I would like to thank Basab Purakayasthya along with all other technical assistants of our department for the technical supports which they have provided whenever I needed.

I wish to thank the present and past Physics Department Heads for supplying the full support and facilities at their best. I extend my whole hearted thanks to all the faculty members in the Physics Department who supported me in several ways during my research period. Many of them helped me to improve my management skills by allowing me to involve in various scientific events they have organized. I am thankful to IIT Guwahati for providing me not only with the financial assistantship but also with rigorous sports facilities, nice accommodations and a peaceful campus which always helped to concentrate better.

I wish to thank all of my batchmates, seniors and juniors who were always supportive. I want to specially mention my dear seniors Dr. Meera V., Dr. Biswanath Dutta, Dr. Poulumi Dey, Dr. Jahir Abbas Ahmed and Dr. Vindhyawasini Prasad for giving valuable tips and mental support in my initial Ph.D days. They helped me a lot to develop my skill on Linux system and in more other issues. I wish to thank all of my friends from IITG with

whom I played, shared light moments, jokes, arguments over non academic issues which kept me refreshed and energetic. I would like to thank all of my group members Kartik Sau, Krishnanjan Pramanik and Omkar Tripathy. They have been always very close my to heart. And the rigorous discussions with them on our research field, helped me to clear my concept and gaining more insight into the subject. Special thanks to my dear friends Bappaditya Pal, Avijit Ghosh, Pratibhamoy Das, Utsab Guharoy and Kausik sen with them I shared very enjoyable and memorable moments and their mental support in my tough times always kept me refreshed for the next working day.

Finally and foremost I wish my gratitude and thanks to my parents who have been the inspiration and core strength of my life. Without them this Ph.D thesis would have been never possible. I am fortunate to have them. From my beginning of the life I have been grown up with their deep love and care. Their moral lessons and the supports in every fields made me what I am today.

Contents

Chapter 1

Introduction

Global energy security and environment conservation are among the immediate challenges before the humanity. The cost-effective natural reserves of petroleum are drying up. More importantly, the indiscriminate use of natural gas over the last hundred years or so, as we realize now, has taken a heavy toll on our environment in the form of global warming. This calls for stringent measures to cut down on our carbon footprint on environment, a sizable part of which owes to automobile emission. Thus, the design and development of sustainable and green portable energy devices to replace natural gas forms one of the major challenges before scientists. Use of electrochemical energy devices is under serious consideration to replace for fossil fuels. The design and fabrication of improvised portable energy sources – secondary energy storage devices such as batteries and primary sources such as fuel cells – relies on fast ion transport in condensed states of matter. The study of fast ion conduction (or, superionic conductors), thus, forms one of the most vibrant areas of present day research.

In electrochemical devises electrical energy is generated by conversion of chemical energy through redox reaction. The anode of a battery is the reducing agent and serves as electron donors while the cathode serves as electron acceptor. The electrolyte is a pure ionic conductor that separates the cathode and anode. While in operation electronic current flows through the external circuit delivering power to an electrical devices, the mobile ions present in the electrolyte carries the current to complete the circuit. Electrolyte can be of liquid or solid phase.

Liquid electrolytes have no regular long range orders consists entirely of mobile ions while solid electrolytes have a rigid matrix in which one or more species of mobile ions diffusing through them. The recent studies of fast ion conduction relies largely on solid electrolytes owing to their high energy densities, leak resistance, less corrosive nature, high thermal and chemical stabilities.

Fast ion conduction has been realized in a variety of solid matrices, such as crystalline solids, glassy materials, polymeric systems, plastic crystals, thin films, etc. The ionic conductivity of fast ion conductors are typically in the range of 10^{-3} to 10^{-1} S/cm, while their electronic conductivity are of the order of 10^{-9} S/cm which is practically negligible. There are fast ion conductors which exhibit electronic conductivity as well (for example, Li-intercalated graphite and Li_xCoO_2), called mixed conductors, they find applications in electrode materials. Several excellent reviews and perspectives on solid electrolytes have recently appeared [1–26].

There are a variety of crystalline fast ion conductors with different mobile ions that can be classified depending on the type of carriers, cationic conductors (Li^+, Na^+, Ag^+, H^+ etc.) and anionic conductors (F^- and O^{2-}). The following sections briefly review some of recent advances in the field of fast ion conduction in crystalline materials.

1.1 F^- ion conductors

Fluoride compounds forms an important class of anionic conductors that find rich technological importance in various fields. Fluoride material shows high ionic conductivity at lower temperatures due to its small size, negligible electronic conductivity and finds its application as solid electrolyte material [27–29]. It has been used as electrode material for Li batteries also for its high electronegative values [30]. Rare earth containing fluoride systems also have been used as solid electrolytes of power and sensor applications depending on their ionic conductivities[31–33].

Fluoride materials such as β-PbF_2[34], CaF_2[35], SnF_2[36] crystallizes in cubic fluorite structure (CaF_2 structure) and exhibit high ionic conductivity with the presence of extensive intrinsic disorder of the anion sub-lattice. There are numerous fluoride conductors synthesized by doping these bivalent fluoride materials. In most of these cases, the homogeneous doping of bivalent fluoride material by monovalent anion deficit systems such as KF[36], NaF[34] etc. or trivalent anion excess systems such as LaF_3[34] enhanced the conductivity of the system and also influence the conductivity behavior with temperature. SnF_2 is reported to show one order in magnitude more conductivity when doped with 10% KF and leads to a α to γ superionic phase transition at 443 K[36]. PbF_2 also shows higher conductivity for both cases while doped with monovalent KF or trivalent LaF_3[34].

There are fluoride based composite materials such as $NaSn_2F_5$ when doped with Al_2O_3 fillers show an enhancement in conductivity[37]. The enhancement of conductivity depends on the factors like size, concentration and nature of the filler particles as well as the method of preparation. In the study of $NaSn_2F_5$ study it was shown that the host conductor dispersed with 0.6 micron size alumina particle shows more than one order of magnitude improvement in conductivity compared to the alumina particle size of 1 micron. There are also other composite electrolytes for example PbF_2 dispersed with SiO_2 particle[34], CaF_2 dispersed with Al_2O_3 [35] has been studied. They showed that the conductivity increases with the concentration and decreases with the sizes of filler particles. Various ternary fluoride materials such as KSn_2F_5[38], $RbSn_2F_5$[39], $PbSnF_4$[40], $KBiF_4$[41] and $TiZrF_5$[42] have also been shown to have very good electronic conductivity at ambient temperature. Among them $RbSn_2F_5$ shows excellent ionic conductivity about 0.125 S/cm at 473 K[39].

Fluoride materials has also been used as thin films for low power applications. However mostly studied fluoride systems for thin film applications are LaF_3[43], and BaF_2[44]. It is also reported that few fluoride materials such as LaF_3[45], SnF_2[46], CaF_2 [47] shows consistently one or two orders higher conductivities for lower crystallite size. For example SnF_2 of two different crystallite sizes 81 nm and 36 nm shows conductivity value 3.74×10^{-6} and 1.61×10^{-6} S/cm respectively[46]. The fractional cross sectional areas of grain boundaries

increases for nano-crystalline and this may be the reason for high conductivity value. More recently multilayer heterostructures of BaF_2 and CaF_2 have been proposed as potential candidates for solid electrolytes. In this study the F^- conductivity enhanced by increasing the periodicity of alternating layers. The F^- ions of BaF_2 transfers to the adjacent CaF_2 through the interfaces which create vacancy in BaF_2 resulting increment in charge carrier concentration [11, 48].

Several molecular dynamics (MD) studies have been reported on the different fluoride ion conductors. Rahman carried out MD simulation on CaF_2 using rigid sphere model[49]. Then Lindan and Gillan[50] used shell model MD simulation on CaF_2. Results from the two models are nearly identical. Both studies the pair distribution functions show decrease in the peak height and increase in the population around the octahedral position which indicates a superionic transition. The diffusion coefficient of the fluorine ion was also calculated which shows good agreement with experimental data. The result of the shell model concludes that the electronic polarizability of anion does not affect the fluorine diffusion significantly. Molecular dynamic simulation were carried out also on the BaF_2[51]. This study showed a phase transition around a temperature 1200 K. The diffusion coefficient and Debye-Waller factors are calculated which showed good agreement with experiment.

Rigid ion model based MD simulations were performed on PbF_2 in temperature range of 450 K to 1000 K [52, 53]. The diffusion coefficients were calculated and show good agreement with the nuclear magnetic resonance data. NPT-MD simulations (constant pressure, constant temperature and constant number of particles) were performed on the perovskite type fluoride ion conducting of KAF_3 family where ($A = Mn,\ Zn$ or Ca). The study shows that only the Ca based system $KCaF_3$ has good ionic conductivity. The study concludes that the ion migration in these materials occurs through the vacancy mechanism of correlated jumps of interstitial ions.

1.2 O^{2-} ion conductors

Oxide ion conductors are used extensively in solid electrolyte fuel cells (SOFC)[15, 54]. SOFC converts chemical energy into electrical energy. The electrodes of SOFC are separated by electrolyte which allow transfer of either oxide or proton conductors. Normally SOFC operates at temperature range $800-1000^{\circ}C$. The fabrication of SOFC which can work at a lower temperature range $500-700^{\circ}C$ remains an open challenge. One of the most popular class of oxide ion conductors has the chemical formula AO_2 which typically stabilize in fluorite type structure where A is a tetravalent cation. One of the best known fluorite based conductor is acceptor doped ZrO_2[8, 15, 55]. Pure ZrO_2 is not a good ionic conductor and stabilizes in fluorite structure only at temperature higher than $2300^{\circ}C$ [56]. So divalent or trivalent cation are doped into cation sublattice of ZrO_2 to stabilize the fluorite structure in lower temperature. This also increases the concentration of oxygen vacancies in the lattice resulting in an enhancement of conductivity. Calcium stabilized zirconia(CaSZ), Yattria stabilized zirconia (YSZ) and Scandium stabilized zirconia (ScSZ)[57] are among the typical acceptor doped zirconia which show good ionic conductivity in the temperature range above $700^{\circ}C$[56]. Among them YSZ shows best ionic conductivity and studied widely for applications in SOFC. But its use is limited because of high operating temperatures $(800-1000^{\circ}C)$[58].

Doped CeO_2 is another class of fluorite type oxide ion conductor. Gd_2O_3 and Sm_2O_3 are the well known dopants used in CeO_2. These materials exhibit higher ionic conductivities at low temperature range $500-700^{\circ}C$ which is advantageous for use as electrolyte material in SOFC[59–61]. But one of the main disadvantages of these materials is the presence of non-negligible electronic conductivity above $600^{\circ}C$. Despite the reduction in cell voltage due to the electronic conduction gadolinia substituted ceria shows enough ionic conductivity to be used as electrolyte. Attempts have been made to mix zirconia and ceria together to achieve better ionic conductors having high conductivity like ceria with the strong chemical and mechanical stability of zirconia [62].

$\delta - Bi_2O_3$ is another material which exhibits high oxygen ion conductivity and stabilizes in the fluorite based structure[63, 64]. This material possesses high fraction of oxygen deficiency. Again the high conducting δ phase of this material is stable at a temperature higher than $750^{\circ}C$. Doping through rare earth materials by Y^{3+}, Dy^{3+} and Er^{3+} in combination with supervalent cations like Nb, W have been reported to produce stable structure at low temperature [65, 66].

Another fluorite structure related oxide ion conductor is pyrochlore structure with general formula $A_2B_2O_7$[67]. Two most widely studied pyrochlore structure are $Gd_x(Ti_{1-x}Zr_x)_2O_7$, $Gd_{2-y}Ln_yZr_2O_7$ where $Ln = Sm,\ Nd$ and La [68, 69]. However these materials exhibit conductivity lower than YSZ or gadolinium based ceria and hence are not used in practical SOFC.

There are another class of important oxide ion conductors which stabilize in perovskite structure with general formula ABO_3 where A cation is sitting on the center of the cube surrounded by twelve anions and B cations are sitting on the corner of the cube making an octahedral arrangement with anion. Sr and Mg doped $LaGaO_3$ with general formula $La_{1-x}Sr_xGa_{1-y}Mg_yO_{3-\delta}$ (LSGM) show very good oxide ion conduction[70–72]. LSGM shows better conductivity than YSZ at low temperature also. The uses of these materials however restricted by the difficulty of obtaining them in a single phase, volatility of gadolinium at high temperatures and its tendency to react with Ni which is often used as the anode.

$La_2Mo_2O_9$ discovered recently also shows fast oxide ion conduction [73]. $La_2Mo_2O_9$ (LAMOX). exhibits a phase transition from very low conducting α monoclinic to high conducting cubic phase at $580^{\circ}C$. Doping of the La site of the pure LAMOX structure by alkali ions (K and Rb) or alkali earth metals ($Ca,\ Ba$ and Sr) stabilizes the cubic structure at room temperature without much reduction in conductivity[74, 75]. Doping of rare earth metals $Gd,\ Y$ and Nb in La site along with W doping in Mo site show better oxygen ion diffusion in LAMOX than those of YSZ and LSGM[76].

As mentioned earlier Yattria stabilized zirconia shows high oxygen ion conductivity above temperature $700^{\circ}C$. The conductivity of this series $(ZrO_2)_{1-x}(Y_2O_3)_x$ increases initially with

the doping concentration and reaches its maximum value for $\approx$ 8 *mol* % then decreases for higher concentration of dopant. To analysis the dependence of conductivity upon the concentration of dopant and the pattern of oxygen vacancy distribution, molecular dynamics (MD) simulations have been carried out on this series[77, 78]. This study also shows a maximum of diffusivity for 10 *mol* % of Y_2O_3 and decreases for the higher Y_2O_3 concentration. Oxide ion concentration increases in the center of tetrahedral site with more number of Y^{3+} ions at its vertices. The oxygen ion pathway has been analyzed in detail. The study analyzes that in low impurity concentration, the ratio of forward and backward jumps and diffusion jumps increases with number of Y^{3+} atoms. But for higher Y^{3+} concentration the contribution from local forward-backward jumps increases which reduces the total diffusion.

Molecular dynamics simulations have been carried out on the doped ceria compound $Ce_{1-x}M_xO_{(2-\frac{1}{2})x}$ where $M = La,\ Gd$ or Y for $0 \leq x \leq 0.3$) [79, 80]. The study analyzes the diffusion coefficient of this series across different concentration of dopant x. The study shows the highest conductivity for Gd doped system. The conductivity variation with composition x for a particular dopant shows that the conductivity increases and reaches a maximum for a certain value of dopant concentration and then decreases. This trend is similar for all the three dopants studied. In this study the higher rate of backward jumps of oxygen is detected as the reason for decrease in conductivity for higher concentration of dopant.

Molecular dynamics simulations on the ABO_3 type perovskite structured material $LaGaO_3$ have been carried out[81, 82]. These materials have higher ionic conductivity than zirconia doped materials. The study proposed that the large free volume and a large value of the factor, $T = \frac{r_A+r_O}{\sqrt{2}(r_B+r_O)} \approx 0.96$ is responsible for the higher value of the conductivity in perovskite structured material. They studied different series of materials by varying the composition at A and B sites which showed maximum conductivity for the compounds for which $T \approx 0.96$.

1.3 Proton conductors

Proton conduction was first discovered by Iwahara et al. in doped barium and strontium cerates[83, 84]. These materials usually stabilize in perovskite type structure. The requirement of a good proton conduction is identified as, oxygen ion vacancies in the structure and dissociative absorption in the surface. A water molecule dissociates into a hydroxide ion and a proton. Hydroxide ion occupies the vacant site and leaving mobile proton which conducts electricity.

Cerates and zirconates are important class of proton conductors. Many materials have been synthesized doping cerates and zirconates and their ionic conductivites are measured as a as a function of doping concentration. $BaCe_{0.80}Y_{0.2}O_{2.9}$ shows high proton conduction[85]. $BaCeO_3$ by itself shows poor chemical stability when used in SOFCs, it reacts with CO_2 and decomposes into barium carbonate and cerium oxide. $BaZrO_3$ shows much better chemical stability and high intrinsic proton conduction than $BaCeO_3$. Cerates and Composites of cirates and zirconates exhibit high proton conductivity and better chemical stability. This has been one of the most promising class of proton conductors[86, 87].

Some oxygen deficient materials with perovskite structure are reported to show good proton conduction. $Ba_2In_2O_5$ is one of this type of materials. The presence of intrinsic oxygen vacancies permits adequate amount of proton conduction in the structure. $(Ba_{1-x}La_x)_2In_2O_{5+x}$ composition shows higher proton conduction with the increment of La [88]. It reaches the highest conductivity for composition $x = 0.1$ of $1.12 \times 10^{-5}\ S/cm$ at $400^{\circ}C$. Another material $Ba_2(In_{1-x}Ti_x)_2O_{5+x}$ shows good ionic conductivity $1.1 \times 10^{-3}\ S/cm$ for composition $x = 0.2$ at temperature $450^{\circ}C$[89].

Ca and Sr doped $LaPO_4$ shows predominant proton conduction at $800^{\circ}C$ though the magnitude is not very high 6×10^{-5} and $3 \times 10^{-4}\ S/cm$, respectively[90, 91]. These phosphate systems consists of a chain of corner sharing PO_4 tetrahedra separated by layers of rare earth materials.

$CsHSO_4$ are CsH_2PO_4 are the solid acids which show high proton conduction at relatively moderate temperature. This material has advantages of anhydrous proton transport and good thermal stability upto ($250^{\circ}C$)[92, 93]. Rare earth doped orthoniobates and orthotantalates materials of the general formula $RE_{1-x}A_xMO_4$, where $RE = La,\ Gd,\ Nb,\ Tb,\ Er$ and Y, $M = Nb$ or Ta and ($A = Ca,\ Ba,$ or Sr) also show good proton conduction. Among different compositions $La_{0.99}Ca_{0.1}NbO_{4-\delta}$ is known to be one of the best conductors of this series. These class of materials go through a structural phase transition from a low temperature monoclinic ($I2/c$) to a high temperature tetragonal ($I4_1/a$) structure associated with a reduction in activation energy depending on the composition. These materials show pure protonic ion conductivities up to temperature $700^{\circ}C$, of the order of $10^{-3}S/cm$ [94].

Classical atomistic molecular dynamics (MD) simulations were performed on $CsHSO_4$ to explore the dynamic behavior of the sublattice and protons[95]. This study suggests that the transport of proton occurs through one oxygen atom to its neighboring tetrahedral oxygen atom along with the reorientation of SO^4 tetrahedra in a structural reorganization. The diffusion coefficient of proton has been measured in good agreement with experiments.

Quantum molecular dynamics has been carried out on the high temperature protonic conductor $SrTi_{1-x}Sc_xO_3$ for $x = 1/8$. This study showed the pathway of proton migration. At the beginning the proton vibrates between O(1) and O(2) oxygen then migrates to O(3) ion and then again start vibrating between O(2) and O(3)[96–98]. Another *ab initio* based molecular dynamics simulation has been performed on the Sr containing cirate $SrCeO_3$ and titanate $SrTiO_3$ materials. $SrCeO_3$ exhibits orthorhombic crystal structure while the titanate counterpart stabilize in cubic structure. The proton conducting pathway has been briefly investigated in this study[99].

1.4 Li^+ ion conductors

Li based solid electrolytes are amongst the best studied materials for solid state electrolyte due to their high thermal stability, high energy density, low self-discharge, excellent life cycle, non flammability and wide range of operating temperature[100–102]. There are various class of Li ion conducting electrolyte.

Li_4SiO_4 and the different derivatives of this material has been studied widely. Though Li_4SiO_4 is not a good ionic conductor ($2\times10^{-5}S/cm$ at $300^{\circ}C$)[103, 104], aliovalent substitutions such as of Si^{4+} by P^{5+}, V^{5+} and As^{5+} at the Si^{4+} site enhance the conductivity[105–108]. $Li_4Si_{1-x}P_xO_4$ series shows best conductivity for the composition $x = 0.4$ at $100^{\circ}C$ [105, 106]. The V^{5+} containing system shows a very high conductivity of the order of $10^{-1}S/cm$ around $400^{\circ}C$ and can be used as a potential material for high temperature battery. Li_4SiO_4 can be substituted by divalent ions such as Zn^{2+}, Mg^{2+}, Co^{2+} or Ni^{2+}[109–111] or trivalent ions Al^{3+}, Ga^{3+} or B^{3+} [112, 113] cations . Divalent Mg^{2+} substituted system having the formula $Li_{4-2x}Mg_xSiO_4$ shows highest conductivity (1.5×10^{-2} S/cm) for composition $x = 0.4$ at $200^{\circ}C$ [111] which is still nearly one order lower for application in batteries.

LISICONs, acronym for Li superionic conductor, are another important class of Li ion conductors that stabilize in γ_{II} orthorhombic phase. These systems have been studied for its high ionic conductivity at high temperatures. $Li_{14}Zn(GeO_4)_4$ [114, 115] is the first material to be named as LISICON and shows excellent conductivity 0.125 S/cm^{-1} at $300^{\circ}C$ but shows very low conductivity of the order of 10^{-7} S/cm at room temperature. This feature is actually suitable for high temperature battery application where the low ionic conductivity is desirable at low temperatures for low self-discharge and high conductivity at higher operating temperature[116]. Li_3PO_4 is another important group of LISICON that permits chemical substitution by tetravalent cation with general chemical formula $Li_{3+x}M^{IV}{}_xM^{V}{}_{1-x}O_4$ where ($M^{IV} = Ge^{4+}$, Si^{4+} or Ti^{4+} and $M^V = P^{5+}$, V^{5+} or As^{5+})[117, 118]. Interestingly, all the intermediate members show higher conductivities than the end members. Among them

$Li_{3.6}Ge_{0.6}V_{0.4}O_{12}$[117] and $Li_{3.6}Si_{0.4}V_{0.6}O_{12}$[118] show very good room temperature ionic conductivity, low self discharge and hence used as solid electrolyte for battery in U.S army.

It should me mentioned that there are other classes of Li ion conducting material which stabilize in NASICON (acronym for sodium superionic conductor)-type structure. These are also refereed to as LISICON material. They form covalent framework of by corner shared PO_4 and ZrO_6 polyhedra, and Li^+ hops through the interstitial sites in the framework. Among them $LiTi_2P_3O_{12}$ system shows highest conductivity at room temperature $7\times10^{-4}\ S/cm$ which rises to 0.1 S/cm at 300˚C[119]. The common problem with this titanate is their instability as Ti^{4+} reduced to Ti^{3+} in contact with Li cathode. But the stability of this material improves when doped with Al^{3+}. $Li_{1.3}Al_{0.3}Ti_{1.7}PO_{12}$ exhibits high conductivity. The Ge, Hf counterpart of the titanium phase show little lower conductivity at room temperature but remain stable with Li atmosphere though expensive for large scale production[120, 121]. The Zr counterpart $LiZr_2P_3O_{12}$ shows two orders of lower conductivity at room temperature which is useful for battery application as it leads to low self-discharge during storage[122].

Li_3N is another group of Li^+ ion conductors which show layered conductivity. Though this material has good conductivity in room temperature ($10^{-3}S/cm$) it has limited practical application as battery material due to its low decomposition voltage (0.44 V)[123]. So attempts have been made to dope Li_3N and make some new materials with high decomposition voltage. Li_3AlN_2 has higher decomposition voltage (0.85 V) but again the conductivity at low temperature is very low[124, 125]. Li_3N has H^+ impurities associated with Li^+ vacancies which is very important for high ionic conduction[126]. When $LiOH$ is mixed to Li_3N and LiI in the ratio of (1:2) it shows two orders of higher ionic conductivity ($0.95\times10^{-3}\ S/cm$) and the decomposition voltage is also quite high (1.6 V)[127] which is useful in battery application.

Li_3P is another Li^+ ion conductor having a moderate conductivity ($10^{-4}\ S/cm$) at room temperature with a decomposition voltage of 2.2 V[128]. Recently a new Li^+ super-ionic conductor, $Li_{10}GeP_2S_{12}$, has been discovered by Kamaya et al. [129] that shows highest Li^+ conductivity compared to all other super-ionic conductor ($1.2\times10^{-2}S/cm$) at room temperature, and is comparable to those of organic liquid electrolyte. This material consists of a

3-D framework structure made of PS_4, GeS_4 tetrahedra and LiS_6 octahedra which stabilize into $P4_2/nmc$ tetragonal structure. One dimensional Li^+ conduction is found in this material along c-axis through the interstitial $16h$ and $8f$ sites. Even at low temperatures ($-30^{\circ}C$) this material shows very high conductivity ($10^{-3}\ S/cm$) which enables battery to operate at lower temperatures also. This material also shows excellent discharge efficiency of about 100% after 2^{nd} cycle of operation with high discharge capacity 120 $mAhg^{-1}$ which makes this material useful for solid state batteries.

Matsuo et al. recently proposed that $LiBH_4$ shows good Li^+ conductivity above 390 K[130]. Though conductivity of this material at room temperature phase is quite low (10^{-7} – $10^{-8}\ S/cm$), it undergoes a structural phase transition from its low temperature orthorhombic to high temperature hexagonal structure and the ionic conductivity increases to the order of $10^{-3}S/cm$. This material does not show any decomposition up-to 5V which indicates high electro-chemical stability. Partial substitution of $[BH_4]^-$ ion $(1-x)LiBH_4 - xLiM$ where ($M = Cl,\ Br$ or I) shows higher conductivity at room temperature without lowering the high temperature conductivity[131]. The reason for this higher conductivity is believed to be the higher polarizability of the doped ions which induce higher mobility to Li^+ [132]. For the I ions lowest activation energy is 0.39 eV reported for $x = 0.13$. The Cl and Br counterparts also show higher conductivity than the host $LiBH_4$[131].

$Li_2(NH_2)(BH_4)$ also shows two to three orders of magnitude higher conductivity ($2 \times 10^{-4}\ S/cm$) than the host $LiBH_4$ at room temperature. However it melts at 368 K[133]. and shows very low activation energy after melting. However $Li_4(NH_2)(BH_4)_3$ shows even more conductivity at room temperature about $2 \times 10^{-4}\ S/cm$. There are also complex hydride material based on $LiNH_2$[134] and $LiAlH_6$[135] investigated. Overall $LiBH_4$ and its derivatives can be potential material for Li based solid state batteries due to its high ionic conductivity, low electronic conductivity, high electrochemical stability and high stability to chemical reaction to Li^+ based anode.

Molecular dynamics simulations were carried out on the compound $LiZr_2P_3O_{12}$ by Padmakumar and Yashonath in 2001. A rigid framework model was used, where all the framework $[Zr_2P_3O_{12}]^{-1}$ ions are kept perfectly rigid and only Li^+ are allowed to move. This study predicts the ionic conductivity and normal to superionic phase transition of this material. The activation energy calculated from the simulation shows good agreement with experiment. The ion migration pathway is predicted as the one which connects M1 and M2 site. The variation of population across temperature and the population density contours around the M1 and M2 sites predicted in the study show good qualitative agreement with experiment [136].

Molecular dynamics simulations on Li_3N by Catlow et al. [137, 138] investigated the details microscopics of Li^+ motion in the system. At 300 K radial distribution function of ion pairs of $N-N$ and $Li(1)-Li(1)$ show features of typical ordered structure but the radial distribution function for $Li(2)-Li(2)$ shows some long range disordered motion. The analysis of Li^+ trajectory identifies a strongly correlated ionic motion between Li^+ ions. As the number of available vacant Li site in Li_3N is less, Li^+ does not reach to a vacant site by direct jump instead it reaches there by several successive jumps cooperatively with other ions [139–141].

There are a few MD studies on Li_2SO_4. Li_2SO_4 possess good ionic conductivity at its high temperature α phase which stabilize in cubic fcc structure [142–144]. The pathway of Li^+ migration is shown is examined at high temperature. The diffusivity calculated from MD shows a little lower value than the experiment.

Li ion conductors are among the most used solid electrolytes in portable devices due to their high charge density, high open circuit voltage, durability and thermal stability. But due to the limited availability of Li and its high cost, now a days there the focus is shifting to alternative electrolytes, more recently.

1.5 Ag^+ ion conductors

Most of the Ag^+ ion conducting materials are based on AgI. At low temperatures, AgI is a mixture of β and γ phases but at $146^{\circ}C$ it transforms to the α phase and shows five to six orders of magnitude rise in conductivity to reach ($\approx 1 S/cm$)[145, 146]. Low conductivity of Ag^+ ions at β-AgI phase is thought of due to the hexagonal closed packing of iodide ions restricting pathways of Ag^+. While at high temperatures, α-AgI in *bcc* eases the Ag^+ movement. But the transition temperature $146\ ^{\circ}C$ is more than the desired operational temperature. Hence for application purpose search of new AgI based conductors have been started[147, 148]. So attempts have been made to get the α-AgI like structure at low temperature by introducing stabilizer ion into AgI matrix. There have been numerous cationic, anionic chemical substitution tried upon AgI material which shall be briefly discussed in the next section.

Ag_3SI was the first attempted anionic substitution upon AgI which shows very good ionic conductivity (0.01 S/cm). This material is stable in β phase at room temperature with body centered cubic lattice structure[149, 150]. The I^- occupy the corners while sulfur sits at the center of the cubic cell. There are four voids for Ag^+ surrounding each face of the *bcc* lattice structure. But the problem with this material is that it decomposes and resulting in a reduction of conductivity. Solid solution of α-AgI with Ag_2SO_4 shows stable good conductivity (0.02 S/cm) at $-20^{\circ}C$, but at room temperature the conductivity gradually decreases with time[151]. There are anionic substitutions, such as by phosphate group, giving rise to good ionic conductivity. $Ag_7I_4PO_4$ and $Ag_{19}I_{15}P_2O_7$ compositions which stabilize in simple cubic lattice with lower activation energy of Ag^+ in the range of 0.16 and 0.14 eV, respectively[151].

Tungstate ion substitution $AgI - Ag_2WO_4$ leads to compounds with higher ionic conductivity. For example, $Ag_6I_4WO_4$ and $Ag_{26}I_{18}W_4O_{16}$ show conductivities 0.047 S/cm and 0.059 S/cm respectively at room temperature[146, 151, 152], hence has been used as battery material.

Several cationic substitution for example by alkali metal ions (Rb^+[153] and K^+[154]), amonium ions (NH^{4+})[155], sulphonium[156] and crabonium[157] ions have successfully

doped in the AgI lattice structure. Among them $RbAg_4I_5$ shows highest conductivity (0.27 S/cm) [158] at room temperature. $RbAg_4I_5$ has a simple cubic structure with lattice parameter of 11.2$\AA$. Iodine ions form tetrahedra which are connected through face sharing. Ag^+ sits at the center of these tetrahedra and diffuses through its faces to the adjacent sites. There are available empty sites for Ag^+ to move through the structure, on an average there are 2.5 tetrahedral sites surrounding one Ag^+.

Doping of ammonium ions in the lattice of AgI leads to higher conductivity[159]. There have been attempts to introduce organic radicals substituted ammonium ions into the lattice of AgI, and improvements in conductivities have been reported[160]. $(CH_3)_4NI - AgI$, $(CH_3)_2(C_2H_5)_2NI - AgI$ or $(C_2H_5)_4NI - AgI$ are the typical examples of ammonium substituted conductors. There have been reports of introducing mercury ions along with alkali metal ions[161] as well as cynide ions[161] and chalcogenide ions[146] in AgI crystal structure.

Several argyrodite silver ion conductors with the general formula $Ag_{12-n}M^{+n}S_6$ where ($M = Ti^{4+}$, Nb^{4+}, Ta^{4+} etc.) have been reported recently which show good silver ion conductivity [162–164]. Most of these type of compounds goes through a phase transition at lower than room temperatures from cubic structure to a less symmetric structure like orthorombic structure. These materials posses high value of Ag^+ conductivity at ambient temperatures ($10^{-2}S/cm$).

There are other Ag^+ ion conductors, such as Ag_5Te_2Cl, reported to shows good 1-D ionic conductivity. There are two reversible phase transitions reported for this compound at temperature 240.9 K and 334.2 K. The high conducting phase, $\alpha - Ag_5Te_2Cl$ shows ionic conductivity of the order of 4.30×10^{-1} S/cm at 469K [165].

There have been numerous computational studies have been carried out on high conducting α phase of AgI conductor. The diffusion coefficient, atomic density analysis, diffusion pathway the phase transition behavior have been studied in detail. In his study Vashista and Rahaman [166] proposed that the Ag^+ moves through the tetrahedral sites. Shimojo and Kobayasi carried out molecular dynamics simulation and analyzing the atomistic density

distribution of Ag^+ concluded that there is a saddle point between two neighboring tetrahedral position[167]. In 1983 Parrinello et al. [168] successfully studied the $\alpha \longleftrightarrow \beta$ phase transition of AgI using NPT-MD (Constant pressure, constant number of atoms and constant temperature molecular dynamics) which showed good agreement with experiment. The study inspired several MD studies on phase transition of AgI. Tallon investigated the phase-diagram study of AgI under constant pressure condition which gave qualitative agreement with experiment[169].

Computational studies on the AgI based electrolytes such as Ag_3SI, Ag_4I_5, $\alpha AgI - Ag_{1-x}Cl_x$ $(0 \leq x \leq 0.25)$ and $Ag_{1-y}Cu_yI$ $(0 \leq x \leq 0.25)$ have been reported. The study on Ag_3SI concluded that the transport of Ag^+ at low temperature β phase is strongly anharmonic around the site while in high temperature α phase, the ion jumps through the sites. Takeuch in 1988 studied the population of Ag^+ and finds good agreement with experiment[170]. MD study on $\alpha - AgI - Ag_{1-x}Cl_x$ predicts correctly the dependence of diffusivity across composition[171] and also calculated the transport number and activation energy. Diffusivity found to decrease with composition and the measurement of transport number as well as the activation energy show good qualitative agreement with experiment. In the study of Cu substituted system also the diffusivity variation with composition and the measurement of Ag^+ transport numbers have been calculated and compared well with experiment[172].

1.6 Na^+ ion conductors

Sodium ion conducting electrolytes find its potential application as solid electrolyte and also in various other industrial fields. Na^+ conducting electrolytes find its applications as sensors technology also. They have been used as sensors for measurement of the amount of CO_2 gas [173, 174] and other volatile organic compounds [175]. Na^+ conducting electrolyte can be used to measure directly the amount of Na^+ in aqueous solution[176] or from molten alumina[177]. Recently the interest over Na^+ onducting electrolyte increases due to its abundance over Li^+ in spite of lower energy density and voltage.

In sodium sulfur cells developed in 1985[178, 179] sodium conducting ceramic tube is placed into sulfur. The anode is metallic sodium in molten state and the cathode is molten S/Na_2S_x where $x = (5 \sim 3)$. This battery operates at a temperature range $(300 - 350^{\circ}C)$ and the output voltage is in the range of 1.78-2.08 V at $350^{\circ}C$[180]. Recently ZEBRA cell (acronym of Zeolite Battery Research Africa) has been developed in improving specific energy storage where instead of sulfur, metal halides has been used as cathode [180–182]. A secondary electrolyte has been included to the solid state halide for fast transport of Na^+ ion in cathode structure and the output voltage in this cell is 2.58 V.

β-alumina and NASICONs are among the most important Na^+ conducting electrolytes having excellent ionic conductivities. There are other Na^+ conducting electrolytes as well as but having somewhat lower conductivity than these two. $Na_2M_2TeO_6$, where ($M = Ni^{2+}$, Co^{2+}, Zn^{2+} and Mg^{2+}) is another series of new Na^+ ion conductor. $Na_2Ni_2TeO_6$ at $300^{\circ}C$ has the high conductivity comparable to β-alumina and NASICON[183]. This materials stabilize in hexagonal $P6_3/mcm$ structure. It is reported that due to the lowest ionic radius and the higher electronegativity, Ni^{2+} based system leads to high conduction. This material has a layered structure along *c*-axis where the layers are made of edge sharing TeO_6 and MO_6 octahedra, and Na^+ ions move in the *a-b* plane. The composite electrolyte where γ-alumina is added to $NaNO_3$ [184] has a higher conductivity than $NaNO_3$ but still lower than those of for β-alumina and NASICON.

1.6.1 β-alumina

β-alumina is one of the most widely used Na^+ conducting electrolyte having excellent 2-D conductivity. β-alumina ($Na_2O.11Al_2O_3$) stabilizes in hexagonal structure ($P6_3/mmc$; $a_0 = 0.559\ nm$, $c_0 = 2.261\ nm$) [185, 186]. In this structure Na^+ conducts in a layer perpendicular to *c*-axis. Alumina layers forms spinel structure and between these two alumina layers sodium oxide layer forms 2-D Na^+ conduction channel. Doping by magnesium or lithium alters the stacking sequence of the layers and transforms into a new rhombohedral phase which is called

as β''-alumina structure($R3m; a_0 = 0.560\ nm, c_0 = 3.395\ nm$) [187, 188]. The stoichiometric formula of Mg doped system is $Na_2MgAl_{10}O_{17}$ and the non stoichiometric formula is $Na_{1+x}Mg_xAl_{11-x}O_{17}$ ($x \leq 1$). This altercation of stacking sequence increases the conductivity of Na^+ in β''-alumina structure (0.2-0.4 S/cm at 300 $^\circ c$) [189, 190], is preferred for uses as Na^+ electrolyte.

Molecular dynamics studies have been carried out on β'-alumina and β''-alumina [191–193]. These studies mainly focus on the the factors which affect the Na^+ migration mechanism. There are mainly two ion conducting site which are called as Beevers-Ross (BR) and anti-Beever-Ross (aBR). Zendejas and Thomas studied the jump time and the numbers of sodium cation from BR to aBR position. This study showed that time of flight is much shorter than the time of residence in these sites which concludes the migration mechanism as jumping process[192]. The conduction process of Na^+ ion in β''-alumina is identified as interstitialcy mechanism, in which the ion moves between lattice and interstitial points[194, 195]. Molecular dynamics study on β''-alumina also support this mechanism [196].

Conductivity variation with temperature for β-alumina shows no change in activation energy [195, 197, 198] but Mg-stabilized β''-alumina shows non Arrhenius behavior at lower temperature[199–201]. MD simulation study also found this non-linear Arrhenius behavior at low temperature[202]. It suggested that the distribution of magenesium ions in spinel block affects the conductivity of Na^+ and the ordering of vacancy at lower temperature leads to this non-linear behavior for β''-alumina structure[202, 203].

1.7 NASICONs

NASICONs is acronym for sodium super ionic conductor. $NaZr_2P_3O_{12}$ is the prototype of this broad and well known family of solids often abbreviated as sodium zirconium phosphate (NZP). NZP material was first discovered by Hagman and Kierkgaard in [204] 1968. The crystal structure stabilizes in $R\bar{3}c$ rhombohedral symmetry and shows high chemical and

thermal stability. The covalently bonded skeleton structure of this compound $[Zr_2P_3O_{12}]^{-1}$ allows hundreds of chemical substitution at all the sites except the oxygen site, as discussed extensively in these papers[205–207]. NZP solids are famous for their various technological importance like use as solid electrolyte, low/negative thermal expansive material and gas sensors etc. Many of the compositions, though do not even contain Na^+ in the structure, having similar framework structures are also called as NZP material. In this thesis the studies have been focused mainly on the ion diffusion and structural changes of NZP solids. So a brief review on the NZP materials exploring these properties will be reviewed.

In 1976 Hong and Goodenough et al. synthesized a series of composition by aliovalent substitution of P^{5+} ion by Si^{4+} having chemical formula $Na_{1+x}Zr_2Si_xP_{3-x}O_{12}$, where $0 \leq x \leq 3$. They exhibit excellent ionic conductivity comparable to β-alumina above 443 K, particularly for $x = 2$ composition[208, 209]. This discovery prompted scientist to experiment extensively on this material and to synthesize NZP-like compounds having better ionic conductivity of NASICON family. In these extensive range of studies along with the fast ion conduction new properties of NASICON materials have been discovered such as low thermal expansivity[210, 211], immobilizer for nuclear waste material[212, 213] and gas sensors[214–217] etc. Roy et al. showed that NZP material is capable of immobilization of large radioactive nuclei such as ^{137}Cs, ^{90}Sr and can be used as a potential material for nuclear waste technology[213].

1.7.1 Structure

Figure1.1 shows the connectivity of the framework skeleton of NZP solids. The basic framework structure $[A_{2n}(XO_4)_{3n}]^{-m}$ consists of corner sharing XO_4 tetrahedra and AO_6 octahedra forming lantern units which makes it stable and at the same time flexible also. These connected lantern units makes hexagonal closed packed structures when looked through the *c*-axis. The general formula of compound from NASICON family is $M1_{0\rightarrow1}M2_{0\rightarrow3}A_2(XO_4)_3$ where $M1$, $M2$ are the two sites for the cations. M1 site has a $\bar{3}$ symmetry. There are only

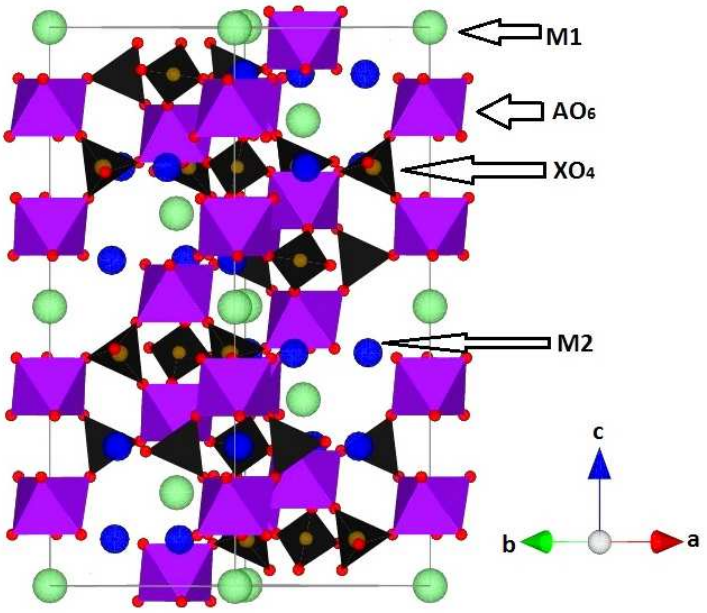

FIGURE 1.1: Framework structure of NZP solids showing corner shared AO_6 octahedra (violet) and XO_4 tetrahedra (black). The locations of the alkali ion sites, M1 (green) and M2 (blue), are also shown.

one M1 site per unit formula and makes a co-ordination of six with oxygen atoms. M2 site has lower $\bar{2}$ symmetry and generally gets filled only when the number of mobile cation exceeds one per unit formula. Although there are cases like $LiZr_2P_3O_{12}$ and $LiTi_2P_3O_{12}$ where at higher temperatures *Li* ion jumps of the M1 site and start populating M2 site[218]. M2 sites are connected to the M1 site making three dimensional pathway for the ion diffusion. There are three M2 sites per formula unit of this compound.

1.7.2 NASICON as Low thermal expansive material

Most of the materials expands upon heating thus having a positive thermal expansion coefficient. But there are certain materials which show very low or even negative thermal expansion coefficient and have drawn the attention in recent years due to their potential applications in various fields[219]. These low thermal expansive materials find its applications in of optical

mirrors, fiber optics materials, packaging for optical gratings etc. They are also used in thermal shock resistance devices. In biomedical and electronic applications field also these type of materials are used.

ZrW_2O_8, AM_2O_7 where ($A = Ti^{4+}$, Zr^{4+}, Hf^{4+} or Sn^{4+}) and ($M = P^{5+}$ or V^{5+}), $Sc_2(WO_4)_3$ and NASICONs are among the widely used material used for low thermal expansion applications. $Zr_2W_2O_8$ shows an isotropic negative thermal expansion coefficient of -9.1×10^{-6} $/K$ in the temperature range of 0-300 K [220, 221]. The framework structure of this material is made of corner shared ZrO_6 octahedra and WO_4 tetrahedra and stabilizes in cubic structure. The ZrO_6 octahedra shares all its six corner with WO_4 tetrahedra but in very unusual way WO_4 tetrahedra shares only its three oxygen out of four with WO_4. Pryde et al. proposed with their simple model that there are unusually high phonon density of states in low energy modes which expected to give rise to negative thermal expansion to these material[222].

ZrV_2O_7, ZrP_2O_7 are the another family of materials which show low/negative thermal expansion behavior. ZrV_2O_7 undergoes two structural phase transitions at temperature 345 K and 375 K and after the second phase transition the material shows very strong negative thermal expansion co-efficient -7.1×10^{-6} $/K$ over the temperature range of 400 -500 K[223, 224]. ZrP_2O_7 also undergoes a structural phase transition at 570 K and above this temperature the material shows low thermal expansion coefficient 5.4×10^{-6} $/K$ over the temperature range of 600 - 700 K[225].

Another material $Sc_2(WO_4)_3$ also shows negative thermal expansion coefficient. This material consists of corner shared ScO_6 octahedra and WO_4 tetrahedra and stabilizes in orthorhombic structure[226]. This material shows contraction along the a and c direction and expansion along the b direction upon heating. These anisotropic expansion of the lattice parameters leads to a volume contraction of these type of material. The bulk thermal expansion coefficient of these materials in the temperature range of 10-450 K is -2.2×10^{-6} $/K$[227].

NZP material with the general formula $M1_{0\rightarrow1}M2_{0\rightarrow3}A_2(XO_4)_3$ also forms a broad family

of low thermal expansion materials. NZP compound is capable of numerous chemical substitutions at its skeleton forming cation site *A* as well as in the non-skeleton cation sites *X*, M1 and M2. The skeleton forming cation *A* can be replaced by cations of different oxidation states ranging from +1 to +5, for example, monovalent-Na^{+}, divalent-Zn^{2+}, Ni^{2+}, Co^{2+} or Cu^{2+} , trivalent-Al^{3+}, Ti^{3+}, Fe^{3+}, Ga^{3+} or Cr^{3+}, tetravalent-Ti^{4+}, Ge^{4+}, Sn^{4+}, Si^{4+} or Hf^{4+} and pentavalent-Nb^{5+} or Ta^{5+}. Another skeleton forming cation *X* is either partially or fully replaced by Si^{4+}, Ge^{4+}, As^{5+}, W^{5+} or V^{5+} in most of the cases. The non skeleton position M1, M2 can also be occupied by cations of different oxidation state but in majority of the compounds they are filled by ions with lower oxidation states.

The reactivity and the structural properties of the NZP compound depends on the interaction of the strong covalently bonded skeleton $[A_{2n}(XO_4)_{3n}]^{-m}$ (strongest when *A* is tetravalent and *X* is pentavalent) with the non skeleton cations held in M1 and M2 sites. The relation between lattice parameter variation of NZP solid with various composition has been studied in detail over the years. As discussed earlier there are so many varieties of substitutions and therefore all the substitutions and its relation to the structural response can not be generalized all together. So some important chemical substitutions have been analyzed separately.

In compound $M1A_2(XO_4)_3$, the structural response to chemical substitution has been studied extensively. Two different types of substitutions have been examined. In the first one for fixed non-skeleton M1 cation size, the size of the skeleton cation *A* has been varied from Ge^{4+}, Ti^{4+}, Sn^{4+} to Zr^{4+} and in the second study the size of the M1 cation is varied from Li^{1+}, Na^{+}, K^{+}, Rb^{+} and Cs^{+} for fixed *A* cation[205, 206].

For a particular M1 alkali ion the lattice parameters *a* and *c* are both found to show increment with the larger size of *A*, which is quite obvious result as the covalent *A*-*O* bond is stronger due to its covalent nature and insertion of larger cation size just expands the whole framework structure. But due to the insertion of larger cation at M1 sites the lattice parameters show an anomalous variation where *a* contracts and *c* parameter expands for a particular skeleton framework. The insertion of larger cation in M1 site expands the volume of the $M1O_6$ octahedra which creates dilatational stress on the two AO_6 octahedra. It should be

mentioned that these AO_6 octahedra and XO_4 tetrahedra posses a certain degree of rotational freedom along its three fold and two fold rotational axis respectively. To counter this extra stress created due to the larger cations these polyhedra goes through a coupled rotation. These coupled rotation leads to the anomalous behavior of the lattice parameters.

Thermal expansion behavior of these materials also show same anisotropic variation. Increment in temperature effect the weakest M1-O bond lengths leaving stronger *A-O* and *X-O* bonds nearly unaffected. Increment in M1-O bond produces same qualitative effect as of the insertion of the larger cation. Therefore the NZP skeleton responds through the same mechanism of coupled rotation to counter the temperature increment. As the lattice parameter of this compound shows anisotropic variation, contraction in *a* direction and expansion in *c* direction, the overall thermal expansion coefficient of the compound from NZP family shows very low or negative value[205, 206, 228].

There are lots of experimental studies on the variety of compositions of NZP family and their thermal expansion coefficient has been studied systematically. The analysis of these experiments concludes that the occupancy and nature of the cation sitting at the M1 sites has a deciding effect on the thermal expansion coefficient. In the compound $M1A_2(XO_4)_3$, the anisotropic nature of the lattice parameter expansion upon heating reduces for the larger cation size in the AO_6 octahedral hole. This is because of insertion of larger cation already put more pressure on the framework skeleton at room temperature so the framework do not expand or contract easily on the further increment of temperature. As a result the thermal coefficient as well as the anisotropy in the lattice parameter variation reduces for the larger cation size of this series which is Cs ($\alpha_a = -0.56 \times 10^{-6}$, $\alpha_c = 0.45 \times 10^{-6}$, $\alpha_{avg} = -0.22 \times 10^{-6}$ /K) compared to the smaller cation size Na ($\alpha_a = -5.5\times10^{-6}$, $\alpha_c = 22.30\times10^{-6}$, $\alpha_{avg} = 3.8\times10^{-6}$ /K)[229].

For the compound $LiTi_2P_3O_{12}$, α_c shows the maximum value of $30.80 \times 10^{-6}/K$ reported in the NZP family of solids. This is explained as Li^+ ion migrates from the M1 position to M2 positions as temperature increases, which increase the repulsion of oxygen chains around the vacant M1 sites resulting increase in the α_c value[218].

In another class of NZP compound where all the M1 sites are not fully filled and M2 sites are fully vacant for example $B_{0.5}A_2P_3O_{12}$ or $Ln_{0.33}A_2P_3O_{12}$ where $B = Ca^{2+}$, Sr^{2+}, Cd^{2+} and Ba^{2+} and $A = Ti^{2+}$ and Zr^{2+} the cation filled M1 sites and vacant M1 sites sometimes behave differently under the thermal increment. For example, in the structure $Cd_{0.5}Zr_2P_3O_{12}$ and $Ca_{0.5}Zr_2P_3O_{12}$ the vacant M1 sites expands during heating while for the compound $Ca_{0.5}Ti_2P_3O_{12}$ they contract during heating[230].

There are experimental reports also on the compound like $Na_5ZrP_3O_{12}$ where M1 and M2 sites are filled with cations. Here also the value of thermal coefficient depends on the size of the cation sizes in the M1 and M2 sites. It is found that the larger the cation size filling the cation positions lower the absolute value of the thermal expansion coefficient α_c, α_a and the anisotropy[231].

In the empty skeleton where M1 and M2 are both vacant, the anisotropy of expansion and contraction depends on the bond length on the *A*-*O* and *O*-*O* bond lengths. Again the *L*-*O* bond length depends on the size of the *L* cation. The average thermal expansion coefficient α_{avg} has range from $-1 \times 10^{-6}/K$ to $1 \times 10^{6}/K$[232].

The coupled polyhedral rotation remain the main cause for the extraordinary chemical and thermal flexibility of the NZP solids. Thermal expansion of the NZP material can be tailored according to the requirement varying the compositions at different cation sizes. Thus this family of solids became an important family of material to be used in low thermal expansion devices and the thermal shock resistance material.

1.7.3 NASICON as solid electrolyte

In 1976 Hong [208] reported the X-ray structure of the NASICON compound with the general chemical formula $Na_{1+x}Zr_2Si_xP_{3-x}O_{12}$ for $0 \leq x \leq 3$. Compositions of this series in $1.6 \leq x \leq 2.2$ range shows conductivity at $300^{\circ}C$ comparable to those of β- alumina. Compositions of this series, except for the range $x = 1.6 - 2.2$ stabilize in the $R\bar{3}c$ crystal structure.

These compositions around $x = 2$ shows slight monoclinic $C\bar{2}c$ modifications. In his study Hong synthesized Na excess compounds $Na_5Zr_4(PO_4)_7$ and $Na_7Zr_5(PO_4)_9$ as well which also stabilize in $R\bar{3}c$ crystal structure but show very minimal ionic conductivity. Material with Na^+ ion exchanged by Li^+, K^+ and Ag^+ at compositions $x = 0$ and $x = 3$ have been prepared and they all stabilizes in $R\bar{3}c$ crystal structure. In an extension of this work Goodenough and his coworkers [209] reported the conductivity of this series at $300^{\circ}C$ for various composition x. The activation energy reported for the $x = 2$ composition $Na_3Zr_2Si_2PO_{12}$ is 0.29 eV above which is 0.1 eV higher than that of for β- alumina. The advantage in NASICON material over β-alumina is that it shows three dimensional Na^+ conduction while in β- alumina the Na^+ ion shows two dimensional conductivity.

Von Alpen in 1979 found a second order phase transition in the $x = 2$ composition $Na_3Zr_2Si_2PO_{12}$ in the temperature range of 410 - 450 K[233]. The sintering temperature of the material was 1250 $^{\circ}C$. The phase transition associated with a change in activation energy from 0.34 eV at low temperature (310 to 410 K) to 0.2 eV at higher temperature region (450 to 625 K). The plot of constant pressure specific heat from colorimetric measurements shows a λ like behavior again peaking around 440 K. The phase transition was reported to be associated with a structural change from low temperature monoclinic to high temperature rhombohedral structure.

In their study Kohler and Schultz[234, 235] investigated the diffusion pathway for the NASICON series where Zr^{4+} is partially substituted by Na^+ ion, $Na_{1+x+4y}Zr_{2-y}Si_xP_{3-x}O_{12}$ ($0 \leq x \leq 3$ and $0 \leq y \leq \frac{3}{4}$). Three compositions $x = 0$, $x = 1.4$ for $y = 0.2$ and $x = 3$ for $y = 0$ have been studied. In his study he predicted the diffusion pathway for Na^+ ion is the path connecting Na1 and Na2 sites. The two bottleneck of this connecting pathway has been identified as two triangles formed by oxygen atoms. These triangles share a common edge and made a distorted tetrahedron. They studied the population density function and found a much spread-out distribution of Na^+ and wider Na1-Na2 pathway for $x = 1.4$ composition than the end member $x = 3$. The expansion of the NaO_6 octahedra due to the expansion of

the *c* parameter has been the reason for the opening of the bottleneck for $x = 1.4$ composition which leads to the spread out population distribution.

In 1985 Nicholas et al. studied [236] the influence of impurities on the NASICON compositions $Na_{1+x}Zr_2Si_xP_{3-x}O_{12}$ in the range $1.85 \leq x \leq 2.3$. Use of sodium-sodium cell test seems to be not appropriate for the measurement of Na^+ conductivity due to degradation of NASICONs by sodium metal. Complex-plane analysis appeared to be more powerful technique to measure the conductivity. Zirconia-deficit material shows higher conductivity than the original stoichiometric compound which indicates presence of second-phase zirconia inhibits the Na^+ conduction. On the other hand, presence of excess sodium oxide enhances the sodium ion conduction. Kreuer et al.[237] examined the chemical durability of $x = 0,\ 3$. He reported the degradation by molten sodium but only for phosphorus containing systems($x = 0$). However only silicate ($x = 3$) containing member shows better stability against molten sodium as well as against molten sulfur. The stability of NASICON in contact with water has been studied by Fuentes et al.[238]. A significant decrease in ionic conductivity has been observed when dense pellets are exposed to water for more than 300 hours due to the increment of grain boundary resistance. Though recently non-hydrolytic synthesis of NASICON compound $Na_3Zr_2Si_2P_3O_{12}$ has been reported by molecular precursor-based approach which helps to get pure NASICON material[239].

In 1988 Boilot et al.[240] carried out an detailed study on the lattice parameter variation, site occupancy and the change in interatomic bond lengths across the the composition *x* of the NASICON series $Na_{1+x}Zr_2Si_xP_{3-x}O_{12}$. They reported single crystal X-ray structure of the composition range $2 \leq x \leq 2.4$. Most interestingly they indicated the presence of an intermediate mid-Na site falling in the connecting pathway of Na1-Na2 site. The general formula for site occupancies was given as $(Na1 + mid - Na)_1 + Na2_x \bigcirc_{3-x} Zr_2P_{3-x}O_{12}$, which says one Na^+ per unit formula will occupy either Na1 or mid-Na site and *x* number of Na^+ occupy the same number of Na2 sites leaving $(3 - x)$ number of Na2 sites vacant. The circle represents the number of vacant Na2 sites. In the formula itself the simultaneous occupancy of Na1 and its neighboring mid-Na site has been excluded. The variation of occupancy of

Na sites across the composition x shows very interesting feature, for $x = 0$ all the Na1 sites remain occupied. As x increases from zero the occupancy of Na2 site keeps on increasing monotonically and the occupancy of Na1 site decreases and reaches its minimum for the composition $x = 2$ and then again increases towards $x = 3$. The occupancy of the mid-Na site shows just the opposite behavior as shown by Na1 site occupancy which is quite understandable from the general occupancy formula mentioned above where it states one sodium per unit formula will be occupied by either Na1 or mid-Na site.

The lattice parameter c and the average $Na1\text{-}O$ bond distance also shows maximum value at $x = 2$ and decreases for the two end member $x = 0$ and 3, while a is found to increase monotonically with the composition x. The expansion of c and $Na1 - O$ can be related to the opening of the bottleneck in the Na1-Na2 pathway. Interestingly the variation of c parameter and $Na1\text{-}O$ bond lengths across the composition x follow the same trend as that of the conductivity. Thus the size of the bottleneck was thought of playing an important role in controlling the conductivity.

Study on the Zr deficient material has been reported for the NASICON series $Na_3Zr_{2-\frac{x}{4}}Si_{2-x}P_{1+x}PO_{12}$ in the composition range $0 \leq x \leq 2$ [241, 242]. Highest ionic conductivity observed for the composition $x = 1.667$, $6\times10^{-4}\ S/cm$ from the value of $6\times10^{-5}\ S/cm$ for the composition $x = 0$. The variation in ionic conductivity is effected is proposed to be affected by the variation of bottleneck size for different composition.

Yuria et al.[243] reported a series of chemical formula $Na_{1.5}M_{0.5}Zr_{1.5}P_3O_{12}$ where Zr^{4+} ion is substituted by a series of trivalent ion, M (Al^{3+}, Ga^{3+}, Cr^{3+}, Sc^{3+}, Fe^{3+}, Yb^{3+} or Y^{3+}). The conductivity of this series at $100^{\circ}C$ found to increase with the larger ionic radius of the trivalent ions. This can be related to the increase of lattice parameters with the larger ions which essentially contributes to increment of the bottleneck size for Na^+ migration. At higher temperature $300^{\circ}C$ also the conductivity variation of this series behave similarly except in the case of Yb^{3+} and Y^{3+}, which show lower conductivity than In^{3+} or Sc^{3+}. But none of the material of this series has higher conductivity than $Na_3Zr_2Si_2PO_{12}$. Experimental study on In^{3+} doped series $Na_{1+x}Zr_{2-x}In_xP_3O_{12}$ series in the range $0 \leq x \leq 1.85$ has been reported to

show higher conductivities for the higher x value. For the composition up-to $x = 0.8$ Na^+ remain relatively localized and the increment in conductivity is due to the presence of access Na^+ only and the activation energy also remain nearly constant in this range. But for the composition $x \geq 0.8$ a progressive delocalization of Na^+ has been observed and the activation energy decreases and reaches minimum for composition $x = 2$[244, 245].

Another study where Zr^{4+} has been substituted by rare earth material in $Na_{1+x}M_x\,Zr_{2-x}P_3O_{12}$ where $M = Yb^{3+}$, Er^{3+} and Dy^{3+} shows increment in conductivity upto $x = 1$ then decreases upto $x = 2$ but again no compound of this series shows higher conductivity than $Na_3Zr_2Si_2PO_{12}$ [246]. Substitution of Zr^{4+} by homovalent Ti^{4+} in $Na_{1+x}Ti_yZr_{2-y}Si_xP_{3-x}O_{12}$ in the range of $0 \leq x \leq 2$ and $0 \leq y \leq 2$ has been reported by Shimazu et al.[247]. However in this x range the conductivity decreases with the increment of Ti^{4+} which can be explained due to the smaller size of the TiO_6 octahedra compared to the ZrO_6 octahedra which reduces the bottleneck size of the Na^+ ion migration. Another study on the same series reported increment in conductivity of Ti^{4+} substituted system from $y = 0$ to 0.5 then again, decreases for higher value of $y \geq 0.5$ for compounds with higher sodium content $x = 3$, $Na_4Ti_yZr_{2-y}si_3O_{12}$[248].

There are other studies of Zr^{4+} substitution by homovalent ions by As^{4+}, Ge^{4+}, Ti^{4+} and Hf^{4+}. The Hf counterpart at room temperature shows nearly 50% higher conductivity ($1.0 \times 10^{-3}\ S\ cm^{-1}$) than $Na_3Zr_2Si_2PO_{12}$ having a conductivity of $6.7 \times 10^{-4}\ S\ cm^{-1}$ [240, 249–251]. But at higher temperature $Na_3Zr_2Si_2PO_{12}$ shows better conductivity than $Na_3Hf_2Si_2PO_{12}$. Substitution of tetravalent Zr^{4+} by bivalent Mg^{2+} in the series $Na_{1+x}Zr_{2-x/2}Mg_{x/2}P_3O_{12}$ has been investigated in the range $0 \leq x \leq 2$. This series shows progressively higher conductivity with composition x [252].

Recently Sn^{4+} doped material $Na_3SnZrSi_2P_3O_{12}$ (NASN) and $Na_3Sn_2Si_2P_3O_{12}$ (NASN2) substituting the Zr atom has been reported. Insertion of Sn atom change the lattice parameters which affects the size of the bottleneck[253]. NASN shows higher but NASN2 shows lower values of c parameter compared to the parent compound $Na_3Zr_2Si_2P_3O_{12}$. Consecutively higher ionic conductivity has been observed for NASN material $Na_3Zr_2Si_2P_3O_{12}$ while NASN2 shows lower conductivity over a wide range of temperatures (300 - 625 K).

There are reports on the trivalent and tetravalent ion conducting NAICON type materials also. Zr^{4+} and Hf^{4+} ion are the typical tetravalent carriers reported in the NASICON type material $MNbP_3O_{12}$[254, 255]. Hf^{4+} ion shows the highest ionic conductivity among tetravalent ion conductor. Sc^{3+} and Al^{3+} are the typical examples of trivalent ion conductors in the NASICON type material. Sc^{3+} exhibits ionic conductivity of $1.06 \times 10^{-4}\ S/cm$ at $600^{\circ}C$ in the composition $Sc_{\frac{1}{3}}Zr_2P_3O_{12}$[256]. Highest Al^{3+} ion conductivity of $6.1 \times 10^{-4}\ S/cm$ observed in the material $[Al_{0.2}(Zr_{0.8}Ti_{0.2})_{0.8}]_{\frac{20}{19}}NbP_3O_{12}$ at $600^{\circ}C$[257].

1.7.4 Computational studies on NASICON material

Daniele Mazza [258] carried out bond valence calculation to investigate the ionic conductivity of NASICON material. His study mainly focused on the four different Na^+ conducting systems of the the idealized NASICON structures, the rhombohedral NASICON series $Na_{1+x}Zr_2Si_xP_{3-x}O_{12}$ for the compositions $0 \leq x \leq 3$, few miscellaneous NASICON compound with rhombohedral crystal symmetry, and the $x = 2$ composition $Na_{3.05}Zr_2Si_{2.05}P_{0.95}O_{12}$ with monoclinic symmetry. The lowest bond valence sum m(x,y,z) for the two different pathway for Na^+ ion migration Na1-Na2 and Na2-Na2 have been compared. For idealized NASICON structure the m(d) maxima shows higher value for Na2-Na2 pathway and concluded to be the more probable pathway than Na1-Na2. But for the NASICON series with rhombohedral structure the rotations of the polyhedra comes into play and shows twine maxima in the m(d) plot for Na1-Na2 pathway while Na1-Na2 pathway shows only one maxima. Thus for this structure Na1-Na2 has been predicted as more probable pathway. This study also predicted that $x = 2$ composition of this series offers easiest pathway for ion migration and hence shows highest conductivity. In the monoclinic NASICON structure the Na2 position of the rhombohedral structures splits into two different sites Na2 and Na3. This study predicts that the Na2 site remain fully occupied in this structure blocking the Na^+ ion movement. And m(d) values shows Na1-Na3-Na1 pathway as the easier pathway than the Na1-Na2-Na1.

Padma Kumar and Yashonath carried out simulation studies[259, 260] on the ionic conduction of the NASICON series $Na_{1+x}Zr_2Si_xP_{3-x}O_{12}$ for $0 \leq x \leq 3$. This study reproduces the framework structure, ionic conductivity variation with composition any many other features successfully. The variation of Na-O bond lengths, lattice parameter variation and occupancy per site were all in agreement with the the Boilot's experimental result discussed earlier. This study also suggested the diffusion pathway is the one connecting Na1-Na2 sites. However the $x = 2$ composition shows comparative low free energy barrier for ion diffusing from Na1 to Na2 site.

1.8 Motivation for the present studies

The conductivity variation behavior of the NASICON series, $Na_{1+x}Zr_2Si_xP_{3-x}O_{12}$, with composition x is still largely speculative. Kohler and Schultz[234, 235] proposed that the expansion of c parameter opens up the bottleneck leading to larger thermal vibration of the Na^+ and a spread out of population density in the Na1-Na2 pathway. Tranqui et al.[261, 262] suggested that the c parameter peaks around $x = 2$, which is directly related to the opening-up of the triangular bottleneck, could be responsible for the conductivity maximum around $x = 2$. Another proposal[240, 263] has been that an enhancement in ion-ion correlation due to increased Na^+ concentration could give rise to the conductivity maximum around $x = 2$.

There has been significant variance in the reported values of conductivity across experimental studies[114, 240, 249]. Colomban et al.[264] showed that the conductivity variation with temperature and activation energies of the $x = 2$ composition depends on the sintering temperature of the material. Samples prepared at high sintering temperatures show signatures of monoclinic to rhombohedral transitions, both in heat capacities and in Arrhenius plots. This calls for detailed microscopic investigations. Evidence for orientational disorder of plolyhedra depending on sintering temperatures were also discussed[264]. It would be interest to investigate if these orientational disorder, which were more pronounced for the case of $x = 2$ composition, is linked to the conductivity maximum. It shall be recalled that in superionic

systems such as LAMOX ($La_2Mo_2O_9$) the rotation of tetrahedral moieties influences ion hops between sites, enhancing the transport of oxygen ions et al. [265].

Highlighted, above are some of the interesting aspects that call for microscopic investigations on structure and ion transport in NASICONs, and forms the motivation behind the present computer simulation studies detailed in the thesis. Chapter 2 describes the major computational techniques employed in the studies. In chapter 3 of the thesis the extent of framework flexibility of $NaZr_2P_3O_{12}$ upon various alkali ion substitutions is examined over a wide a range of temperatures, employing Monte Carlo simulations. Chapters 4 and 5 discusses the influence of Si/P ordering on the ion transport in $Na_3Zr_2Si_2PO_{12}$ and $Na_2Zr_2SiP_2O_{12}$, the $x = 2$ and $x = 1$ compositions of $Na_{1+x}Zr_2Si_xP_{3-x}O_{12}$ respectively.

Bibliography

[1] D. Almond and A. West, Nature **306**, 456 (1983).

[2] H. Klauk, Nat. Mat. **8**, 853 (2009).

[3] M. Armand and J.-M. Tarascon, Nature **451**, 652 (2008).

[4] Y.-M. Chiang, Science **330**, 1485 (2010).

[5] J.-M. Tarascon and M. Armand, Nature **414**, 359 (2001).

[6] E. Kendrick and P. Slater, Annual Reports Section" A"(Inorganic Chemistry) **102**, 482 (2006).

[7] D. K. Belashchenko, Phys.Usp. **42**, 297 (1999).

[8] B. C. Steele and A. Heinzel, Nature **414**, 345 (2001).

[9] P. Knauth and H. L. Tuller, J. Am. Ceram. Soc. **85**, 1654 (2002).

[10] B. Kang and G. Ceder, Nature **458**, 190 (2009).

[11] J. Maier, Nature materials **4**, 805 (2005).

[12] M. Ingram, Nature **362**, 112 (1993).

[13] M. A. Hayward and M. J. Rosseinsky, Nature **450**, 960 (2007).

[14] Z. Gadjourova, Y. G. Andreev, D. P. Tunstall, and P. G. Bruce, Nature **412**, 520 (2001).

[15] J. B. Goodenough, Annual Review of Materials Research **33**, 91 (2003).

[16] S. Stølen, E. Bakken, and C. E. Mohn, Phys. Chem. Chem. Phys. **8**, 429 (2006).

[17] O. Diat and G. Gebel, Nature materials **7**, 13 (2008).

[18] K. Kreuer, Annual Review of Materials Research **33**, 333 (2003).

[19] E. Kendrick, J. Kendrick, K. S. Knight, M. S. Islam, and P. R. Slater, Nature materials **6**, 871 (2007).

[20] J. B. Goodenough, Proceedings of the Royal Society of London. A. Mathematical and Physical Sciences **393**, 215 (1984).

[21] H. L. Tuller, Solid State Ionics **131**, 143 (2000).

[22] M. Armand, F. Endres, D. R. MacFarlane, H. Ohno, and B. Scrosati, Nature materials **8**, 621 (2009).

[23] R. Agrawal and R. Gupta, J. Mat. Sci. **34**, 1131 (1999).

[24] S. Hull, Reports on Progress in Physics **67**, 1233 (2004).

[25] A. Kingon, Nature Materials **5**, 251 (2006).

[26] M. Saiful Islam and P. R. Slater, MRS bulletin **34**, 935 (2009).

[27] J. Portier, J. Reau, S. Matar, and Soubeyroux, Solid State ionics **11**, 83 (1983).

[28] M. Turaeva, S. Kot, O. Glumov, and I. Murin, Russ. J. Appl. Chem. **74**, 596 (2001).

[29] N. Sorokin and B. Sobolev, Crystallogr. Rep **52**, 842 (2007).

[30] Y. Koyama, I. Tanaka, and H. Adachi, J. Electrochem. Soc. **147**, 3633 (2000).

[31] V. Trnovcová, P. P. Fedorov, and I. Furár, J. Rare Earths **26**, 225 (2008).

[32] D. K. de Boer et al., Opt. Express **20**, A395 (2012).

[33] L. Patro and K. Hariharan, Solid State Ionics **239**, 41 (2013).

[34] K. Hariharan and J. Maier, J. Electrochem. Soc. **142**, 3469 (1995).

[35] N. Vaidehi, R. Akila, A. Shukla, and K. Jacob, Mater. Res. Bull. **21**, 909 (1986).

[36] L. Patro and K. Hariharan, Mater. Res. Bull. **47**, 2492 (2012).

[37] L. Patro and K. Hariharan, Ionics , 1 (2013).

[38] S. Vilminot, R. Bachmann, and H. Schulz, Solid State Ionics **9**, 559 (1983).

[39] A. Podgorbunsky, S. Sinebryukhov, and S. Gnedenkov, Physics Procedia **23**, 94 (2012).

[40] M. M. Ahmad, K. Yamada, and T. Okuda, J. Phys. Cond. Matter **14**, 7233 (2002).

[41] S. Matar, J.-M. Reau, J. Grannec, and L. Rabardel, J. Solid State Chem. **50**, 1 (1983).

[42] D. Avignant, I. Mansouri, R. Chevalier, and J. Cousseins, J. Solid State Chem. **38**, 121 (1981).

[43] C. Tiller, A. Lilly, and B. LaRoy, Phys. Rev. B **8**, 4787 (1973).

[44] J. D. Targove and A. R. Murphy, Thin solid films **191**, 47 (1990).

[45] D.-X. Wu, X.-J. Wu, Y.-f. LÜ, and H. Wang, Transactions of Nonferrous Metals Society of China **16**, 828 (2006).

[46] L. Patro and K. Hariharan, Mater. Lett. **80**, 26 (2012).

[47] W. Puin, S. Rodewald, R. Ramlau, P. Heitjans, and J. Maier, Solid State Ionics **131**, 159 (2000).

[48] S. Kim, Electrochemical Society Interface , 29 (2006).

[49] A. Rahman, J. Chem. Phys. **65**, 4845 (1976).

[50] P. Lindan and M. Gillan, J. Phys. Condens. Matter **5**, 1019 (1993).

[51] A. Ivanov-Shitz, A. Buchstab, S. K. Aityan, and H.-H. Kohler, Appl. Phys. A **54**, 251 (1992).

[52] A. Walker, M. Dixon, and M. Gillan, J. Phys. C: Solid State Phys. **15**, 4061 (1982).

[53] F. Zimmer, P. Ballone, M. Parrinello, and J. Maier, Solid State Ionics **127**, 277 (2000).

[54] L. Malavasi, C. A. Fisher, and M. S. Islam, Chem. Soc. Rev. **39**, 4370 (2010).

[55] O. H. Kwon and G. M. Choi, Solid State Ionics **177**, 3057 (2006).

[56] H. Scott, J. Mater. Sci. **10**, 1527 (1975).

[57] S. Badwal, F. Ciacchi, and D. Milosevic, Solid State Ionics **136**, 91 (2000).

[58] A. Lashtabeg and S. J. Skinner, J. Mater. Chem. **16**, 3161 (2006).

[59] K. Eguchi, T. Setoguchi, T. Inoue, and H. Arai, Solid State Ionics **52**, 165 (1992).

[60] O. A. Marina, C. Bagger, S. Primdahl, and M. Mogensen, Solid State Ionics **123**, 199 (1999).

[61] H. Inaba and H. Tagawa, Solid state ionics **83**, 1 (1996).

[62] T.-H. Yeh and C.-C. Chou, Solid State Ionics **180**, 1529 (2009).

[63] T. Takahashi, H. Iwahara, and T. Arao, J. Appl. Electrochem. **5**, 187 (1975).

[64] H. J. Bouwmeester and A. J. Burggraaf, Membrane Science and Technology **4**, 435 (1996).

[65] A. A. Yaremchenko, V. V. Kharton, E. N. Naumovich, and A. A. Vecher, J. Solid State Electrochem. **2**, 146 (1998).

[66] A. A. Yaremchenko, V. V. Kharton, E. N. Naumovich, A. A. Tonoyan, and V. V. Samokhval, J. Solid State Electrochem. **2**, 308 (1998).

[67] H. L. Tuller, Solid State Ionics **52**, 135 (1992).

[68] T.-H. Yu and H. Tuller, J. Electroceram. **2**, 49 (1998).

[69] J. Díaz-Guillén et al., Solid State Ionics **179**, 2160 (2008).

[70] T. Ishihara, H. Matsuda, and Y. Takita, J. Am. Chem. Soc. **116**, 3801 (1994).

[71] K. Huang, M. Feng, and J. B. Goodenough, J. Am. Ceram. Soc. **79**, 1100 (1996).

[72] M. Feng and J. Goodenough, Eur. J. Solid State Inorg. Chem. **31**, 663 (1994).

[73] P. Lacorre, F. Goutenoire, O. Bohnke, R. Retoux, and Y. Laligant, Nature **404**, 856 (2000).

[74] C. Tealdi, L. Malavasi, C. Ritter, G. Flor, and G. Costa, J. Solid State Chem. **181**, 603 (2008).

[75] X. Wang, Z. Cheng, and Q. Fang, Solid State Ionics **176**, 761 (2005).

[76] T. Ishihara et al., Solid State Ionics **113**, 593 (1998).

[77] M. Kobayashi and H. Okazakitn, J. Phys. Soc. Jpn. **61**, 2848 (1992).

[78] F. Shimojo and H. Okazaki, J. Phys. Soc. Jpn. **61**, 4106 (1992).

[79] H. Inaba, R. Sagawa, H. Hayashi, and K. Kawamura, Solid State Ionics **122**, 95 (1999).

[80] H. Hayashi, R. Sagawa, H. Inaba, and K. Kawamura, Solid State Ionics **131**, 281 (2000).

[81] H. Hayashi et al., Solid State Ionics **122**, 1 (1999).

[82] Y. Yamamura et al., Solid State Ionics **160**, 93 (2003).

[83] H. Iwahara, H. Uchida, K. Ono, and K. Ogaki, J. Electrochem. Soc. **135**, 529 (1988).

[84] H. Iwahara, Solid State Ionics **28**, 573 (1988).

[85] L. Malavasi, C. Ritter, and G. Chiodelli, Chem. Mater. **20**, 2343 (2008).

[86] P. Babilo, T. Uda, and S. M. Haile, J. Mater. Res. **22**, 1322 (2007).

[87] S. Tao and J. T. Irvine, J. Solid State Chem. **180**, 3493 (2007).

[88] K. Kakinuma, A. Tomita, H. Yamamura, and T. Atake, J. Mater. Sci. **41**, 6435 (2006).

[89] E. Quarez, S. Noirault, M. T. Caldes, and O. Joubert, J. Power Sources **195**, 1136 (2010).

[90] T. Norby and N. Christiansen, Solid State Ionics **77**, 240 (1995).

[91] K. Amezawa, S. Kjelstrup, T. Norby, and Y. Ito, J. Electrochem. Soc. **145**, 3313 (1998).

[92] D. A. Boysen, T. Uda, C. R. Chisholm, and S. M. Haile, Science **303**, 68 (2004).

[93] S. M. Haile, D. A. Boysen, C. R. Chisholm, and R. B. Merle, Nature **410**, 910 (2001).

[94] R. Haugsrud and T. Norby, Nat. Mater. **5**, 193 (2006).

[95] W. Münch, K. Kreuer, U. Traub, and J. Maier, J. Mol. Struct. **381**, 1 (1996).

[96] F. Shimojo, K. Hoshino, and H. Okazaki, J. Phys. Soc. Jpn. **66**, 8 (1997).

[97] F. Shimojo, K. Hoshino, and H. Okazaki, J. Phys. Soc. Jpn. **65**, 1143 (1996).

[98] F. Shimojo, K. Hoshino, and H. Okazaki, J. Phys. Soc. Jpn. **67**, 2008 (1998).

[99] F. Shimojo, K. Hoshino, and H. Okazaki, J. Phys. Soc. Jpn. **67**, 2008 (1998).

[100] Y. Nishi, J. Power Sources **100**, 101 (2001).

[101] A. Robertson, A. West, and A. Ritchie, Solid State Ionics **104**, 1 (1997).

[102] K. Takada, Acta Mater. **61**, 759 (2013).

[103] A. West, J. Appl. Electrochem. **3**, 327 (1973).

[104] I. M. Hodge, M. D. Ingram, and A. R. West, J. Am. Ceram. Soc. **59**, 360 (1976).

[105] Y.-W. Hu, I. Raistrick, and R. Huggins, Mater. Res. Bull. **11**, 1227 (1976).

[106] R. A. Huggins, Electrochim. Acta **22**, 773 (1977).

[107] A. Khorassani and A. West, Solid State Ionics **7**, 1 (1982).

[108] A. Khorassani and A. West, J. Solid State Chem. **53**, 369 (1984).

[109] A. West and F. Glasser, J. Mater. Sci. **6**, 1100 (1971).

[110] A. West and F. Glasser, J. Mater. Sci. **5**, 557 (1970).

[111] M. Wakihara, T. Uchida, and T. Gohara, Solid state ionics **31**, 17 (1988).

[112] Y. Saito, T. Asai, K. Ado, H. Kageyama, and O. Nakamura, Solid state ionics **40**, 34 (1990).

[113] Y. Saito, K. Ado, T. Asai, H. Kageyama, and O. Nakamura, Solid state ionics **47**, 149 (1991).

[114] H.-P. Hong, Mater. Res. Bull. **13**, 117 (1978).

[115] P. Bruce and A. West, Mater. Res. Bull. **15**, 379 (1980).

[116] P. Bruce and A. West, J. Solid State Chem. **44**, 354 (1982).

[117] J. Kuwano and A. R. West, Mater. Res. Bull. **15**, 1661 (1980).

[118] J.-i. Yamaki, H. Ohtsuka, and T. Shodai, Solid State Ionics **86**, 1279 (1996).

[119] H. Aono, E. Sugimoto, Y. Sadaaka, N. Imanaka, and G. Adachi, J. Electrochem. Soc.;(United States) **136** (1989).

[120] H. Aono, E. Sugimoto, Y. Sadaoka, N. Imanaka, and G.-y. Adachi, Bull. Chem. Soc. Jpn. **65**, 2200 (1992).

[121] H. Aono, E. Sugimoto, Y. Sadaoka, N. Imanaka, and G.-y. Adachi, Solid State Ionics **62**, 309 (1993).

[122] F. Sudreau, D. Petit, and J. Boilot, J. Solid State Chem. **83**, 78 (1989).

[123] U. v. Alpen, A. Rabenau, and G. Talat, Appl. Phys. Lett. **30**, 621 (1977).

[124] H. Yamane, S. Kikkawa, and M. Koizumi, Solid State Ionics **15**, 51 (1985).

[125] B. Schoch, E. Hartmann, and W. Weppner, Solid State Ionics **18**, 529 (1986).

[126] T. Lapp, S. Skaarup, and A. Hooper, Solid State Ionics **11**, 97 (1983).

[127] H. Obayashi, R. Nagai, A. Gotoh, S. Mochizuki, and T. Kudo, Mater. Res. Bull. **16**, 587 (1981).

[128] G. Nazri, Solid State Ionics **34**, 97 (1989).

[129] N. Kamaya et al., Nat. Mater. **10**, 682 (2011).

[130] M. Matsuo, Y. Nakamori, S.-i. Orimo, H. Maekawa, and H. Takamura, Appl. Phys. Lett. **91**, 224103 (2007).

[131] H. Maekawa et al., J. Am. Chem. Soc. **131**, 894 (2009).

[132] A. West and P. Bruce, J. solid state electrochem., 1995.

[133] M. Matsuo et al., J. Am. Chem. Soc. **131**, 16389 (2009).

[134] P. Vajeeston, P. Ravindran, A. Kjekshus, and H. Fjellvåg, Phys. Rev. B **69**, 020104 (2004).

[135] H. Oguchi et al., J. Appl. Phys. **107**, 096104 (2010).

[136] P. Padma Kumar and S. Yashonath, J. Phys. Chem. B **105**, 6785 (2001).

[137] C. Catlow, Solid State Ionics **8**, 89 (1983).

[138] J. Walker and C. Catlow, Philosophical Magazine A **43**, 265 (1981).

[139] M. Wolf, J. Walker, and C. Catlow, J. Phys. C: Solid State Phys. **17**, 6623 (1984).

[140] M. Wolf and C. Catlow, J. Phys. C: Solid State Phys. **17**, 6635 (1984).

[141] M. Wolf, J. Phys. C: Solid State Phys. **17**, L285 (1984).

[142] C. Satheesan Babu and B. L. Tembe, Chem. Phys. Lett. **194**, 351 (1992).

[143] R. W. Impey, M. L. Klein, and I. R. McDonald, J. Chem. Phys. **82**, 4690 (1985).

[144] R. Impey, M. Klein, and I. McDonald, J. Phys. C: Solid State Phys. **17**, 3941 (1984).

[145] L. W. Strock and V. A. Brophy, Amer. Mineralogist **40**, 94 (1955).

[146] T. Takahashi, K. Kuwabara, and O. Yamamoto, J. Electrochem. Soc. **120**, 1607 (1973).

[147] T. Takahashi, J. Appl. Electrochem. **3**, 79 (1973).

[148] T. Takahashi et al., Pure Appl. Chem. **50**, 1091 (1978).

[149] T. Takahashi and O. Yamamoto, Denki Kagaku,(Tokyo) **32**, 610 (1964).

[150] B. Reuter, J. Pickardt, and K. Hardel, Zeitschrift für Physikalische Chemie **56**, 309 (1967).

[151] T. Takahashi, S. Ikeda, and O. Yamamoto, J. Electrochem. Soc. **119**, 477 (1972).

[152] L. Y. Chan and S. Geller, J. Solid State Chem. **21**, 331 (1977).

[153] B. B. Owens and G. R. Argue, J. Electrochem. Soc. **117**, 898 (1970).

[154] J. Bradley and P. D. Greene, Trans. Faraday Soc. **62**, 2069 (1966).

[155] D. O. Raleigh, J. Appl. Phys. **41**, 1876 (1970).

[156] R. Linford, J. Pollock, and C. Randell, Nature **256**, 398 (1975).

[157] J. Christie, B. B. Owens, and G. Tiedeman, Inorg. Chem. **14**, 1423 (1975).

[158] S. Geller, Science **157**, 310 (1967).

[159] B. B. Owens, J. Electrochem. Soc. **117**, 1536 (1970).

[160] B. B. Owens, J. Christie, and G. T. Tiedeman, J. Electrochem. Soc. **118**, 1144 (1971).

[161] G. Mellors and D. Louzos, J. Electrochem. Soc. **118**, 846 (1971).

[162] H. Wada et al., Solid state ionics **154**, 723 (2002).

[163] M. Onoda, H. Wada, M. Tansho, and M. Ishii, Solid state ionics **113**, 515 (1998).

[164] M. Tansho, H. Wada, M. Ishii, and Y. Onoda, J. Phys. Chem. B **102**, 5047 (1998).

[165] T. Nilges, S. Nilges, A. Pfitzner, T. Doert, and P. Böttcher, Chem. Mater. **16**, 806 (2004).

[166] P. Vashishta and A. Rahman, Phys. Rev. Lett.;(United States) **40** (1978).

[167] F. Shimojo and M. Kobayashi, J. Phys. Soc. Jpn **60**, 3725 (1991).

[168] M. Parrinello, A. Rahman, and P. Vashishta, Phys. Rev. Lett. **50**, 1073 (1983).

[169] J. Tallon, Phys. Rev. B **38**, 9069 (1988).

[170] T. Takeuchi, Phys. Status Solidi B **147**, K9 (1988).

[171] A. Ivanov-Shitz, B. Y. Mazniker, and E. Povolotskaya, Crystallogr. Rep. **47**, 117 (2002).

[172] A. Ivanov-Shitz, B. Y. Mazniker, and E. Povolotskaya, Crystallogr. Rep. **46**, 292 (2001).

[173] S. Kishi et al., J. Electrochem. Soc. **156**, J351 (2009).

[174] M. Zhou and A. Ahmad, Sens. Actuators, B **122**, 419 (2007).

[175] T. Kida et al., Electrochim. Acta **56**, 7484 (2011).

[176] R. Fuentes, F. Figueiredo, F. Marques, and J. Franco, Ionics **8**, 383 (2002).

[177] J. Dekeyser, F. De Schutter, C. Van der Poorten, L. Zhang, and D. Fray, Sens. Actuators, B **24**, 273 (1995).

[178] J. Sudworth and A. Tiley, *Sodium Sulphur Battery*, Springer, 1985.

[179] T. Oshima, M. Kajita, and A. Okuno, Int. J. Appl. Ceram. Technol. **1**, 269 (2004).

[180] X. Lu, G. Xia, J. P. Lemmon, and Z. Yang, J. Power Sources **195**, 2431 (2010).

[181] J. Sudworth, J. Power Sources **51**, 105 (1994).

[182] M. Hosseinifar and A. Petric, J. Power Sources **206**, 402 (2012).

[183] M. A. Evstigneeva, V. B. Nalbandyan, A. A. Petrenko, B. S. Medvedev, and A. A. Kataev, Chem. Mater. **23**, 1174 (2011).

[184] M. Rao, S. Narender Reddy, and A. Sadananda Chary, Physica B **362**, 193 (2005).

[185] W. Bragg, C. Gottfried, and J. West, Z. Krist **77**, 255 (1931).

[186] C. Beevers and M. Ross, Z. Krist **97**, 59 (1937).

[187] G. Yamaguchi and K. Suzuki, Bull. Chem. Soc. Jpn. **41**, 93 (1968).

[188] M. Bettman and C. R. Peters, J. Phys. Chem. **73**, 1774 (1969).

[189] G. E. Youngblood, G. R. Miller, and R. S. Gordon, J. Am. Ceram. Soc. **61**, 86 (1978).

[190] A. V. Virkar, G. R. Miller, and R. S. Gordon, J. Am. Ceram. Soc. **61**, 250 (1978).

[191] Z. Skotniczny, J. MoScinski, and Z. Rycerz, J. Phys. C: Solid State Phys. **19**, 4781 (1986).

[192] M. A. Zendejas and J. O. Thomas, Phys. Scr. **1990**, 235 (1990).

[193] M. A. Zendejas and J. O. Thomas, Phys. Scr. **47**, 440 (1993).

[194] J. Bocquet and G. Lucazeau, Solid state ionics **24**, 235 (1987).

[195] M. S. Whittingham and R. A. Huggins, J. Chem. Phys. **54**, 414 (1971).

[196] J. Beckers, K. Van Der Bent, and S. De Leeuw, Solid State Ionics **133**, 217 (2000).

[197] N. Baffier, J. Badot, and P. Colomban, Mater. Res. Bull. **16**, 259 (1981).

[198] J. Briant and G. Farrington, J. Solid State Chem. **33**, 385 (1980).

[199] S. Park and E. Hellstrom, J. Mater. Sci. **29**, 2425 (1994).

[200] J. Bates et al., Solid State Ionics **5**, 159 (1981).

[201] K. Funke and R. D. Banhatti, J. Mater. Sci. **42**, 1942 (2007).

[202] M. A. Zendejas and J. O. Thomas, Solid State Ionics **28**, 46 (1988).

[203] W. Smith and M. Gillan, J. Phys. Cond. Matter **4**, 3215 (1992).

[204] L. Hagman and P. Kierkegaard, Acta Chem. Scand **22** (1968).

[205] J. Alamo, Solid State Ionics **63**, 547 (1993).

[206] J. Alamo and R. Roy, J. Mater. Sci. **21**, 444 (1986).

[207] N. Anantharamulu et al., J. Mater. Sci. **46**, 2821 (2011).

[208] H.-P. Hong, Mater. Res. Bull. **11**, 173 (1976).

[209] J. Goodenough, H.-P. Hong, and J. Kafalas, Mater. Res. Bull. **11**, 203 (1976).

[210] R. Roy, D. Agrawal, J. Alamo, and R. Roy, Mater. Res. Bull. **19**, 471 (1984).

[211] R. Roy, D. K. Agrawal, and H. A. McKinstry, Annu. Rev. Mater. Sci. **19**, 59 (1989).

[212] B. Scheetz, D. Agrawal, E. Breval, and R. Roy, Waste Management **14**, 489 (1994).

[213] R. Roy, E. Vance, and J. Alamo, Mater. Res. Bull. **17**, 585 (1982).

[214] K. Frank, H. Kohler, and U. Guth, Ionics **14**, 363 (2008).

[215] A. Hetznecker, H. Kohler, U. Schönauer, and U. Guth, Sens. Actuators, B **99**, 373 (2004).

[216] A. Hetznecker, H. Kohler, and U. Guth, Sens. Actuators, B **120**, 378 (2007).

[217] H. Aono, Y. Sadaoka, L. Montanaro, E. Bartolomeo, and E. Traversa, J. Am. Ceram. Soc. **85**, 585 (2002).

[218] D. Woodcock and P. Lightfoot, J. Mater. Chem. **9**, 2907 (1999).

[219] J. O. Evans, J. Chem. Soc., Dalton Trans. , 3317 (1999).

[220] J. Evans, T. Mary, T. Vogt, M. Subramanian, and A. Sleight, Chem. Mater. **8**, 2809 (1996).

[221] T. Mary, J. Evans, T. Vogt, and A. Sleight, Science **272**, 90 (1996).

[222] A. K. Pryde et al., Phase Transitions **61**, 141 (1997).

[223] J. Evans, J. Hanson, and A. Sleight, Acta Crystallogr., Sect. B: Struct. Sci **54**, 705 (1998).

[224] R. Withers, J. Evans, J. Hanson, and A. Sleight, J. Solid State Chem. **137**, 161 (1998).

[225] V. Korthuis et al., Chem. Mater. **7**, 412 (1995).

[226] S. Abrahams, J. M. Reddy, and J. Bernstein, J. Phys. Chem. Solids **27**, 997 (1966).

[227] J. Evans, T. Mary, and A. Sleight, J. Solid State Chem. **137**, 148 (1998).

[228] D. Agrawal, C.-Y. Huang, and H. McKinstry, Int. J. Thermophys. **12**, 697 (1991).

[229] H. Miyazaki et al., Japanese J. Appl. Phys. **47**, 7262 (2008).

[230] S. Limaye, D. Agrawal, and H. McKinstry, J. Am. Ceram. Soc. **70**, C (1987).

[231] V. Pet'kov, K. Kir'yanov, and E. Asabina, Russ. J. Appl. Chem. **77**, 707 (2003).

[232] V. Pet'kov and E. Asabina, Glass Ceram. **61**, 233 (2004).

[233] U. Von Alpen, M. Bell, and W. Wichelhaus, Mater. Res. Bull. **14**, 1317 (1979).

[234] H. Kohler and H. Schulz, Mater. Res. Bull. **20**, 1461 (1985).

[235] H. Kohler, H. Schulz, and O. Melnikov, Mater. Res. Bull. **18**, 1143 (1983).

[236] V. Nicholas, P. Johnson, and A. Kingon, Solid state ionics **17**, 351 (1985).

[237] K. Kreuer and U. Warhus, Mater. Res. Bull. **21**, 357 (1986).

[238] R. Fuentes, F. Figueiredo, F. Marques, and J. Franco, Solid State Ionics **139**, 309 (2001).

[239] M. L. Di Vona, E. Traversa, and S. Licoccia, Chem. Mater. **13**, 141 (2001).

[240] J.-P. Boilot, G. Collin, and P. Colomban, J. Solid State Chem. **73**, 160 (1988).

[241] O. Bohnke, S. Ronchetti, and D. Mazza, Solid State Ionics **122**, 127 (1999).

[242] A. Essoumhi, C. Favotto, M. Mansori, and P. Satre, J. Solid State Chem. **177** (2004).

[243] Y. Saito, K. Ado, T. Asai, H. Kageyama, and O. Nakamura, Solid state ionics **58**, 327 (1992).

[244] E. R. Losilla et al., Chem. Mater. **12**, 2134 (2000).

[245] F. Cherkaoui, G. Villeneuve, C. Delmas, and P. Hagenmuller, J. Solid State Chem. **65**, 293 (1986).

[246] Y. Miyajima, Y. Saito, M. Matsuoka, and Y. Yamamoto, Solid State Ionics **84**, 61 (1996).

[247] K. Shimazu, Y. Yamamoto, Y. Saito, and O. Nakamura, Solid state ionics **79**, 106 (1995).

[248] O. Nakamura, Y. Saito, M. Kodama, and Y. Yamamoto, Solid state ionics **89**, 159 (1996).

[249] J. Boilot, G. Collin, and P. Colomban, Mater. Res. Bull. **22**, 669 (1987).

[250] R. Cava, E. M. Vogel, and D. W. Johnson, J. Am. Ceram. Soc. **65**, c157 (1982).

[251] J.-M. Winand, A. Rulmont, and P. Tarte, J. Solid State Chem. **93**, 341 (1991).

[252] F. Cherkaoui, J. Viala, C. Delmas, and P. Hagenmuller, Solid State Ionics **21**, 333 (1986).

[253] P. Yadav and M. Bhatnagar, J. Electroceram. , 1 (2013).

[254] N. Imanaka, M. Itaya, T. Ueda, and G. Adachi, Solid State Ionics **154**, 319 (2002).

[255] N. Imanaka, T. Ueda, and G.-y. Adachi, J. Solid State Electrochem. **7**, 239 (2003).

[256] S. Tamura, N. Imanaka, and G. Adachi, Solid state ionics **136**, 423 (2000).

[257] Y. Hasegawa and N. Imanaka, Solid state ionics **176**, 2499 (2005).

[258] D. Mazza, J. Solid State Chem. **156**, 154 (2001).

[259] P. P. Kumar and S. Yashonath, J. Am. Chem. Soc. **124**, 3828 (2002).

[260] P. P. Kumar and S. Yashonath, J. Phys. Chem. B **106**, 7081 (2002).

[261] D. T. Qui, J. Capponi, J. Joubert, and R. Shannon, J. Solid State Chem. **39**, 219 (1981).

[262] D. T. Qui et al., Solid State Ionics **3**, 219 (1981).

[263] S. H. Jacobson, M. A. Ratner, and A. Nitzan, Phys. Rev. B **23**, 1580 (1981).

[264] P. Colomban, Solid State Ionics **21**, 97 (1986).

[265] P. Lacorre, A. Selmi, G. Corbel, and B. Boulard, Inorganic chemistry **45**, 627 (2006).

Chapter 2

Methodology

2.1 Introduction

Most of the scientific problems in nature cannot be solved analytically; for example a classical system of three particles interacting through the simple gravitational force can not be solved analytically. So in the study of material science where interaction of large number of atoms are to be dealt with, it is impossible to handle it analytically, rather has to be solved using suitable computational/numerical techniques.

Computer simulation started as a tool to exploit the electronic computing machines that had been developed during and after the second world war. Then computers were used in the development of nuclear weapons and code breaking. In 1952 the first non-military problem, *numerical simulation of dense liquids* was performed by Metropolis et al.[1] on the MANIAC computer at Los Alamos, employing a technique now renowned as Metropolis Monte Carlo method. This method was idealized for hard sphere type molecules but within a few years Monte Carlo technique were carried out for the Lennard-Jones interactions[2]. This method was implemented in simulation of liquid Argon and the results were in agreement with experiments.

For dynamic properties a different method by name molecular dynamics (MD) has been used to describe the classical equations of motions.

MD was first accomplished on the phase transition study of hard spheres by Alder and Wainwright [3] in 1957 where the particles move at a constant velocity between perfectly elastic collisions. Later Gibson et al. employed MD simulation to study radiation damage in a Cu target in 1960 using Born-Mayer interaction potential. In 1964 Rahman [4] carried out molecular dynamics simulation for a system of Lennard-Jones particles. Berne [5] extended the study to di-atomic molecular liquid. These studies were followed by the attempts to model liquid water, which continues to be one of the most challenging and interesting systems even today [6–8].

MD simulations are now widely employed in different fields of science. In the field of biochemistry, the technique is extensively employed in drug design, structure of membranes and bio-molecules. Molecular dynamics finds its utility in the study of structure, dynamics and conformations of of long chain molecules such as flexible hydrocarbons [9], proteins [10] and polymers. The exciting area of protein folding is another field where MD simulation contributed significantly to our understanding. Recently one microsecond simulation of few steps of the folding of villin headpiece has been studied which is one of the fastest folding proteins [11]. This technique has been used extensively to study phase transition behavior, correlated motion in many body systems, thin film growth, surface reconstruction, study of defects and their interactions, microscopic mechanism of fracture, defect interactions, interfaces etc. [12–14]. There are numerous MD studies of superionic conductors; some of which will be discussed later in this chapter [15].

In the last three decades the field witnessed several important methodological developments, and presently of atomistic simulation techniques are available in a variety of ensembles, such as NVE-MD, NVT-MD, NPT-MD, NPT-MC etc. These methods are developed to make direct comparisons with experimental conditions or to suit the problem at hand. Some of these advanced simulation techniques are employed in the studies described in the thesis, and are briefly outlined below.

2.2 Molecular Dynamics

Molecular Dynamics (MD) involves numerical solution of the classical equation of motion for every single atom in a collection of atoms representing the material of interest. The result is a very detailed description of the temporal evaluation of the dynamical quantities in the system. Typically the positions and velocities of atoms are stored over a period of time, which are later analyzed for structural, dynamical and thermodynamics properties of interest. In classical molecular dynamics the atoms are treated as point particles, ignoring electronic degrees of freedom, and are assumed to interacts with each other through an effective interatomic potential that is characteristic of the system. Molecular dynamics simulation can be extended to different ensemble such as microcanonical (NVE-MD), canonical(NVT-MD) and isobaric isothermal (NPT-MD) etc. In our studies NVE and NPT-MD simulations have been used.

2.2.1 Microcanonical molecular dynamics (NVE-MD)

In this ensemble the total energy, number of atoms and volume of the cell remain conserved. Molecular dynamics implementation in NVE ensemble is most straightforward. The force on each atom is calculated by summing up the force on that atom due to all other atoms in the system through the equation,

$$\bar{F}_i = \sum_{\substack{j=1 \\ j \neq i}}^{N} \bar{F}_{ij}\,(r_{ij}) \tag{2.1}$$

where r_{ij} is the interatomic distance between a pair of atoms labelled i and j, and N is the total number of atom in the system. The force $\bar{F}_{ij}$ between the pair i and j is calculated as the first derivative of interatomic potential between the two particle $u_{ij}(r_{ij})$,

$$F_{ij}^{\alpha} = -\frac{\partial u_{ij}}{\partial r_{ij}}\left(\frac{\alpha_j - \alpha_i}{r_{ij}}\right) \tag{2.2}$$

where α stands for the different Cartesian components, $\alpha = x,\ y$ and z. Now the acceleration of the i^{th} atom with mass m_i can be calculated through the equation,

$$\bar{a}_i^{\alpha} = \bar{F}_i^{\alpha}/m_i \tag{2.3}$$

The simulations are started from an initial set of positions and velocities of all particles. From initial positions acceleration is calculated and position and velocities are integrated to get the value for next time step. There are different schemes available for integration. Among them simplest is the Verlet algorithm [16] where the equations for position and time at the next time step $t + \delta t$ are given by,

$$\begin{aligned} \bar{r}(t+\delta t) &= 2\bar{r}(t) - \bar{r}(t-\delta t) + \frac{d^2\bar{r}(t)}{dt^2}\delta t \\ \bar{v}(t+\delta t) &= \frac{\bar{r}(t+\delta t) - \bar{r}(t-\delta t)}{2\delta t} \end{aligned} \tag{2.4}$$

δt is the time step that is in the order of femto seconds ($10^{-15}s$). But the disadvantages of this algorithm is the velocity does not appear explicitly in the equation of motion, instead calculated through typical first order central difference method. Another disadvantage is that it is a two step method, as the positions at time $t + \delta t$ requires the positions at two previous time steps.

2.2.1.1 Velocity-Verlet Algorithm

In our study Velocity Verlet algorithm has been used to integrate the equation of motion. This set of algorithm needs less memory because only one set of positions, velocities and accelerations need to be stored at a time. Let the positions and velocities of atoms at time t are $\bar{r}(t)$ and $\bar{v}(t)$. The accelerations of atoms, $\bar{a}(t)$, are calculated from eqn. 2.3. The velocity verlet algorithm consists of four steps as follows[16, 17],

1. The first step is to calculate the velocity at the mid time step $(t + \delta t/2)$ using,

$$\bar{v}(t + \delta t/2) = \bar{v}(t) + \frac{1}{2}\bar{a}(t)\delta t \tag{2.5}$$

2. The next step is to calculate the position of the atoms at time step $(t + \delta t)$ as,

$$\bar{r}(t + \delta t) = \bar{r}(t) + \bar{v}(t + \delta t/2)\delta t \tag{2.6}$$

3. Now the acceleration at the next time step $\bar{a}(t + \delta t)$ is calculated from the updated positions $\bar{r}(t + \delta t)$ using 2.3,

4. The final step is to calculate the velocity at $t + \delta t$ with the help of the equation,

$$\bar{v}(t + \delta t) = \bar{v}(t + \delta t/2) + \frac{1}{2}\bar{a}(t + \delta t)\delta t \tag{2.7}$$

Now the positions and velocity of the atom at time $t + \delta t$ is available. Repeating these four steps successively for all the atoms, the trajectory of atoms are generated.

2.2.1.2 Velocity scaling

The MD algorithm explained above do not have any control on the temperature of the system. To simulate a system in microcanonical MD (NVE-MD) at a particular temperature velocity scaling method is employed. Suppose at a particular MD step the instantaneous temperature is T_{in} and the required temperature for the simulation is T_{re}. According to classical statistical mechanics there is an average energy of $k_B T/2$ associated with each degree of freedom that appears as a squared term in the Hamiltonian,

$$H = \sum_{i=1}^{N} u(\bar{r}_1, \bar{r}_2, ..., \bar{r}_N) + \frac{1}{2}\sum_{i=1}^{N} m_i v_i^2 \tag{2.8}$$

In the system of N atoms there are 3N velocity degrees of freedom, and each one appears as $\frac{1}{2}m_i v_i^2$ in the kinetic energy term of the Hamiltonian H. Then the instantaneous kinetic energy

of the system can be written as,

$$K = \frac{3\,N\,k_B T}{2} = \frac{1}{2}\sum_{i=1}^{N} m_i v_i^2 \tag{2.9}$$

According to the eqn. 2.9 the instantaneous and required temperatures are,

$$\begin{aligned} T_{in} &= \frac{\sum_{i=1}^{N} m_i (v_i^{in})^2}{3Nk_B} \\ T_{re} &= \frac{\sum_{i=1}^{N} m_i (v_i^{re})^2}{3Nk_B} \end{aligned} \tag{2.10}$$

To get the desired temperature T_{re}, velocities of each atom should be multiplied by the scale factor ($S.F$) calculated from the equation,

$$S.F = \frac{v_i(re)}{v_i(in)} = \sqrt{\frac{T_{re}}{T_{in}}} \tag{2.11}$$

In simulations typically after every 10 MD steps the temperature deviation from the T_{re}, $\delta T = |T_{re} - T_{in}|$, is calculated. A certain tolerance range in the deviation of temperature δT_{tol} is set (typically, $\delta T_{tol} = 10\%\ T_{re}$). If the deviation in temperature δT exceeds δT_{tol}, the velocities of the atoms are scaled according to eqn. 2.11. It must, however, be mentioned that the scaling of velocities are performed only in the initial stage of the simulation, which is followed by the 'equilibration phase' when the system is let to evolve with out any perturbation. The statistical averages of quantities are performed in the final stage of simulation, sometimes referred to as the 'production phase', which follows the 'equilibration phase'.

2.2.2 Isobaric-Isothermal Molecular Dynamics (NPT-MD)

The isobaric-isothermal molecular dynamics has been performed by time integration of Nose-Hoover style extended Hamiltonian equations which are designed to generate positions and velocities sampled from the isothermal isobaric (NPT) ensemble. To simulate in the NPT

ensemble some additional dynamic variable are coupled to the particle velocities (for thermostatting) and with simulation domain dimensions (for barostatting). The equations of motions are used from the hydrostatic equations of Martyana [18] with the strain energy proposed by Parrinelo and Rahaman [19]. The method permits fluctuations of both volume and shape of the simulation cell. The equations of motions used in this case are,

$$\begin{aligned} \dot{r_i} &= \frac{p_i}{m_i} + \frac{\overleftrightarrow{p_g}}{W_g} r_i \\ \dot{p_i} &= F_i - \frac{\overleftrightarrow{p_g}}{W_g} p_i - \left(\frac{1}{N_f}\right) \frac{Trace\,[\overleftrightarrow{p_g}]}{W_g} p_i - \frac{p_\xi}{Q} p_i \end{aligned} \tag{2.12}$$

where r_i, p_i, F_i, m_i are the particle velocity, momenta, force and mass of the particle respectively. $\overleftrightarrow{p_g}$ is the cell variable momentum matrix and W_g is the mass of the barostat. For dynamics of the thermostat a fictitious particle is added to the system associated with the variable s. ξ is defined as,

$$\xi = \frac{\log s}{N_f} \tag{2.13}$$

p_ξ is the momenta and Q is the mass associated with the thermostat. d is the dimensionality and N_f is the degrees of freedom of the system.

$$\begin{aligned} \dot{\overleftrightarrow{h}} &= \frac{\overleftrightarrow{p_g}\,\overleftrightarrow{h}}{W_g} \\ \dot{\overleftrightarrow{p_g}} &= V(\overleftrightarrow{P}_{int} - \overleftrightarrow{I} P_{ext}) + \left[\frac{1}{N_f} \sum_{i=1}^{N} \frac{p_i^2}{m_i}\right] \overleftrightarrow{I} - \frac{p_\xi}{Q} \overleftrightarrow{p_g} \\ \dot{\xi} &= \frac{p_\xi}{Q} \\ \dot{p_\xi} &= \sum_{i=1}^{N} \frac{p_i^2}{m_i} + \frac{1}{W_g} Trace[\overleftrightarrow{p_g}^t][\overleftrightarrow{p_g}] - (N_f + d^2) K_B T \end{aligned} \tag{2.14}$$

The internal pressure tensor P_{int} is defined as,

$$(P_{int})_{\alpha\beta} = \frac{1}{V}\left[\sum_{i=1}^{N}\frac{(p_i)_\alpha (p_i)_\beta}{m_i} + (F_i)_\alpha (r_i)_\beta - (\overrightarrow{\phi}'\overrightarrow{h}^t)_{\alpha\beta}\right]$$

$$(\phi')_{\alpha\beta} = \frac{\partial\phi(r, \overleftrightarrow{h})}{\partial(h)_{\alpha\beta}} \tag{2.15}$$

where α and β are the Cartesian components, x, y and z. ϕ is the interatomic potential which is a function of the co-ordinates of the particle and ϕ' is the first order derivative of inter-atomic potential function ϕ with respect to $\overleftrightarrow{h}$ matrix. The volume of the simulation cell can be obtained from determinant of $\overleftrightarrow{h}$ matrix,

$$V = det[\overleftrightarrow{h}] \tag{2.16}$$

where

$$h = \begin{bmatrix} a & b_x & c_x \\ 0 & b_y & c_y \\ 0 & 0 & c_z \end{bmatrix} \tag{2.17}$$

a, b and c are the lattice parameters, b_x, b_y, c_x, c_y and c_z are the projection of lattice parameters along x, y, and z directions. In this eqn. 2.17, the a parameter of the cell is chosen along x-axis and b in the x-y plane.

The conserved quantity in this case is the extended Hamiltonian,

$$H' = \sum_{i=1}^{N}\frac{p_i^2}{m_i} + \frac{1}{2W_g}Trace[\overleftrightarrow{p_g}^t][\overleftrightarrow{p_g}] + \frac{p_{\xi^2}}{2Q} + \phi(r, \overleftrightarrow{h}) + P_{ext}det[\overleftrightarrow{h}] + (N_f + d^2)K_BT\xi \tag{2.18}$$

P_{ext} and T are the desired pressure and temperature. The first three terms in the equation 2.18 associated with the various kinetic energy terms associated with the N atoms, the barostat variables and the thermostat respectively. The final three terms represents the potential energy contribution from the N particle system, barostat and the thermostat, respectively.

2.3 NPT Monte Carlo

Monte Carlo (MC) methods are stochastic techniques means they are based on the use of random numbers and probability statistics to investigate problems. In classical Monte Carlo, samples are drawn from Boltzmann probability distribution. This method is very powerful in the study of structural phase change but does not provide any dynamical information related to the system. In our studies we use the *importance sampling* algorithm where the configurations of atoms are chosen according to the desired statistical ensemble. The importance sampling method involves selections of samples those contribute most to the statistical average. Sampling must ensure all relevant elements of the ensemble are varied. The ensemble average of the observable A in the NPT ensemble is [16] given by,

$$\langle A_{NPT} \rangle = \frac{\int A(\bar{s}^N) e^{-\beta u(\bar{s}^N)} d\bar{s}^N \int_0^\infty V^N e^{-\beta PV} dV}{Z} \tag{2.19}$$

where Z is the partition function defined as,

$$Z_{NPT} = \int e^{-\beta u(\bar{s}^N)} d\bar{s}^N \int_0^\infty V^N e^{-\beta PV} dV \tag{2.20}$$

where N is the total number of atoms, u is the potential energy, V, P and T are the volume, constant pressure and temperature of the system respectively. $\bar{s}$ is the scaled positions of atoms ($\bar{s}1, \bar{s}2, \bar{s}3, ..., \bar{s}N$) defined as,

$$\bar{s} = h^{-1}\bar{r} \tag{2.21}$$

where $\bar{r}$ is the Cartesian position vector of atoms ($\bar{r}1, \bar{r}2, \bar{r}3, ..., \bar{r}N$). h^{-1} is the inverse of h matrix, which transforms the real co-ordinates into scaled co-ordinates (see equation 2.17).

The Metropolis scheme is implemented by generating a Markov chain of states which has the limiting probability distribution,

$$P \propto e^{(-\beta u + PV + N \log V)} \tag{2.22}$$

Suppose the initial state of configuration of the system has the potential energy $u_o(r^N)$ and volume $V_o(a, b, c, \alpha, \beta, \gamma)$. Where a, b, c, α, β and γ are the initial cell edges and angles. To simulate NPT ensemble the co-ordinate space of the atoms as well as the lattice parameters space of the simulation cell need to be sampled. In the present work this has been done in two steps first the coordinate space of the atoms has been sampled keeping the lattice parameters fixed then in the second step the lattice parameters has been sampled. It should be mentioned that with the change in lattice parameters the co-ordinates of the atoms have to be scaled again according to the new set of lattice parameters which will automatically bring in the change in total interatomic potential energy.

2.3.1 Sampling of coordinate space

To generate a new configuration of the system, an atom chosen at random is displaced along x, y and z co-ordinates randomly by,

$$\alpha_n = \alpha_o + \rho * (2 * ran(\alpha) - 1) \tag{2.23}$$

where $\alpha = x, y$ or z are the Cartesian coordinates and α_o, α_n represents the coordiantes before and after the move respectively [16]. ρ is a parameter which defines the maximum magnitude of displacement in a single trial move.

Let the energy corresponding to new and old configuration is u_n, u_o respectively. If the energy difference between the two states, $\delta u = (u_n - u_o)$, is negative then the new configuration is accepted. But if δU is positive then the move is accepted with a probability equal to the ratio of probabilities of these two states, $P(o \rightarrow n) = e^{-\beta \delta u}$. That is, the probability factor $P(o \rightarrow n)$ calculated is compared with a random number between zero and one; and the move is accepted only if $P(n \rightarrow o)$ greater than the random number generated, else the move rejected. Then this method is implemented to all the atoms in the system, starting from a randomly picked

one, and then serially progressing to all the rest. An *MC step* refers to attempts to move all the atoms in the system. This way co-ordinates space is sampled in metropolis algorithm.

The choice of the parameter ρ influence the convergence of the Markov chain. If ρ is very small then nearly all the moves are accepted but the configuration space are sampled very slowly. Again ρ is set too large then most of the moves are rejected and movement in phase space became very slow. So ρ is chosen such a way that roughly 40-50% of the trial moves are accepted [16]. Essentially different ρ values have been assigned for the different types of atoms depending on the their mobility.

Upto this point the algorithm sampled only the coordinate space of the atoms but in NPT ensemble box volume and shape too has to be sampled which will be discussed in the next step.

2.3.2 Sampling of volume and shape

$a, b, c, \alpha, \beta, \gamma$ are six degrees of freedom corresponding to size and shape of the simulation box. After a certain number of MC steps involving attempted coordinate displacements, the lattice parameters are changed with similar equations 2.23. Then again the new energy u_n and volume V_n is calculated corresponding to new lattice parameters. It should be mentioned that the total potential energy will be modified according to the new set of lattice parameters as the h matrix of eqn. 2.21 gets modified according to the lattice parameters. Then the difference in the quantity in this case is,

$$\delta H = (u_n - u_o) + P(V_n - V_o) + \frac{N}{\beta} ln\left(\frac{V_n}{V_o}\right) \tag{2.24}$$

If δH is negative then the new configuration is accepted. If δH is positive, ratio of probability of these two states, $P(o \rightarrow n)_{(lt)} = e^{-\beta \delta H}$ is calculated. If the random number is less than the factor $P(o \rightarrow n)$ then the move is accepted otherwise rejected. In this case also ρ parameter for different cell edges can be different, and are chosen according to the acceptance ratio of 40-50%.

2.4 Periodic Boundary Condition

Suitable periodic boundary conditions (PBC) are employed in all bulk simulation used to remove the surface effects to simulate bulk properties of the system. Typical number of atoms in a bulk system is of the order of $\approx 10^{23}$ while in computer simulation the number of atoms used is typically in the range of $\approx 1000 - 10000$ (of length $\approx 20 - 40\mathring{A}$). The significance of imposing periodic boundary conditions while dealing with such a small system can be argued by simple considerations. Consider a sphere of radius r and a spherical shell of very small width dr. The ratio of surface atoms N_{surf} to the total number of atoms N_{tot} can be calculated by,

$$\frac{N_{surf}}{N_{tot}} = \frac{4\pi r^2 dr\rho}{\frac{4}{3}\pi r^3\rho} = 3\frac{dr}{r}. \tag{2.25}$$

This ratio for bulk system is roughly $\approx 3\frac{3\mathring{A}}{10^8\mathring{A}} \approx 10^{-7}$ while in typical simulation the ratio is much higher $\approx 3\frac{3\mathring{A}}{20\mathring{A}} \approx 0.45$. Thus a larger fraction of atoms are on the surface and the surface atoms in typical simulation feel different atmosphere than the atoms which are deep inside the system.

Applying periodic boundary condition this surface effect can be removed. In this method original simulation cell is surrounded by replicas of the original simulation cell. For a orthogonal simulation cell (with sides L_x, L_y, L_z), image co-ordinates can be created by these equations,

$$\begin{aligned} x' &= x_{simu} + n_x L_x \\ y' &= y_{simu} + n_y L_y \\ z' &= z_{simu} + n_z L_z \end{aligned} \tag{2.26}$$

where n_x, n_y, n_z are integers, positive or negative including zero. The image particles interact with the atoms in the simulation cell. Now the surface atoms in the original simulation feels similar atmosphere as the atoms at the center of the original simulation cell. It is always better to add more number of image cell to achieve more accurate result but it would be then

very expensive in terms of computational time as the required computational time increases in proportion to square of the number of particles used in the simulation[16]. To limit the number of interactions between atoms a cut-off distance R_c is chosen such that the potential energy contribution beyond this distance can be neglected with out affecting the properties of the simulation much. If the original cell is large enough such that $R_c \leq \frac{L}{2}$ then a particle of the simulation cell i should interact with another particle j or one of its image but not the both of them. This is called minimum image convention. Of course, there may be cases where i will interact neither j nor its image. For non orthogonal simulation box the real coordinates should be transformed to scaled coordinates using the h matrix as in eq. 2.21. Scaled co-ordinates are the coordinates in a orthogonal simulation box with sides of unit length. Then PBC can be implemented on these scaled co-ordinates according to eqn. 2.26 and then transformed into real co-ordinates with the help of h matrix through the equation,

$$\bar{r} = h\bar{s} \tag{2.27}$$

2.5 Interatomic potential

Interatomic potentials plays the most crucial role in computer simulation. The property extracted from computer simulation depends on the accuracy of the potential and is vital to reproduce the properties of the system. Interatomic potentials are typically functions of distance between two atoms (assuming only pair wise interaction neglecting the many body interaction terms). Interatomic potentials contains mainly two parts one attractive and another repulsive. They can further be short ranged or long ranged ($\frac{1}{r^n}$, where $n \leq 3$). Some of the widely employed short-ranged potentials are Lennard-Jones, Born-Mayer, Vashistha Rahaman etc. The form of the Lennard-Jones potential is,

$$u(r_{ij}) = 4\epsilon\left[\left(\frac{\sigma}{r_{ij}}\right)^{12} - \left(\frac{\sigma}{r_{ij}}\right)^{6}\right] \tag{2.28}$$

where $|r_{ij}|$ is the interatomic distance between particle i and j. σ is a measure of the diameter of the particle. ϵ is the measure of the depth of the pair potential at the equilibrium position of the pair potential. This potential has been used to simulate inert gases such as argon [20, 21]. However for certain ionic solids Lennard Jones potential has been used with an additional coloumbic term [22]. The repulsive part of the Lennard-Jones potential goes like $\frac{1}{r^{12}}$ which describes the Pauli's repulsive term at short distances due to the overlap of electron clouds. And $\frac{1}{r^6}$ is the attractive term arises due to the interaction between instantaneous dipoles.

Born Mayer Huggins (BMH) potential[23] is one of the most popular potentials for simulation of ionic alkali halides, has the functional form,

$$u(r_{ij}) = \frac{q_i q_j}{r_{ij}} + A_{ij} e^{-\frac{r_{ij}}{\rho_{ij}}} - \frac{C_{ij}}{r_{ij}^6} - \frac{D_{ij}}{r_{ij}^8} \tag{2.29}$$

where q_i is the charge of the ion, A_{ij}, C_{ij}, D_{ij} is the overlap repulsive energy, instantaneous dipole-dipole attractive term, dipole-quadropole interaction term, respectively. In this potential exponentially decaying term has been used for the repulsive part which has a stronger theoretical basis than the $\frac{1}{r^{12}}$ term of Lennard-Jones (eqn. 2.28). BMH potential have been used widely in the simulation of several inorganic solids and molten salts [24–26]. Simulation studies on superionic solids such as, β-alumina[27], Li_3N[28], $SrCl_2$[29], CaF_2 [30, 31], $LiMn_2O_4$[32], $Gd_2Zr_2O_7$[33] etc. employed BMH potential.

Vashistha and Rahaman[34] introduced a new potential function of the form,

$$U_{ij} = \frac{q_i q_j}{r_{ij}} - \frac{1}{2}\frac{(\alpha_i q_j^2 + \alpha_j q_i^2)}{r_{ij}^4} + A_{ij}\frac{(\sigma_i + \sigma j)^{n^{ij}}}{r_{ij}^{n_{ij}}} - \frac{C_{ij}}{r_{ij}^6} \tag{2.30}$$

in their study of one of the well known superionic conductor $\alpha - AgI$. Where α_{ij} is the polarizability, σ_i is the ionic radius and the other parameters have the same meaning as in the previous eqn. 2.30. This potential has been used successfully in the study of several other super ionic conductors such as Ag_2Se, UO_2 also [35–37].

2.6 Ewald Summation

While dealing with long ranged forces, such as the Coulomb force, special care is needed such that the potential and forces converges. For the calculation of Coloumbic contribution to the potential energy cut off R_c cannot be used in the usual fashion. In the presence of Columbic interaction original simulation cell and all its images must be considered. In principle for large enough systems screening by the neighboring atoms would diminish the effect of the potential, however this would occur over a range of several of ten or hundred of nanometers. But dealing with such large simulation cells become prohibitively expensive. So to include the long range interactions the contribution from all the periodic images must be included. Ewald summation[14] technique has been implied for calculation contribution from coloumbic interaction[14].

The effective potential for coloumbic interaction due to a set of point charges upon a charged particle q_i,

$$u_i = \frac{1}{4\pi\epsilon_0} \sum_n \sum_{j=1}^{N} \frac{q_j}{|\bar{r}_{ij} + n\bar{l}|} \tag{2.31}$$

where $\bar{l} = (l_x, l_y, l_z)$ and are the lattice vectors. The sum is over all the periodic images n and over all particles j, except for $j = i$ when $n = 0$ (that is, the self interaction is excluded).

The total Coloumbic contribution then to the potential energy of this N particle system is,

$$u_C = \frac{1}{2} \sum_{i=1}^{N} q_i u_i \tag{2.32}$$

The sum in eqn. 2.31 is only conditionally convergent. Ewald summation technique has been used to converge the eqn. 2.32. In this technique the charge density of the equation has been rewritten. In eqn. 2.31 the charge density have been represented as a sum of δ-functions (the charge density of point charge is a δ-function).

Now the assumption in this technique is to consider a diffuse charge distribution of opposite sign surrounding the charge particle i with charge q_i such that the total charge of the cloud exactly cancels q_i. Thus the potential due to the δ-function is now screened. This screened potential rapidly goes to zero at large distances. The rate of decay of this fraction depends on the functional form of the screened charge and what follows a Gaussian charge distribution has been assumed for the screening charges. But the aim is to calculate the contribution from the point charges not screened charges. Hence to correct for the screening charge cloud, to every particle, a compensating Gaussian charge with opposite sign to the screening (Gaussian) charge has been included.

Now the electrostatic potential at the point charge q_i due to point charge q_j will have three parts

1. One due to the point charge q_j.
2. Secondly the one due to the screening Gaussian charge cloud with charge $-q_j$.
3. Finally the compensating charge cloud distribution with charge q_j.

To calculate the total potential energy contribution at the point charge q_i the contributions from all the three above mentioned term has to be added for all the atoms in the simulation cell and all its periodic images except for the ion itself to avoid self coloumbic interaction. But it is convenient to calculate the interaction of the compensating charge of particle i with charge q_i and subtract the resultant spurious interaction afterwards. The compensating charge cloud is retained because this will make compensating charge distribution not only smoothly varying but also periodic, which will be essential for numerical implementation also. The potential of the screened point charge is short range in nature and calculated in real space. The remaining contribution from the periodic compensating Gaussian charge is calculated in the Fourier space.

Now the contribution from each term can be calculated as follows.

2.6.1 Short-range part

The potential due to the screened point charged is short range in nature. Consider the expression for screening Gaussian charge distribution around the charge q_j is $\rho(r) = -q_j(\frac{\alpha}{\pi})^{\frac{3}{2}}e^{-\alpha r^2}$. The potential at a distance r from the center of this Gaussian charge distribution using Poisson's equation can be written as,

$$u_{gs} = -\frac{q_j}{r}erf(\sqrt{\alpha}r) \tag{2.33}$$

where

$$erf(x) = (\frac{2}{\sqrt{\pi}})\int_0^x e^{-u^2}du$$

is the *error function*. The contribution of screened point charge u_{scr} is simply at a distance r from the point charge is,

$$u_{scr} = u_{point} + u_{gs} = \frac{q_j}{r} - \frac{q_j}{r}erf(\sqrt{\alpha}r) = \frac{q_j}{r}\,erfc(\sqrt{\alpha}r) \tag{2.34}$$

where

$$erfc(x) = 1 - erf(x)$$

is the *complementary error function*. The total contribution of the short-range potential for the whole system u_{srt} is,

$$u_{srt} = \frac{1}{2}\sum_{i\neq j}^{N}\frac{q_iq_j\,erfc(\sqrt{\alpha}r_{ij})}{r_{ij}} \tag{2.35}$$

Here the summation goes over only the atoms for which the interatomic distance r is less than the cut-off distance R_c.

The potential of a Gaussian charge cloud of total charge q_j at its center u_{cnt} can be obtained by putting $r = 0$ in the eqn. 2.33 which is,

$$u_{cnt}(r=0) = 2q_j\left(\frac{\alpha}{\pi}\right)^{\frac{1}{2}} \tag{2.36}$$

This is the correction term should be subtracted from the total contribution of the potential as in the calculation of compensating charge the self interaction has been overestimated.

The total self correction term for the entire system u_{cr} is,

$$u_{cr}(r=0) = \frac{1}{2}\sum_{i=1}^{N} 2q_i^2 \left(\frac{\alpha}{\pi}\right)^{\frac{1}{2}} = \left(\frac{\alpha}{\pi}\right)^{\frac{1}{2}} \sum_{i=1}^{N} q_i^2 \tag{2.37}$$

2.6.2 Long-range part

The potential energy contribution from the compensating Gaussian charge distribution is calculated in Fourier space. The properties of Poisson's equation has been applied to calculate the contribution of compensating Gaussian charge distribution. The total charge distribution of a periodic sum of Gaussians can be written as,

$$\rho_1(r) = \sum_{j=1}^{N} \sum_{n} q_j \left(\frac{\alpha}{\pi}\right)^{\frac{3}{2}} e^{\left[-\alpha|r-(r_j+nL)|^2\right]} \tag{2.38}$$

Fourier transforming the charge density $\rho_1(k)$ yields,

$$\rho_1(k) = \sum_{j=1}^{N} q_j e^{-ik.r_j} e^{-k^2/4\alpha} \tag{2.39}$$

Poisson equation in Fourier space takes the form,

$$k^2\phi_1(k) = 4\pi\rho_1(k) \tag{2.40}$$

Now putting the value of $\rho_1(k)$ in eqn. 2.40, the potential for this charge distribution(see eqn. 2.38) in Fourier space $\phi_1(k)$ can be obtained as,

$$\phi_1(k) = \frac{4\pi}{k^2} \sum_{j=1}^{N} q_j e^{-ik.r_j} e^{-k^2/4\alpha} \tag{2.41}$$

It should be noted that this expression is defined for only $k \neq 0$. This is a direct consequence of the conditional convergence of the Ewald sum. The value of this expression for $k = 0$ is assumed to be zero. Now the potential at real space $\phi_1(r)$ can be obtained by Fourier transformation of the potential at k space $\phi_1(k)$ through these equations,

$$\begin{aligned}\phi_1(r) &= \frac{1}{V}\sum_{k\neq 0}\sum_{j=1}^{N}\phi_1(k)e^{ik.r} \\ &= \sum_{j=1}^{N}\sum_{k\neq 0}\frac{4\pi}{k^2V}q_j e^{-ik.(r-r_j)}e^{-k^2/4\alpha}\end{aligned} \tag{2.42}$$

Hence the total contribution of long range potential u_{tl}

$$u_{tl} = \frac{1}{2}\sum_i q_i\phi_1(r_i) = \frac{1}{2V}\sum_{k\neq 0}\frac{4\pi}{k^2}|\rho(k)|^2 e^{-k^2/4\alpha} \tag{2.43}$$

where $\rho(k) = \sum_{i=1}^{N} q_i e(ik.r_i)$

So the total coloumbic contribution u_c to the potential energy of the system can be obtained by summing equations 2.35, 2.37 and 2.43, as,

$$u_c = \frac{1}{2}\sum_{i\neq j}^{N}\frac{q_i q_j\, erfc(\sqrt{\alpha}r_{ij})}{r_{ij}} + \sum_{k\neq 0}\frac{4\pi}{k^2}|\rho(k)|^2 e^{-k^2/4\alpha} + \left(\frac{\alpha}{\pi}\right)^{\frac{1}{2}}\sum_{i=1}^{N}q_i^2 \tag{2.44}$$

2.7 Property Calculation

2.7.1 Thermodynamic Properties

Thermodynamic properties of the system such as, total energy, temperature, pressure of the system can be calculated as time averages during the simulation. A variety of other quantities, such as for example, the specific heats at constant volume (C_V) and constant pressure (C_P), are calculated from the fluctuations of temperature, total energy or enthalpy [16] as,

$$C_V(NVE) = \frac{k_B}{\frac{2}{3N} - \frac{<T^2> - <T>^2}{<T>^2}} \tag{2.45}$$

$$C_V(NVT) = \frac{1}{k_B T^2}(< E^2 > - < E >^2) \tag{2.46}$$

$$C_P(NPT) = \frac{1}{k_B T^2}(< H^2 > - < H >^2) \tag{2.47}$$

where E, P, *and* V are the total energy, pressure and volume; and $H = E + PV$ is the enthalpy of the system.

2.7.2 Radial Distribution function

The radial distribution function (RDF) is a useful tool to describe the structure of a system. In a solid, the RDF has an infinite number of sharp peaks whose separations and heights are characteristic of the lattice structure. RDF provides probability of finding a pair of atoms at a distance r apart, relative to the probability expected for a completely random distribution at the same density. The mathematical expression of RDF between pair of atom i and j is,

$$g(r) = \frac{V}{N^2}\langle(\sum_i \sum_{j \neq i} \delta(r - r_{ij})\rangle \tag{2.48}$$

This form can be used to find $g(r)$ in computer simulation replacing the delta function within very small bins. The neighbors around each atom or molecule are sorted into bins of distance dr.

Suppose there are two types of particles i and j of number n_1 and n_2 respectively in the simulation cell of volume V. The number of j type of atoms calculated sitting on the i type of atoms within the spherical shell between distance r and $r + \delta r$ is δn_2. The volume of the spherical cell is $4\pi r^2 \delta r$. Then the radial distribution function of ion pair j-i, taking atom i type as origin, will be the local density of the j type atoms found in that spherical shell, divided by the density of the j type of atoms in the simulation box. The equation of radial distribution

function in this case is

$$g(r) = \frac{1}{n_1} \frac{\frac{\delta n_2}{4\pi r^2 \delta r}}{\left(\frac{n_2}{V}\right)} = \frac{V \times \delta n_2}{4\pi\ r^2\ \delta r\ n_1\ n_2} \tag{2.49}$$

Factor $\frac{1}{n_1}$ appears due to averaging of $g(r)$ for all the i type particle taking as origin. The number of neighbors in each bin is averaged over the entire simulation over all the i-j type of pairs.

Running co-ordination number at distance r, $C(r)$ is defined as the integration of $g(r)$ from distance zero to distance r. Physically it means the total number of neighbors of an atom within a spherical volume of r around it. Mathematical expression of $C(r)$ is,

$$C(r) = \int_0^r 4\pi s^2 g(s) ds \tag{2.50}$$

2.7.3 Angle distribution function

Angle distribution function is the probability distribution of angles between a triplet of atoms, and is useful to map the angular average orientation of the pair of bonds. The equations for angle distribution function between two bonds ij and ik is,

$$g(\theta) = \langle (\sum_i \sum_{j \neq i} \sum_{k \neq j} \delta(\theta - \theta_{ijk}) \rangle \tag{2.51}$$

2.7.4 Mean Square Displacement

Mean square displacement (MSD) is a measure of the average distance square an atom travels with respect to time. The mean square displacement of atoms can easily be computed by its definition,

$$MSD = \langle |\overline{r}_i(t) - \overline{r}_i(0)|^2 \rangle \tag{2.52}$$

in this equation $|\bar{r}_i(t) - \bar{r}_i(0)|$ denotes the vector distance traveled by an atom over a period of time, t. The squared magnitude of this vector is averaged (as indicated by the angle brackets) over all the particles and with respect to several time origins.

The slope of the MSD gives the self-diffusion co-efficient, D. In the three dimensional case the equation reads like,

$$D = \lim_{t' \to \infty} \frac{\langle |r_i(t + t') - r_i(t)|^2 \rangle}{6t'} \tag{2.53}$$

It does not depend on the time origin. From the diffusion coefficient D, using Nernst-Einstein equation ionic *dc*-conductivity (σ) can be measured as,

$$\sigma = \frac{nq^2 D}{k_B T} \tag{2.54}$$

where n= Number density of the mobile atom, k_B= Boltzman Constant, T= temperature, q is the charge carried by the mobile ion.

Again the diffusion coefficient of solid at different temperatures are related by the equation,

$$D = D_0 \, e^{-\frac{E_a}{k_B T}} \tag{2.55}$$

where D_0 is the limiting diffusion coefficient at infinite temperature and E_a is activation energy of the atom for diffusion. Now putting the value of D on the eqn. 2.54, we get the Arrhenius relation,

$$\sigma = \frac{nq^2 D_0 \, e^{\frac{-E_a}{k_B T}}}{k_B T}$$

$$\sigma = \sigma_0 \frac{e^{-E_a/k_B T}}{T}$$

$$\ln(\sigma T) = \ln(\sigma_0) - \frac{E_a}{k_B T} \tag{2.56}$$

where $\sigma_0 = \frac{nq^2 D_0}{k_B}$. When $\ln(\sigma T)$ is plotted against $\frac{1}{T}$, the slope of the plot gives activation energy E_a.

In our study these formulas have been used to analyze the trajectories of atoms and various microscopic properties have been extracted.

Bibliography

[1] N. Metropolis, A. W. Rosenbluth, M. N. Rosenbluth, A. H. Teller, and E. Teller, J. Chem. Phys. **21**, 1087 (1953).

[2] W. Wood and F. Parker, J. Chem. Phys. **27**, 720 (1957).

[3] B. Alder and T. Wainwright, J. Chem. Phys. **27**, 1208 (1957).

[4] A. Rahman, Phys. Rev. **136**, A405 (1964).

[5] B. Berne, P. Pechukas, and G. Harp, J. Chem. Phys. **49**, 3125 (1968).

[6] H. L. Lemberg and F. H. Stillinger, J. Chem. Phys. **62**, 1677 (1975).

[7] D. Wood, Computer simulation of water and aqueous solutions, in *Water: A Comprehensive Treatise*, pages 279–409, Springer, 1979.

[8] D. H. Morse and R. S. Fritz, Oecologia **60**, 190 (1983).

[9] J.-P. Ryckaert and A. Bellemans, Chem. Phys. Lett. **30**, 123 (1975).

[10] J. McCammon and M. Karplus, (1977).

[11] Y. Duan and P. A. Kollman, Science **282**, 740 (1998).

[12] J. Barker, R. Watts, J. K. Lee, T. Schafer, and Y.-T. Lee, J. Chem. Phys. **61**, 3081 (1974).

[13] G. A. Chapela, G. Saville, S. M. Thompson, and J. S. Rowlinson, J. Chem. Soc., Faraday Trans. 2 **73**, 1133 (1977).

[14] D. Frenkel and J. McTague, J. Chem. Phys. **72**, 2801 (1980).

[15] C. Catlow et al., Philosophical Transactions of the Royal Society A: Mathematical, Physical and Engineering Sciences **368**, 3379 (2010).

[16] M. P. Allen and D. J. Tildesley, *Computer simulation of liquids*, Oxford university press, 1989.

[17] D. Frenkel and B. Smit, *Understanding molecular simulation: from algorithms to applications*, Access Online via Elsevier, 2001.

[18] G. J. Martyna, M. E. Tuckerman, D. J. Tobias, and M. L. Klein, Mol. Phys. **87**, 1117 (1996).

[19] M. Parrinello and A. Rahman, J. Appl. Phys. **52**, 7182 (1981).

[20] R. D. Etters and J. Kaelberer, Phys. Rev. A **11**, 1068 (1975).

[21] H. L. Davis, J. Jellinek, and R. S. Berry, J. Chem. Phys. **86**, 6456 (1987).

[22] D. Adams, Mol. Phys. **29**, 307 (1975).

[23] M. P. Tosi, Solid State Phys. **16**, 1 (1964).

[24] D. Adams, Mol. Phys. **28**, 1241 (1974).

[25] J. W. Lewis and K. Singer, J. Chem. Soc., Faraday Trans. 2 **71**, 41 (1975).

[26] L.-V. Woodcock, Chem. Phys. Lett. **10**, 257 (1971).

[27] M. Wolf, J. Walker, and C. Catlow, Solid State Ionics **13**, 33 (1984).

[28] M. Wolf and C. Catlow, J. Phys. C: Solid State Phys. **17**, 6635 (1984).

[29] M. Gillan and M. Dixon, J. Phys. C: Solid State Phys. **13**, 1901 (1980).

[30] Z. Cheng, J. Chang, Z. Jia, and N. Chen, Mol. Simul. **10**, 27 (1993).

[31] R. A. Montani, J. Chem. Phys. **100**, 8381 (1994).

[32] B. Ammundsen and J. Paulsen, Adv. Mater. **13**, 943 (2001).

[33] P. Wilde and C. Catlow, Solid State Ionics **112**, 173 (1998).

[34] P. Vashishta and A. Rahman, Phys. Rev. Lett.;(United States) **40** (1978).

[35] J. R. Ray and P. Vashishta, J. Chem. Phys. **90**, 6580 (1989).

[36] P. Sindzingre and M. Gillan, J. Phys. C: Solid State Phys. **21**, 4017 (1988).

[37] C. Catlow and G. D. Price, Nature **347**, 243 (1990).

Chapter 3

Framework Flexibility of NASICONs: Role of Disorder and Polyhedral Distortions from Monte Carlo Investigation[†]

3.1 Introduction

NASICONs (acronym for Na-SuperIonic CONductors) forms a large family of solids having high thermal and chemical stabilities, with potential technological applications in nuclear waste immobilization[1–3], as refractory materials, low thermal expansion ceramics,[4–15] and as solid electrolytes[16–19], gas sensors[20, 21]. The best studied $NaZr_2P_3O_{12}$ that is prototypical of NASICON solids stabilizing in the rhombohedral $R\bar{3}c$ structure [22],

[†]Publications based on this work: (1)Supriya Roy and P. Padma Kumar, *AIP Conf. Proc.*, **1349**, 113-114 (2011) (2)Supriya Roy and P. Padma Kumar, *J. Mat. Sci.*, **47**, 4946 (2012).

has a three dimensional framework structure of ZrO_6-octahedra sharing corners with PO_4-tetrahedra. The corner sharing of the polyhedra, opposed to edge sharing, makes the NASICON framework (often referred to as the NZP-framework /skeleton) highly fluxional allowing for wide ranges of chemical substitutions [23]. The framework flexibility of NASICONs is responsible for their low thermal expansivity, and makes them one of the most attractive family of materials in the search for better solid electrolytes [19, 22–25]. Bulk thermal expansion of these material is influenced by the interstitial alkali ions. Insertion of larger cation lowers thermal expansions. Most of the NZP solids show anisotropic thermal expansions with α_a negative and α_c positive. This anisotropy is the main cause of the low-thermal expansion of these materials.

Several experimental reports are available in the literature on the low-anisotropic nature of thermal expansivity of NZP skeleton [26–29]. Alamo and coworkers have proposed a structural model [23, 30, 31], which provides a qualitative explanation of the low-anisotropic changes in the lattice parameters in terms of coupled rotations of the structural polyhedra. However certain underlying assumptions of the structural model, such as the distortions of the polyhedra and the extent of polyhedral rotations are not critically evaluated against experimental results. Further it would be of interest to examine if these polyhedral disorder are static, frozen-in or a dynamical one. We present results based on Monte Carlo investigation of the structural changes in the NZP-skeleton upon substitution of alkali ions of varying sizes. The ability of the interatomic potential in reproducing the gross experimental results on NZP solids, when loaded with larger alkali ions, and over a wide range of temperatures, is critically examined comparing with available experimental results. The extent of validity of the rigid polyhedra based structural model of Alamo and coworkers [23, 30, 31] in explaining the anisotropic variations in lattice parameters of these solids is investigated. The nature of the polyhedral disorder in these systems is also examined in the light of the present simulation results.

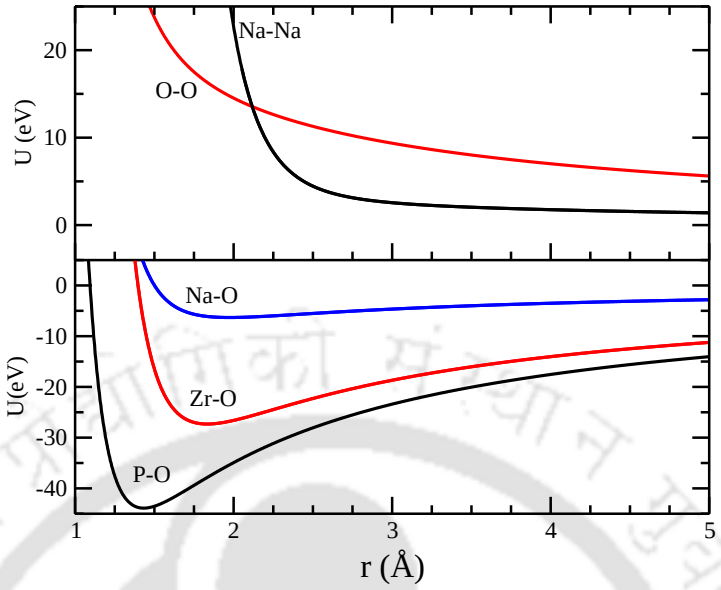

FIGURE 3.1: Plots of the interaction potential between select species, Na-Na, O-O (top panel), Na-O, Zr-O and P-O (lower panel),are given over a range of 1 - 5 *Å*.

3.2 Method

Isobaric-isothermal (NPT) ensemble Monte Carlo simulation (NPT-MC) is employed in the present study of structural changes in $MZr_2P_3O_{12}$. The NPT-MC method employed [32] allows changes in the shape and size of the simulation box in contrast to canonical (NVT) ensemble Monte Carlo method such that uniform-hydrostatic pressure is maintained in the system. This method is well suited in the studies of structural transformations of solids. Following earlier computer simulation investigations on $Na_{1+x}Zr_2Si_xP_{3-x}O_{12}$ by Padma Kumar and Yashonath [33, 34] the present study employs inter-atomic potentials of the form,

$$U(r_{ij}) = \frac{q_i q_j}{r_{ij}} + \frac{A_{ij}(\sigma_i + \sigma_j)^{n_{ij}}}{r_{ij}^{n_{ij}}} - \frac{C_{ij}}{r_{ij}^6} \tag{3.1}$$

where q_i and σ_i are respectively the effective charge and ionic radius of ith ion. r_{ij} is the inter-atomic distance, A_{ij} and C_{ij} are the overlap-repulsive energy and dispersion terms

TABLE 3.1: Interaction potential parameters between, species X and oxygens, where $X = M, Zr, P$ or O and $M = Li^+, Na^+, K^+, Rb^+$ and Cs^+.

Species(X)	$q_x(\mid e \mid)$	$\sigma_x(\AA)$	$A_{XO}(eV)$	$C_{XO}(eV.\AA^6)$	$n_{XO}{}^*$
M	0.702	(0.9 – 1.81)	0.1716	0.0	9
Zr	2.808	0.86	1.2126	11.917	9
P	3.510	0.31	3.6158	9.279	9
O	−1.404	1.21	0.3252	47.999	7

$A_{M-M} = 5eV$ and $n_{M-M} = 11$. All the other parameters not listed above are kept zero.

respectively between ion pairs i and j. The ionic radii employed in the present study are taken from Huheey [35]. The parameters employed are as listed in Table4.1. The potential between important pairs are plotted in figure 4.7. A remarkable feature of this potential function, originally proposed by Vashishta and Rahman [36] for AgI, is the softer overlap repulsion ($1/r^n$ with n < 12) compared to the more popular Born-Mayer and Lennard-Jones forms. The softness further depends on the nature of the charge of the ions, as expected between two positive charge the repulsion is very strong as n=11, between positive and negative charge it is softer n=9 and the repulsion is further soft between negative charges with n=7. The partial charges on ions accounts for the partial covalent nature of the interatomic interactions, and were optimized along with A_{ij} and C_{ij} to reproduce the X-ray structure and ionic conductivity of the high conducting, rhomohedral-phase of $Na_3Zr_2Si_2PO_{12}$ at 600 K [33]. Though less obvious, short range repulsion between oxygen ions plays a crucial role, along with the Zr-O and P-O interactions, in maintaining the polyhedral structure intact. The short range repulsion between the sodium ions and the Na-O interactions influence Na^+ mobility in $Na_3Zr_2Si_2PO_{12}$.

NPT ensemble MC (NPT-MC) simulations of $MZr_2P_3O_{12}$ systems, where M is Li^+, Na^+, K^+, Rb^+ or Cs^+, are carried out over the temperature range of 300-900 K, all at one atmospheric pressure. The choice of NPT-MC over NPT-molecular dynamics (NPT-MD) made here, is in view of the better converge of thermodynamic averages in MC for the same computing time [37], and the ease of implementation. The simulations of all $MZr_2P_3O_{12}$ systems at 600 K are started from the - rhombohedral X-ray structure of $NaZr_2P_3O_{12}$, with unit cell parameters $a = b = 8.80\AA$ and $c = 22.83\AA$, $\alpha = \beta = 90°$and γ =120° [22]. It may be noted that there

are three prominent alkali ion sites in the rhombohedral NASICON structure. These sites shall be referred to as M(1), M(2) and mid-M, which correspond to 6b, 18e, 36f sites of the space group $R\bar{3}c$, respectively [19]. The simulations are started with all alkali ions placed at the 6b sites (shall be referred to as M(1) sites henceforth). The simulation includes a total of 972 ions, equivalent to $3 \times 3 \times 1$ rhomohedral unit cells, each containing 6 formula units of $MZr_2P_3O_{12}$. Simulations at temperatures other than 600 K are started from the final configurations (coordinates of the atoms and simulation cell parameters) for the closest temperature available. Typically, 40000 MC steps were dedicated for equilibration and another 40000 MC steps for averaging. By an MC step, we mean, attempts to move all the ions in the system starting from a randomly picked ion and proceeding serially over all the remaining ones [32]. Attempts to change the shape and size of the simulation supercell are performed once in every four MC moves. The atomic configurations are written out after every 8 MC steps for detailed structural analysis. Simulation using $5 \times 5 \times 2$ unit cells were performed to confirm the adequacy of the system size employed here.

The Statistical error estimates for lattice parameters from the present simulation are estimated by the method of block averages [32]. The data from the MC sampling is divided into n_b blocks of size τ_b. The statistical inefficiency of the sampling is then calculated as,

$$s = \lim_{\tau_b \to \infty} \frac{\tau_b \times \sigma^2(\langle a \rangle_b)}{\sigma^2(a)} \tag{3.2}$$

where $\langle a \rangle_b = \frac{1}{\tau_b} \sum_{\tau=1}^{\tau_b} a(\tau)$ is the average of the quantity, a, over a block, $\sigma^2(\langle a \rangle)_b)$ represent the variance across blocks of size b, and $\sigma^2(\langle a \rangle)$ refers to the variance over the entire data set. The saturation value of S, $S_{plateau}$,when plotted against $\tau_b^{-1/2}$ gives the minimum block size beyond which data are uncorrelated. Finally the statistical errors are estimated as

$$\Delta = \left[\frac{S_{plateau}}{\tau_b n_b} \right]^{1/2} \times \sigma(a) \tag{3.3}$$

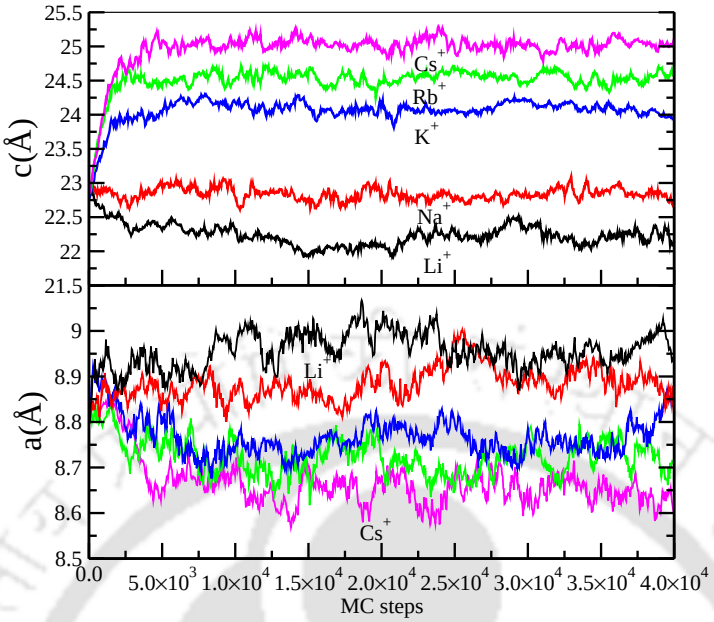

FIGURE 3.2: The evaluation of lattice parameters c and a over with MC steps at 600 K for different alkali ions with variable sizes Li^+, Na^+, K^+, Rb^+ and Cs^+. The starting structures of all systems are chosen as that of the $NaZr_2P_3O_{12}$ at 600 K.

3.3 Result and Discussion

Figure 3.2 shows the evolution of lattice parameters c, a with MC steps for different alkali ion containing NZP skeletons during equilibration at 600 K. It can be seen that for larger cation size (K^+, Rb^+, and Cs^+) c increases gradually from their starting value (chosen as that of the $NaZr_2P_3O_{12}$) for a few thousand initial MC steps and reaches a plateau, while for the smaller cation Li^+ containing system the lattice parameters decreases initially (figure. 3.2a). Value of c, a remains nearly constant for the system $NaZr_2P_3O_{12}$ as expected. The pattern of changes in a is of opposite nature, though much less pronounced compared to that of c. Beyond the transient region of about 4000 MC steps variation is that of fluctuations about the mean value characteristic of systems in equilibrium.

The average cell parameters of the $MZr_2P_3O_{12}$ systems, where M is Li^+, Na^+, K^+, Rb^+ or Cs^+, at 600 K is shown as a function of the alkali ion size in figure 3.3. In figure 3.4a statistical inefficiency S plotted for c parameter against the square root of block sizes for the

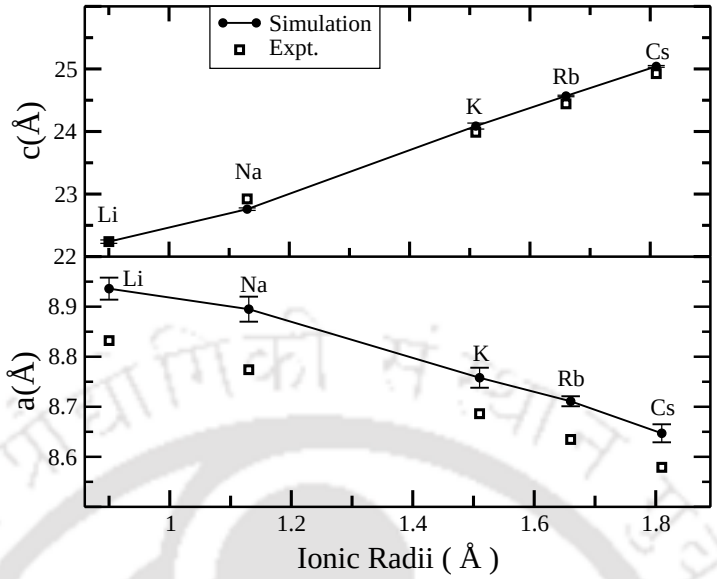

FIGURE 3.3: Variation of average lattice parameters c and a over 40,000 MC steps with the size of the alkali ion incorporated in NASICON framework at 600K.

different systems. It shows that K^+ containing system shows slower convergence compared to other systems. To estimate the length of correlated data, S which measures the number of MC steps containing completely new information to the average is generated, S is plotted against the inverse of block size, τ_b, in figure 3.4b. The value of $S_{plateau}$ (in Eqn.3.2) is obtained from the intersecting point of the extrapolated fitted line at $\tau_b = 0$ in figure 3.4b. Values of $S_{plateau}$ obtained for all the systems $Li^+, Na^+, K^+, Rb^+ or\ Cs^+$ systems are approximately 459, 246, 739, 175, 236 respectively.

Then the error bars estimated employing the block averages (Eqn.3.3). The error in the average cell angles obtained (not shown) are within 0.5% of the rhombohedral values, and the difference in a and b are within 0.2%, in all cases, confirming the rhombohedral symmetry of the system. A anisotropic variation in lattice parameters, where a increase in the c-parameter and a decrease in the a-parameter with the size of the alkali ion is observed. This is in good agreement with previous experimental results (the experimental data shown are extracted from figure 3.2 of reference [38]).

The effect of the anisotropic changes in lattice parameters on the distribution of M(1) sites

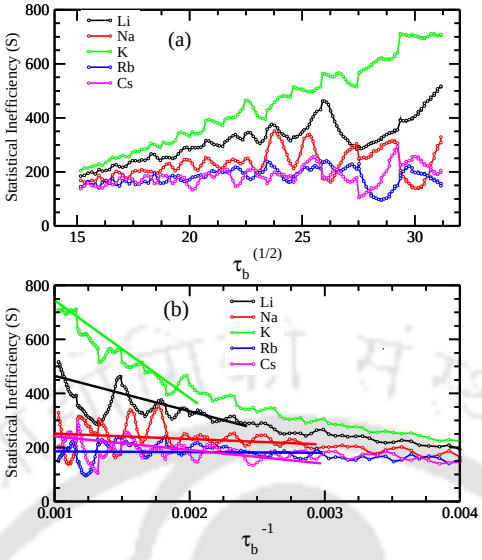

FIGURE 3.4: Plot of statistical inefficiency for c parameter from MC simulation against (a) the square root of block sizes (b) inverse of block sizes for the $MZr_2P_3O_{12}$ (where Li^+, Na^+, K^+, Rb^+ or Cs^+) systems at 600K.

is examined using the radial distribution function (rdf) between the alkali ions calculated over the 40000 MC steps at 600 K (shown in figure 3.5).

TABLE 3.2: Select interatomic distances in $\AA$, for pairs M-O, Zr-O and P-O from NPT-MC simulations at 600 K. The values in parenthesis are experimental data.

M	$\sigma(\AA)$	*M-O*	*Zr-O*	*P-O*	*Ref*
Li^+	0.90	2.22	2.06	1.52	
		(2.49)	(2.06)	(1.52)	[39]
Na^+	1.13	2.57	2.07	1.52	
		(2.54)	-	(1.52)	[22]
K^+	1.51	2.85	2.07	1.52	
Rb^+	1.66	2.96	2.08	1.52	
Cs^+	1.81	3.05	2.08	1.52	
		(2.89)	(2.08)	(1.53)	[40]

The prominent, first peak in the rdfs appear at around 6.2 $\AA$ which correspond to the separation between the neighbouring 6b sites (M(1)-M(1) distance). The six neighbouring M(1) sites (of a given M(1) site) are on two different a-b planes, $c/6$ above and $c/6$ below the plane containing the reference M(1) site. An M(1) site has six of its second neighbouring

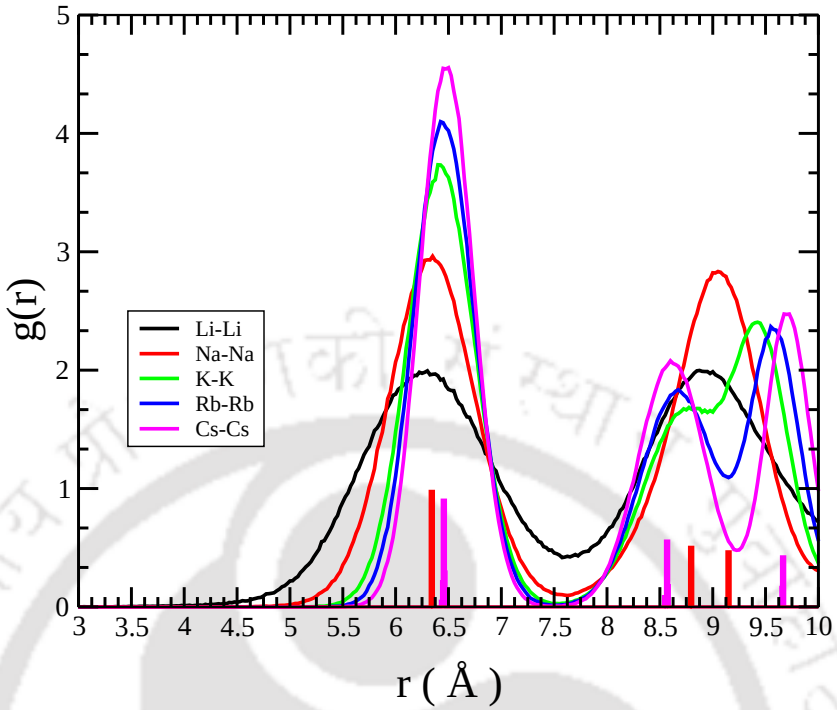

FIGURE 3.5: The radial distribution functions between the alkali ions from NPT-MC simulation at 600 K. The bars indicate the M(1)-M(1) distances for Na^+ (black) and Cs^+ (blue) substituted systems calculated from their respective X-ray structure [22, 40].

M(1) sites at a distance equal to lattice parameter a on the same a-b plane, while another six third neighbours, are arranged on two a-b planes, $c/3$ above and $c/3$ below them. For the Na^+ system, for instance, these sites (2^{nd} and 3^{rd} neighbours) occur at close distances of 8.8 $\AA$ and 9.13 $\AA$ at 600 K, and fall within the broad second peak of the rdf. However, for larger alkali ion containing systems, the distance to the in-plane 2^{nd} neighbors decrease while the distance to off-plane 3rd neighbors increases due to the anisotropic expansion of the unit cell.

This results in the splitting of the second peak of the M-M rdfs figure 3.5. The agreement in the positions of the peaks in the M-M rdfs for the simulated Na and Cs-systems to the M(1) - M(1) distances from their respective X-ray structures [22, 40], shown by vertical lines in figure 3.5, reflects this aspect. It may be noted in passing that at higher temperatures (above 600 K) Na^+ and larger alkali ions remain at the M(1) sites. The Li^+ -ions, however, starts hoping between the M(1) and M(2) sites above 600 K, which is expected as $LiZr_2P_3O_{12}$ exhibits fast

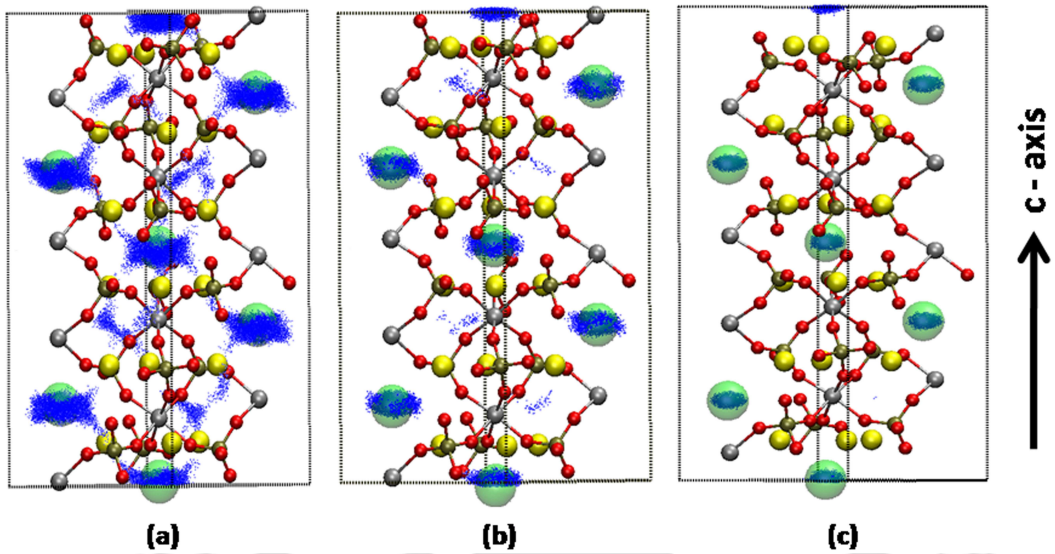

FIGURE 3.6: The alkali ion positions from 40000 MC configurations (blue dots) folded back in to a single unit cell for,(a):Li^+, (b) Na^+, (c)Cs^+ substituted systems (not to scale). The M(1) and M(2) sites of the alkali ions are shown respectively by light-green and yellow balls. A single framework configuration in ball and stick representation,where Zr (silver), P (mauve) and O (red), is also shown. The scattered alkali ion positions appearing away from the M(1) sites shown are largely the population around the M(1) sites of the neighbouring unit cells.

ion conduction around 600 K [39, 41]. A demonstration of the alkali ion localization at M(1) sites is provided in figure 3.6, where the coordinates of alkali ions, Li^+, Na^+, Cs^+ across the 40000 MC configurations, folded back in to a single unit cell at 600 K is shown amidst the framework structure and the M(1) and M(2) sites of the respective system.

The alkali ions (blue dots) evidently populate the M(1) sites (light green balls) at 600 K, leaving vacant the M(2) sites (yellow balls). The extent of the alkali ion distribution around M(1) sites provides a measure of the thermal amplitudes of the alkali ions which are larger for smaller alkali ions. Information related to structural parameters of the building polyhedra and their connectivity are obtained from the analysis of the MC configurations generated. Table 3.2 lists the bond-lengths between select atomic pairs, Zr-O, P-O, M-O, obtained from the respective rdfs at 600 K. Zr and P ions show sharp coordination numbers of six and four with oxygens respectively, as expected of ZrO_6-octahedra and PO_4- tetrahedra. Alkali ions, however, exhibit relatively weak six coordination with oxygens due to their larger thermal

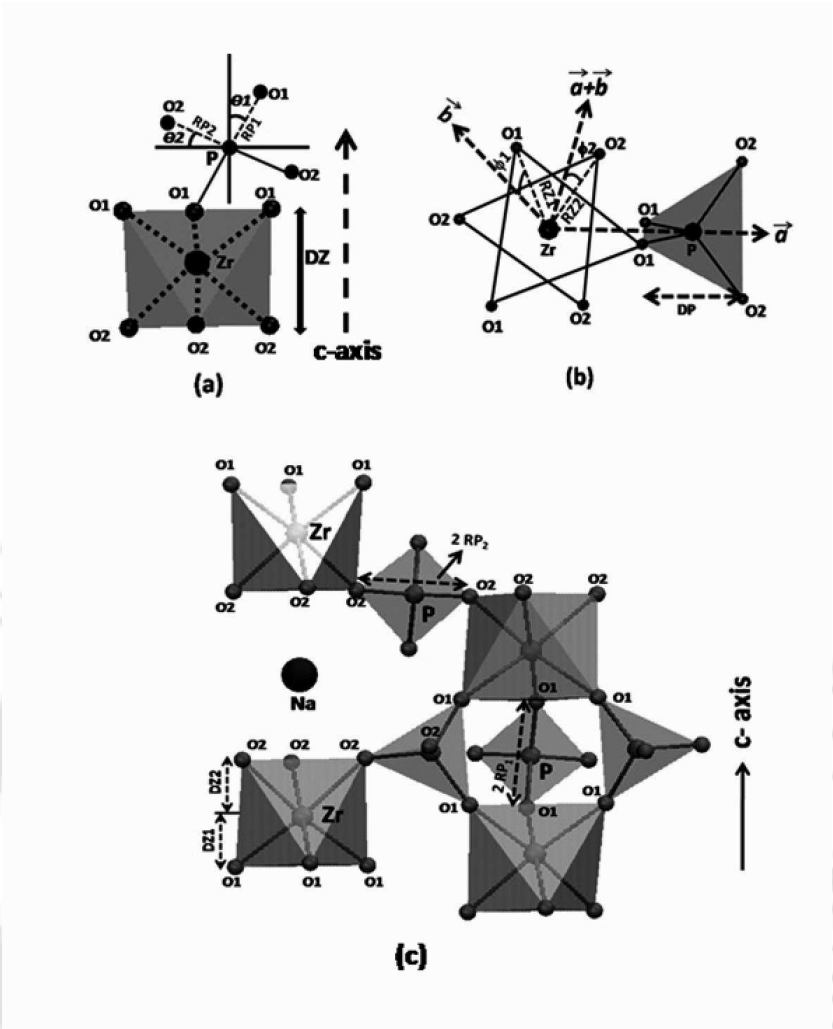

FIGURE 3.7: The illustration of angles and distances employed in the structural analysis (see text for details). An M(1) site (marked Na),and the lateral connectivity of an $M(1)O_6$ octahedron to a lantern unit consisting of two ZrO_6 octahedra pillared by three PO_4 tetrahedra are shown in (c).

amplitudes. It may be noted from Table 3.2 that the Zr-O and P-O bond lengths do not change appreciably with the size of the alkali ion incorporated in the framework. Significant increase in the average M-O distances are observed, as expected. The agreement in Li-O distance between simulation results and experimental data [41] are due to the fact that the Li^+ ions are found located off-centered in the Li-O octahedral hole in simulations. Thus this value does not serve a good measure of the octahedral hole in the case of the Li-system. The value of 2.22 *Å* from simulation appears more reasonable in the light of the neutron diffraction results [42]. Other interatomic distances are in good agreement with previous X-ray studies [19, 40].

The interest is, thus, how the $[Zr_2P_3O_{12}]^-$ framework accommodates the increase in the

M-O_6 octahedron without appreciable change in the covalent bond-lengths in the system. The

TABLE 3.3: Rotational angles of the polyhedra (in degrees) for the various alkali ions substituted NASICON framework from NPT-MC simulations at 600K. The values in parenthesis are experimental data. $\theta 1$ (SM) refers to values predicted by Alamo[31] based on the structural model.

M	$\phi 1$	$\phi 2$	$\theta 1$	$\theta 1(SM)$	$\theta 2$	Ref
Li^+	6.1	7.4	8.0	3	6.9	-
Na^+	6.9	7.6	9.2	6	9.5	
	(8.9)	(6.2)	(11.7)		(8.4)	[22]
K^+	10.4	8.2	13.9	15	17.1	
	(11.2)	(7.1)	(15.1)		(14.0)	[30]
Rb^+	11.9	8.3	15.7	–	19.9	-
Cs^+	13.6	8.6	17.7		22.7	
	(11.59)	(7.25)	(14.80)	24	(15.41)	[40]

anomalous changes in the lattice parameters were explained by Alamo and co-workers based on a mechanism involving coupled rotations of the polyhedral [23, 30, 31]. The pressure exerted on the two neighbouring ZrO_6 octahedra by the larger cation in the M(1) sites results in an in-equivalent rotation of the two triangular faces of the octahedra (parallel to the a-b plane) about its 3-fold axis parallel to the c-axis. As the Zr-O and P-O bonds are practically rigid the PO_4 tetrahedra connected to the two neighbouring ZrO_6 octahedra are bound to rotate about their 2-fold axis parallel to the a-b plane. By projecting distances measured along the Zr-O and P-O bonds on to the a-b plane and c-axes of the rhombohedral cell, Alamo and co-workers proposed the following exact equations connecting the rotational angles of the polyhedra and the lattice parameters [30, 31].

$$a = 2 \times \left[\left(RZ1 \cos\phi 1 + RZ2 \ \sin(\phi 2 + \frac{\pi}{6})\right) + DP\right] \tag{3.4}$$

$$b = 6 \times [(RP1 \cos\theta 1 + RP2 \ \sin\theta 2)) + DZ] \tag{3.5}$$

Where distances RZ1, RZ2, RP1, RP2, DZ, DP and the angles $\phi 1$, $\phi 2$, $\theta 1$ and $\theta 2$ are illustrated in figure 3.7. RZ1 and RZ2 measures the circum radii of the triangular faces of the ZrO_6 octahedra parallel to the a-b-plane, formed respectively by O1 and O2 -oxygens.

The O2-oxygens are those forming the triangular basal planes of the two ZrO_6 around an

TABLE 3.4: The internal measures of pertaining to the PO_4 tetrahedra and ZrO_6 octahedra,from NPT-MC simulation at 600 K. The values in parenthesis are calculated from respective X-ray structure.

M	*RP*1	*RP*2	*DP*	*RZ*1	*RZ*2	*DZ*	Ref
Li^+	1.21	1.23	1.80	1.65	1.72	2.37	-
Na^+	1.22	1.23	1.79	1.64	1.72	2.39	
	(1.29)	(1.26)	(1.79)	(1.68)	(1.6)	(2.36)	[22]
K^+	1.24	1.24	1.76	1.60	1.72	2.44	-
Rb^+	1.24	1.24	1.75	1.59	1.72	2.48	-
Cs^+	1.25	1.24	1.74	1.57	1.73	2.51	
	(1.30)	(1.24)	(1.69)	(1.66)	(1.6)	(2.55)	[40]

M(1) site of the alkali ions (thus forming the $M(1)O_6$ octahedra), and the O1-oxygens forms the basal planes of two neighbouring ZrO_6 pillared by the edges of three PO_4 tetrahedra when viewed along the *c*-axis. RP1 and RP2 are respectively half the O1-O1 and O2-O2 distances of the PO_4 tetrahedra. DZ measures the height of the ZrO_6 octahedra along the *c*-axis, and *DP* is the dimension of the tetrahedra measured along the 2-fold axis parallel to the a-b-plane. $\phi 1$ measures the rotation angle of the triangular face formed by O1-oxygens of the octahedra with respect to the b-axis, and $\phi 2$ is the angle the O2-oxygens makes with the vector, *a*+*b*, as shown in figure 3.7. $\theta 1$ is the tilt angle O1-O1 edge of PO_4 makes with the c-axis, and $\theta 2$ is the angle O2-O2 edge of PO_4 makes with the *a*-*b* plane.

The rotational angles of the polyhedra calculated from the present NPT-MC simulation at 600 K is listed table 3.3. The rotational angles calculated by us from the X-ray structures [22, 40] for Na and Cs-systems,as well as those reported for K^+ substituted system [30] are also given for comparison. It can be seen that the rotational angles of the polyhedra $\phi 1$ and $\phi 2$ of the octahedra, and $\theta 1$ and $\theta 2$ of the tetrahedra increase with the size of alkali ion. These increased rotations of the octahedra about its three-fold axis and the tilt of the tetrahedra about its two-fold axis are in agreement with the experimental results. Based on the structural model, Alamo [31] has predicted the tilt angle, $\theta 1$,for Li, Na, K, Cs -systems by fitting to the respective experimental lattice parameters (also listed in table 3.3). A 'rigid' polyhedral model with parameters, RP1, RP2, DP, RZ1, RZ2 and DZ, taken from K^+ substituted system is

presumably employed in this analysis [27]. Over all, simulation results are in better agreement with experimental results than those predicted by the structural model [30].

It may be noted that Alamo and coworkers estimates of polyhedral rotations are based on 'rigid' polyhedral model, subject only to torsional modifications [30]. We have examined the extent to which this rigid polyhedral model holds for these systems. For this purpose, the detailed structural parameters of the polyhedral units, averaged over all the polyhedra and over the 40000 MC steps,are computed (see table 3.4).

The distances RP1 and DP show changes of 0.04 $\AA$ and 0.06 $\AA$, respectively, between the end members Li^+ and Cs^+- substituted systems; while RP2 remain almost a constant across the series. From Eq.3.4, the decrease in DP contributes to about 0.12 $\AA$ decrease in the *a*-parameter, accounts for about $1/3^{rd}$ of the change observed between the Li^+ and Cs^+ substituted systems. The internal measures of the ZrO_6 octahedra, RZ1 and DZ changes through 0.08 $\AA$ and 0.14 $\AA$, respectively, while RZ2 remain nearly constant across the series. The elongation of the octahedra thus contribute to about 0.84 $\AA$ of change in *c*-parameter between the Li and Cs -systems, again accounts for nearly $1/3^{rd}$ of the total change observed. The internal measures of the polyhedra computed from MC are compared with data extracted from X-ray structures for Na^+ and Cs^+ substituted systems [22, 40] (given in parenthesis in table 3.4). The agreement is within 4% in the case of PO_4 tetrahedra, and within 8% for ZrO_6 octahedra. These differences are responsible for the relative larger values of *a*-parameters observed in simulations figure 3.3. Turning to the structural model as noted earlier, Alamo′s estimates of rotational angles are on the higher side for larger ions, though the equation 3.4 provided by the structure model are exact. This owes to the fact that the internal measures of the polyhedra, particularly DP and DZ, are kept constant throughout series. Thus the present simulation results as well as experimental observations do not support the rigid polyhedra model, and emphasis the need to account for the polyhedral distortions.

It is worth examining these polyhedral deformations a little more closely, and their connection to the size of the alkali ion inserted. The larger cations exert a vertical (along the z-axis) stress on the two neighbouring ZrO_6 octahedra resulting the expansion of $M(1)O_6$

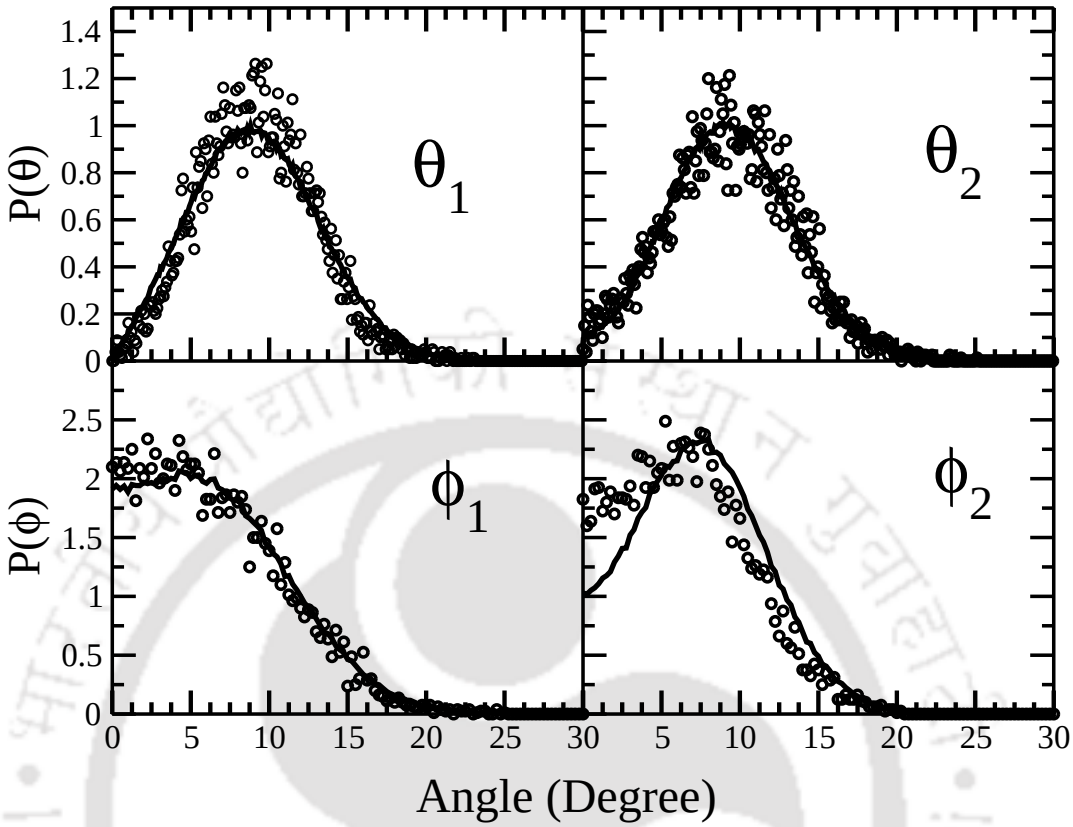

FIGURE 3.8: Distribution of rotation angles of the PO_4 tetrahedra and ZrO_6 octahedra, $\theta 1$, $\theta 2$, $\phi 1$and $\phi 2$, at 600 K for $NaZr_2P_3O_{12}$. Continuous lines are averaged over all the polyhedral units, circles are those for a single polyhedron,arbitrarily chosen all averaged over 40000 MC configurations.

octahedra along the z-axis. This stress gets transferred across to the lantern units, consisting of two octahedra pillared by three tetrahedra (figure 3.7(c)). Since the height of the $M(1)O_6$ (along the z-axis) equals half the height of the lantern units its expands correspondingly. Thus the polyhedra show an overall expansion in the z-direction, and explains the increase in *DZ* and *RP*1 (figure 3.7(a) and (c)). On the other hand some of the polyhedral measures on the $a-b$ plane, such as *DP* and *RZ*1 decreases, while others *RP*2 and *RZ*2 remain constant with the size of the alkali ion (figure 3.7(b) and (c)). This behavior owes to the fact that the stress due to the larger alkali ions is oriented along the *c*-axis, and is consistent with the small reduction in a-parameter. Further, the increase in *DZ* owes entirely to *DZ*1 (not listed in table 3.4), which is the distance from Zr to the O1-triangular face of the octahedra, that is away from the

alkali ion site. (Note that *RZ*1 and *DZ*1 are projections of Zr-O bond on to the *a-b* plane and the c-axis respectively, and Zr-O bond lengths remain nearly a constant. Thus the reduction in *RZ*1 causes an increase in *DZ*1.) Similarly the increase in *RP*1 accounts for the reduction in *DP*1. Thus the deformations of the polyhedra are more intricate than an expansion along the z-axis and a contraction on the *a-b* plane.

Colomban et al. examining the phase transition in $Na_3Zr_2Si_2PO_{12}$ have proposed that the nature of the polyhedral rotation can have a profound influence on the thermodynamics of these systems [43]. Shown in figure 3.8, the distribution functions (un-normalized) of the rotational angles of the PO_4 tetrahedra, $\theta 1$ and $\theta 2$, and those of the ZrO_6 octahedra, $\phi 1$ and $\phi 2$, of $NaZr_2Si_2PO_{12}$ at 600 K are shown. The distribution function for each of these angles are computed in two ways one, averaged over all the polyhedral units and over all MC configurations (shown as continuous lines); two, for an arbitrary chosen polyhedra over all MC configurations (shown by circles). It is noted that the distribution functions averaged over all the polyhedral units compares well with the corresponding distribution computed for an arbitrarily chosen polyhedron. This demonstrates that each polyhedron undergoes rotations over the entire range of angles, suggesting the dynamical nature of polyhedral rotations in NASICONs. It shall be noted in passing that molecular dynamics approach would be better suited for a more detailed investigation of this dynamical polyhedral rotations.

Previous experimental studies have shown that the thermal expansion of NASICON framework is significantly influenced by the interstitial ion as well as framework compositions [44–50] a very useful property in the tailor making of low thermal expansion solids. In figure 3.9 the variation of lattice parameters with temperature for the different alkali ion substituted NASICONs is shown over the range of 300-900 K together with data extracted from previous experimental work [38]. Note that for Li and Cs-systems data are shown over restricted ranges. For the Li-system simulations are not performed below 500 K, as the system is known to undergo monoclinic distortion below 443 K. The Cs-system on the other hand is found to be unstable,and undergoes a structural transformation at 900 K in our simulations; hence omitted from the results. No further analysis of this transformation is carried out. We are not aware of

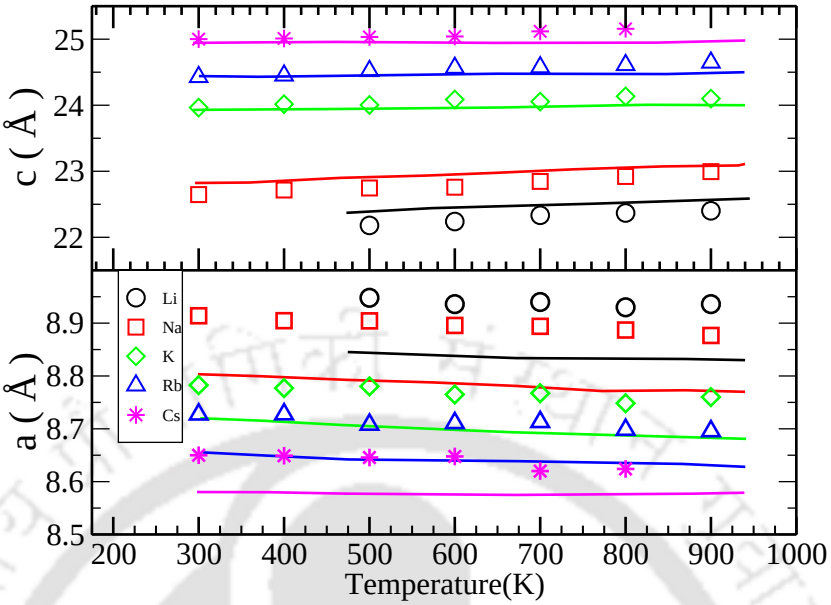

FIGURE 3.9: The variation of c and a parameters with temperature for the alkali ion incorporated NASICONs,from NPT-MC simulations. Lines are experimental data extracted from the figure 3 of reference 33. Symbols are simulation results.

any experimental observation of a transformation in the $CsZr_2P_3O_{12}$ at 900 K; the observation,rather suggest the limit the interatomic potentials can faithfully emulate the system. The *c*-parameter increases with the temperature, while a smaller negative change in *a*-parameter is observed with temperature across the series. The quantitative agreement with experimental results in the *c*-parameter variation is excellent across the series. The absolute values of a-parameters from simulation show typical deviations of about 1% from the corresponding experimental values, across the series, making the agreement appears largely qualitative in the expanded scale of figure 3.9.

Following earlier experimental studies the variation of c-parameter is plotted against a for all compositions ($M = Li^+, Na^+, K^+, Rb^+$ and Cs^+) over the range of 300-900 K. The thermal effects being small relative to the size of the alkali ion incorporated, the data divides into five distinct clusters (shown encircled in figure 3.10), each corresponding to a particular alkali ion and contains data for the entire temperature range. The fact that all data points, irrespective of the temperature, fall nearly to the same universal curve confirms that the dominant mechanism

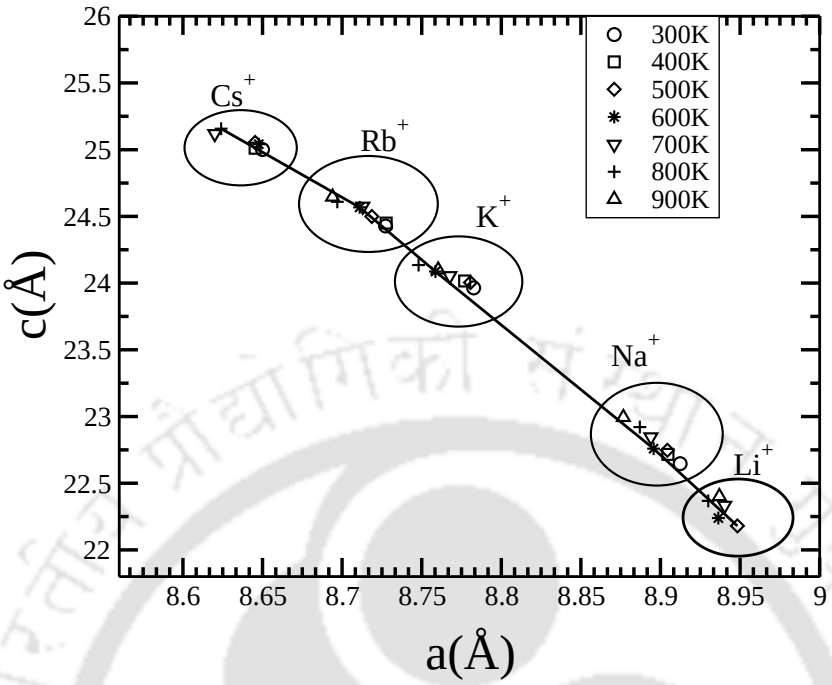

FIGURE 3.10: Variation of lattice parameters,*c* versus *a*,over the temperature range of 300-900 K for $MZr_2P_3O_{12}$, where $M = Li^+, Na^+, K^+, Rb^+$and Cs^+. The solid line is only to guide the eye.

of anisotropic thermal expansion of these systems also involve coupled polyhedral rotations. This suggests that the larger thermal ellipsoid of the alkali ion due to increase in temperature mimic an increase in the size of the ion itself.

3.4 Conclusion

Monte Carlo simulation allowing for changes in the shape and size of the system is performed on NASICON solids $MZr_2P_3O_{12}$incorporating different alkali ions, $M = Li^+, Na^+, K^+, Rb^+$ and Cs^+. The *c*-parameter of the rhombohedral unit cell is found to increase with the size of the alkali ion, while the *a*-parameter found decreasing in agreement with previous experimental results. The alkali ions are found localized at the M(1) sites (6b sites of $R\bar{3}c$) over the entire range of temperatures explored (300 - 900 K), except Li^+ which was found to populate the Na(2) sites (18e sites of $R\bar{3}c$), partially, at temperatures above 600 K. The changes in the

Zr-O and P-O bond lengths across the series is found marginal, however, significant changes in alkali ion oxygen (M-O) distances are observed.

The extent of the coupled rotations of PO_4 tetrahedra and ZrO_6 octahedra as well as the distortions of these polyhedra for different alkali ion containing NASICON framework are in agreement with X-ray structure. The present simulation results suggest that while dominant mechanism of anisotropic variation of lattice parameters involve coupled rotations of the polyhedra, as proposed by Alamo and co-workers, the contribution from polyhedral distortions are also significant. The distortions of the structural polyhedra are estimated to contribute about one-third of the cell parameter variations for the NASICON solids examined here. The anisotropic thermal expansion of $MZr_2P_3O_{12}$-systems follows the same qualitative pattern observed with the size of the alkali ion at a given temperature. The universal behavior of the *c*- versus *a*-parameter variation suggests that the anisotropic thermal expansion involves the same mechanism that allows insertion of larger alkali ion in the NZP-skeleton. Our results suggest that these polyhedral rotations are dynamic in nature.

Bibliography

[1] B. Scheetz, D. Agrawal, E. Breval, and R. Roy, Waste Management **14**, 489 (1994).

[2] C. Hashimoto and S. Nakayama, J. Nucl. Mater. (2013).

[3] R. Chourasia, A. Bohre, R. D. Ambastha, O. Shrivastava, and P. Wattal, J. Mater. Sci. **45**, 533 (2010).

[4] J. Evans, T. Mary, and A. Sleight, J. Solid State Chem. **137**, 148 (1998).

[5] J. O. Evans, J. Chem. Soc., Dalton Trans. , 3317 (1999).

[6] G. Barrera, J. Bruno, T. Barron, and N. Allan, J. Phys. Cond. Matter **17**, R217 (2005).

[7] M. G. Tucker et al., Phys. Rev. Lett. **95**, 255501 (2005).

[8] R. Mittal and S. Chaplot, Phys. Rev. B **60**, 7234 (1999).

[9] G. Buvaneswari, K. Govindan Kutty, and U. Varadaraju, Mater. Res. Bull. **39**, 475 (2004).

[10] R. Roy, D. K. Agrawal, and H. A. McKinstry, Annu. Rev. Mater. Sci. **19**, 59 (1989).

[11] D. Woodcock and P. Lightfoot, J. Mater. Chem. **9**, 2907 (1999).

[12] S. Taniguchi and M. Aniya, A theoretical model for the relationship between thermal expansion and ionic conduction, in *IOP Conference Series: Materials Science and Engineering*, volume 18, page 132016, IOP Publishing, 2011.

[13] N. Anantharamulu et al., J. Mater. Sci. **46**, 2821 (2011).

[14] K. G. Kutty, R. Asuvathraman, and R. Sridharan, J. Mater. Sci. **33**, 4007 (1998).

[15] G. Rambabu et al., J. Mater. Sci. **42**, 3613 (2007).

[16] M. Barré et al., J. Phys. Cond. Matter **21**, 175404 (2009).

[17] J. W. Fergus, Solid State Ionics **227**, 102 (2012).

[18] K. Kreuer and U. Warhus, Mater. Res. Bull. **21**, 357 (1986).

[19] J.-P. Boilot, G. Collin, and P. Colomban, J. Solid State Chem. **73**, 160 (1988).

[20] H. Aono, Y. Sadaoka, L. Montanaro, E. Bartolomeo, and E. Traversa, J. Am. Ceram. Soc. **85**, 585 (2002).

[21] K. Frank, H. Kohler, and U. Guth, Ionics **14**, 363 (2008).

[22] H.-P. Hong, Mater. Res. Bull. **11**, 173 (1976).

[23] J. Alamo and R. Roy, J. Mater. Sci. **21**, 444 (1986).

[24] M. Barj, H. Perthuis, and P. Colomban, Solid State Ionics **9**, 845 (1983).

[25] W. Baur, J. Dygas, D. Whitmore, and J. Faber, Solid State Ionics **18**, 935 (1986).

[26] A. Orlova et al., Crystallogr. Rep **54**, 431 (2009).

[27] T. Ota, P. Jin, and I. Yamai, J. Mater. Sci. **24**, 4239 (1989).

[28] J. F. Cloer, D. K. Agrawal, and H. A. McKinstry, J. Mater. Sci. letters **7**, 422 (1988).

[29] A. Sleight, Endeavour **19**, 64 (1995).

[30] G. E. Lenain, H. A. McKinstry, J. Alamo, and D. Agrawal, J. Mater. Sci. **22**, 17 (1987).

[31] J. Alamo, Solid State Ionics **63**, 547 (1993).

[32] M. P. Allen and D. J. Tildesley, *Computer simulation of liquids*, Oxford university press, 1989.

[33] P. P. Kumar and S. Yashonath, J. Am. Chem. Soc. **124**, 3828 (2002).

[34] P. P. Kumar and S. Yashonath, J. Phys. Chem. B **106**, 7081 (2002).

[35] J. E. Huheey, E. A. Keiter, R. L. Keiter, and O. K. Medhi, *Inorganic chemistry: principles of structure and reactivity*, Harper & Row New York, 1983.

[36] P. Vashishta and A. Rahman, Phys. Rev. Lett.;(United States) **40** (1978).

[37] W. L. Jorgensen and J. Tirado-Rives, J. Phys. Chem. **100**, 14508 (1996).

[38] D. Agrawal, C.-Y. Huang, and H. McKinstry, Int. J. Thermophys. **12**, 697 (1991).

[39] F. Sudreau, D. Petit, and J. Boilot, J. Solid State Chem. **83**, 78 (1989).

[40] E. Gobechiya, Y. K. Kabalov, V. Petkov, and M. Sukhanov, Crystallogr. Rep **49**, 741 (2004).

[41] D. Petit, P. Colomban, G. Collin, and J. Boilot, Mater. Res. Bull. **21**, 365 (1986).

[42] M. Catti and S. Stramare, Solid State Ionics **136**, 489 (2000).

[43] P. Colomban, Solid State Ionics **21**, 97 (1986).

[44] H. Miyazaki et al., Japanese J. Appl. Phys. **47**, 7262 (2008).

[45] A. Yaroslavtsev and I. Stenina, Russ. J. Inorg. Chem. **51**, S97 (2006).

[46] V. Pet'kov and E. Asabina, Glass Ceram. **61**, 233 (2004).

[47] A. Orlova et al., J. Mater. Sci. **40**, 2741 (2005).

[48] K. Govindan Kutty, R. Asuvathraman, C. Mathews, and U. Varadaraju, Mater. Res. Bull. **29**, 1009 (1994).

[49] T. Oota and I. Yamai, J. Am. Ceram. Soc. **69**, 1 (1986).

[50] D. Woodcock et al., Chem. Commun. , 107 (1998).

Chapter 4

Influence of Si/P Ordering on Na^+ Transport in $Na_3Zr_2Si_2PO_{12}$[†]

4.1 Introduction

In their pioneering work Hong and Goodenough et al.[1, 2] demonstrated feasibility of fast ion conduction in several frameworks; solid solutions of the formula, $Na_{1+x}Zr_2Si_xP_{3-x}O_{12}$ where $0 \leq x \leq 3$, named NASICONs (for Na-superionic conductor) were particularly attractive for their high and three-dimensional conductivity and superior thermal stability[3–5]. The NASICON framework permits variety of ion substitutions, and serves a potential template for tailor making of solids for varied technological applications, such as solid electrolytes, low-thermal expansion materials[6–9], nuclear waste packaging matrices[10, 11], gas sensors etc[12–15].

The NASICONs consists of three dimensionally linked ZrO_6 octahedra sharing corners with SiO_4 and PO_4 tetrahedra, and stabilizes generally in the rhombohedral (space group $R\bar{3}c$)

[†]Publication based on this work: Supriya Roy and P. Padma Kumar, *Phys. Chem. Chem. Phys.*, **15**, 4965 (2013).

structure as detailed in Chapter 3. The $Na_{1+x}Zr_2Si_xP_{3-x}O_{12}$ -series, where $0 \leq x \leq 3$, exhibit many interesting structural and conductivity behaviour with composition. The *a*-parameter of the unit cell increases monotonically with *x*, while the *c*-parameter attains a maximum around $x = 2$ and decreases thereafter[16]. The Na^+ conductivity of the series also exhibit a maximum near the composition $x = 2$, which is about three orders of magnitude higher than the end members ($x = 0$ and $x = 3$)[16]. The compositions in the range $1.6 \leq x \leq 2.2$ has been reported to undergo monoclinic distortion at low temperature ($< 450K$).

Colomban has carried out detailed investigation of the high conducting $x = 2$ composition, and showed that the conductivity and phase transformations of the system is strongly influenced by the sintering temperature of the samples[17]. The material sintered at a higher temperature (1200°C) shows three phase transitions, two diffuse transitions at 60 K and 520 K, and a prominent transition around 423 K. This 423 K transition involves a structural phase change from monoclinic (indexed in $C2/c$ or $B2/b$ respectively in references [1, 16]) to rhombohedral-$R\bar{3}c$, and is associated with the increase of ionic conductivity from normal to superionic state [17]. However, the samples sintered at a lower temperatures (600 and 900°C) showed no signatures of phase transition across the temperature range of 300 to 800 K.

In figure 4.1 high temperature rhombohedral and low temperature monoclinic structure are shown. The eighteen Si/P positions (18e locations of $R\bar{3}c$) in the rhombohedral unit cell can be visualized as distributed across six equidistant *ab*- planes along the *c*-axis. However, the specific locations of silicon and phosphorous in the framework have been indistinguishable in previous experiments, due to their similar sizes[1, 16, 18]. The low-temperature monoclinic structural has often been described as a "slight monoclinic distortion" of its high temperature rhombohedral structure, by previous authors [1] to imply the closeness of spacial distributions of atoms in the two structures. The corner shared framework connectivity remain very similar in these two phase, though the silicon and phosphorous are distributed across two different crystallographic positions 4e and 8b in the monoclinic $C2/c$ structure, while in the rhombohedral counterpart they share same crystallographic sites, 18e of the $R\bar{3}c$ -space group. In the rhombohedral structure there are three Na sites Na(1), Na(2) and mid-Na. Among them

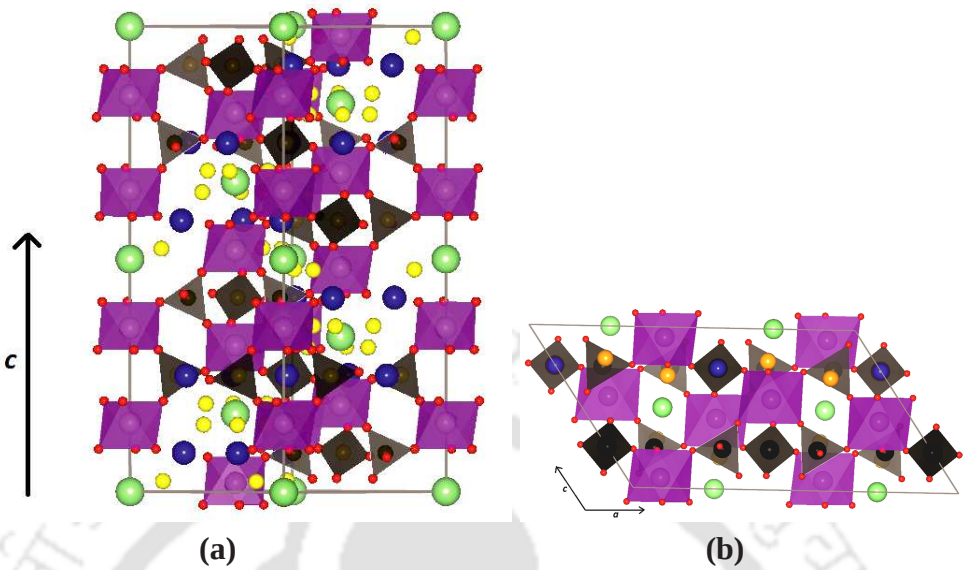

FIGURE 4.1: structure of the two phases of $Na_3Zr_2Si_2PO_{12}$, (a) the high-temperature rhombohedral phase, (b) the low-temperature monoclinic phase. The polyhedral framework of ZrO_6 (in pink) corner sharing with $(Si/P)O_4$ tetrahedra (dark) are shown along with the Na-sites, Na(1) (light green), Na(2) (blue), mid-Na (light yellow) and Na(3) (orange, in (b)). Oxygens are shown in red.

Na(1) (6b positions of $R\bar{3}c$) and Na(2) (18e positions of $R\bar{3}c$) are the prominent ones in terms of their occupancy[16]. In the monoclinic counterpart the conventional Na(2) sites of the rhombohedral structure are modified into two different sites, labelled Na(2) and Na(3). The new site Na(3) site of the monoclinic structure is slightly displaced from the Na(2) containing basal planes.

Previous experimental [16, 18, 19] as well as simulation studies[20, 21] have proposed that for the rhombohedral structure the preferred Na^+ conduction channels is the one connecting Na(1) and Na(2) site, through the mid-Na site. The Na(2) sites fall in the same basal planes as those of Si/P, and are three coordinated to the coplanar Si/P sites at a distance of 3.15 $\AA$. The Na(1) sites fall between these basal planes, and are six coordinated to the Si/P sites above and below it, but at a larger distance of 3.76 $\AA$. Thus, the different oxidation states of silicon (Si^{4+}) and phosphorous (P^{5+}) will presumably influence the energetic of Na^+ along the conduction channel due to their differential local coordination with Si and P. This prompts the present

molecular dynamics simulation of Na^+ mobility in NASICON frameworks with different Si/P ordering.

4.2 Method and Computational details

To begin with, a series of microcanonical molecular dynamics (NVE-MD) simulations are performed at 600 K on the high-conducting rhombohedral structure of $Na_3Zr_2Si_2PO_{12}$ (having different Si/P orderings) with the objective of investigating the role of Si/P ordering on Na^+ transport in the system. These results are discussed in section 4.3.1. A second series of MD studies in the isothermal-isobaric ensemble (NPT-MD) are carried out over 300-800 K in an effort to bridge the present simulation results to available experimental observation. The results of these NPT-MD studies discussed in section 4.3.2.

Molecular dynamics (MD) simulations on $Na_3Zr_2Si_2PO_{12}$ are performed employing the previously proposed interatomic potential [20],

$$U(r_{ij}) = \frac{q_i q_j}{r_{ij}} + \frac{A_{ij}(\sigma_i + \sigma_j)^{n_{ij}}}{r_{ij}^{n_{ij}}} - \frac{C_{ij}}{r_{ij}^6} \tag{4.1}$$

TABLE 4.1: Interaction potential parameters between, species X and oxygen, where $X = Na, Zr, Si, P$.

Species(X)	$q_X(\mid e \mid)$	$\sigma_X(\mathring{A})$	$A_{X-O}(eV)$	$C_{X-O}(eV.\mathring{A}^6)$	n_{X-O}
Na	0.702	1.13	0.1716	0.0	9
Zr	2.808	0.86	1.2126	11.917	9
Si	2.808	0.40	2.8059	11.529	9
P	3.510	0.31	3.6158	9.279	9
O	−1.404	1.21	0.3252	47.999	7

$A_{Na-Na} = 5\,eV$ and $n_{Na-Na} = 11$. All the other parameters not listed above are kept zero.

where q_i and σ_i are respectively the effective charge and ionic radius of i^{th} ion. r_{ij} is the interatomic distance, A_{ij} and C_{ij} are the overlap-repulsive energy and dispersion terms respectively between ion pairs i and j. These parameters are listed in Table 4.1. This interatomic potential has successfully reproduced a variety of structural properties and conductivity of $Na_{1+x}Zr_2Si_xP_{3-x}O_{12}$, over the entire range of composition, $0 \leq x \leq 3$ [20, 21]. This potential has been employed in the study of distortions and orientational disorder of the polyhedra in $MZr_2P_3O_{12}$(where M=Li, Na, K, Rb and Cs) and their role on the anisotropic variations of the lattice parameters and low-thermal expansivity, over wide range of temperatures as described in chapter 3.

4.2.1 Microcanonical Molecular Dynamics (NVE-MD)

In order to investigate the effect of Si/P ordering on Na^+ transport in the system, framework structures with different Si/P ordering are prepared as below:

1. Each of the six basal planes perpendicular to the *c*-axis contain two Si and one P in one unit cell (this structure shall be referred P1-P1-P1)(see figure 4.2).

2. Repeating units of two silicon rich planes, parallel to the *ab*-plane, sandwiching one phosphorous rich layer (shall be referred to as P0-P0-P3). There are two such units per unit cell (see figure 4.2).

3. Three random structures have been made by distributing silicon and phosphorous randomly across the Si/P sites in the simulation cell (referred to as Rand1, Rand2 and Rand3).

The simulated system consists of $3\times3\times1$ rhombohedral $R\bar{3}c$ unit cells of $Na_3Zr_2Si_2PO_{12}$ containing a total of 1080 ions. The unit cell parameters and coordinates of atoms are taken from the single crystal X-ray data of Boilot et al. at 623 K [16, 18]. Periodic boundary conditions are employed together with Ewald summation technique for convergence of long

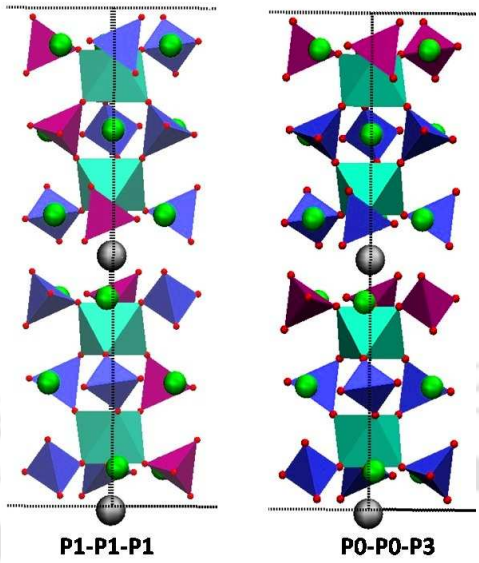

FIGURE 4.2: The two Si/P ordered frameworks of high-temperature rhombohedral phase of $Na_3Zr_2Si_2PO_{12}$ examined in the present MD study; (left) P1-P1-P1 structure and (right) P0-P0-P3. Only one column of "lantern units" of a unit cell along the *c*-axis, with SiO_4 (blue) and PO_4 tetrahedra (pink) sharing corners with ZrO_6 octahedra (light green) is shown. Na(1) and Na(2) sites are shown as gray and green balls, respectively.

range Coulombic interactions. After dedicating 2 nano seconds for equilibration, production runs of 6 nano seconds are carried out. A time step of 2 femto seconds is employed. The trajectory samples are stored at intervals of 200 pico seconds for further analysis. These NVE-MD simulations are performed using an in-house-developed MD code.

4.2.2 Isothermal-Isobaric Molecular Dynamics

To study the influence of Si/P ordering on the phase transition and activation energy of $Na_3Zr_2Si_2PO_{12}$, molecular dynamics calculations in the isothermal-isobaric ensemble (NPT-MD) simulations are carried out over 300-800 K. The NPT-MD simulations allows for change in shape and size of the supercell, and are best suited for investigation of structural phase transformations in solids. The interatomic potential mentioned earlier in this chapter (eqn. 4.1) is employed in these NPT-MD simulations as well. The simulations are started from the low-temperature monoclinic X-ray structure reported by Hong [1], with lattice parameters of these

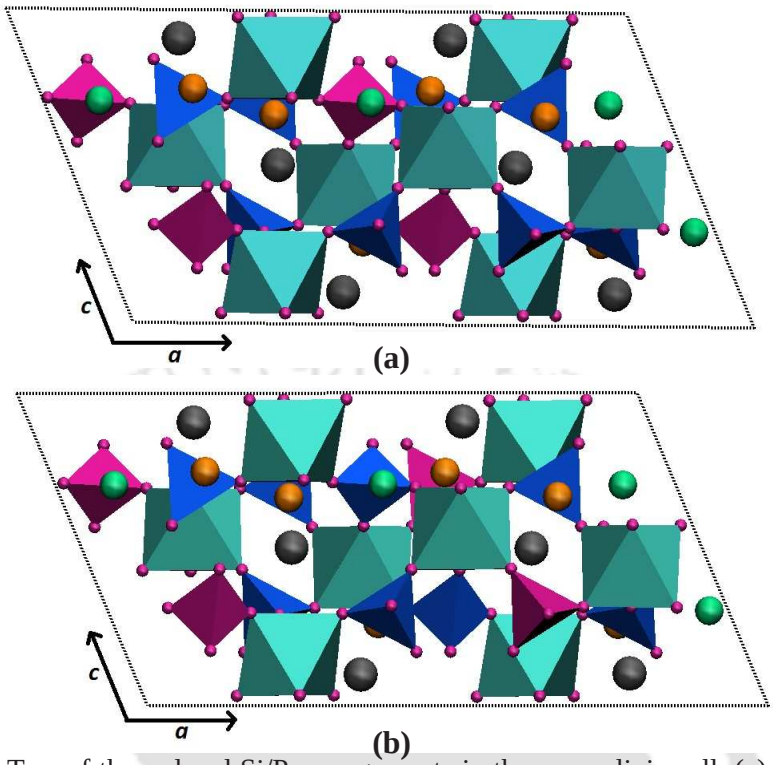

FIGURE 4.3: Two of the ordered Si/P arrangements in the monoclinic cell, (a) labelled Ord1 and (b) Ord2, used as the starting structures for NPT-MD simulations. The ZrO_6 -octahedra are shown in green, and the SiO_4 and PO_4-tetrahedra in blue and pink, respectively. The Na(1), Na(2) and Na(3) sites are shown respectively as dark-gray, green and orange balls.

monoclinic cell are $a = 15.586\AA$, $b = 9.029\AA$, $c = 9.205\AA$, $\alpha = 90.0°$, $\beta = 123.7°$, $\gamma = 90.0°$. One unit cell contains 4 formula units of $Na_3Zr_2Si_2PO_{12}$. The simulation supercell in this case consists of $2\times3\times3$ unit cells containing a total of 1440 atoms. As mentioned earlier, due to the similar sizes of the Si/P atoms the exact positions of Si and P atoms separately remain unknown.

Thus the following monoclinic structures having different Si/P orderings are investigated:

1. The Si and P atoms are distributed, respectively, over the 8f and 4e sites of the $C2/c$. Labelled Ord1, the arrangement is shown in figure 4.3(a). It shall be noted that Hong assumed this particular order in his original work[1], purely intuitively.

2. The Si/P atoms arranged as demonstrated in figure 4.3(b). Labelled Ord2, this arrangement introduces different local coordination of Si/P at the prominent Na(1), Na(2) and Na(3) sites of the $C2/c$, compared to Ord1.

3. The Si/P are arranged randomly over the $2 \times 3 \times 3$ unit cells forming the simulation super cell (labelled RandM; not shown).

In addition to the above, a series of NPT-MD simulations starting from the P1-P1-P1 rhombohedral structure (described in figure 4.2) are carried out over 800 to 300 K.

All NPT-MD simulations are carried out at a target pressure of 10 atmospheres. Simulations are typically of 5 nano seconds duration (for production) at a time step of 2 femto seconds. Trajectory has been written out after every 200 MD steps which are used for the calculation of dynamical properties of the system. The NPT-MD simulations has been carried out using the simulation package LAMMPS [22]. A tabulated form of the potential has been used, as the functional form describing the short-range interaction (see eqn. 4.1) is not available in the package. For better conservation of energy, the interatomic potential on a grid size of 125×10^{-6} $\AA$ is used.

4.3 Result and Discussion

4.3.1 Influence of Si/P ordering on Na^+ conductivity

The gross structural features of the NASICON framework, the polyhedra and their connectivity, are found insensitive to the different Si/P orders present. The radial distribution functions (RDF), g(r), between select ion pairs, Zr-O, Si-O, P-O and O-O, for the three frameworks with different Si/P orders shown in figure 4.4 are very similar to one another, demonstrating this. Though the starting structures involve average Si/P-O distances for all the tetrahedra, the system quickly relaxes, and SiO_4 and PO_4 tetrahedra assumes their respective natural dimensions. The bond lengths of covalently bonded ion pairs, Zr-O, Si-O and P-O, are respectively,

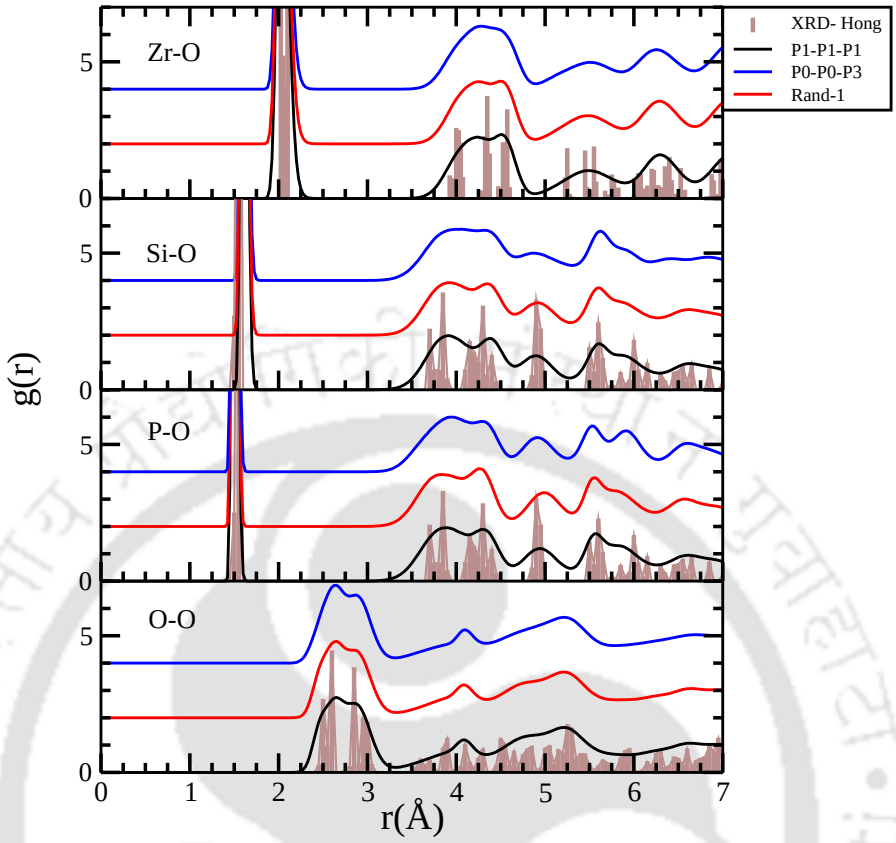

FIGURE 4.4: The radial distribution functions, g(r), between select ion pairs, Zr-O, Si-O, P-O and O-O, for $Na_3Zr_2Si_2PO_{12}$ frameworks with different Si/P orders at 623 K. The intensities of the first peaks are truncated for optimal view of the function at long range. The vertical bars in brown are for the corresponding X-ray structure [16, 18] in arbitrary units. The functions are uniformly displaced along the Y-axis for clarity.

2.07, 1.61 and 1.52 $\AA$, and with sharp coordination numbers of 6, 4 and 4, in agreement with previous X-ray studies[1].

The mean squared displacements (MSD) of Na^+ ions at 623 K in frameworks with different Si/P ordering are shown in figure 4.5. The MSD of Na^+ ions in the ordered structure, P1-P1-P1, are significantly higher compared to the orther ordered structure P0-P0-P3 over the same period of time, and those in the random structures are intermediate. The self diffusion coefficient of Na^+ ions calculated for the P1-P1-P1 structure (D = 0.11×10^{-8} $m^2 sec^{-1}$; conductivity, σ_{dc} = 0.366 $S.cm^{-1}$), is more than an order of magnitude higher than that in the P0-P0-P3 structure (D = 0.31×10^{-10} $m^2 sec^{-1}$; conductivity, σ_{dc} = 0.01 $S.cm^{-1}$). For the

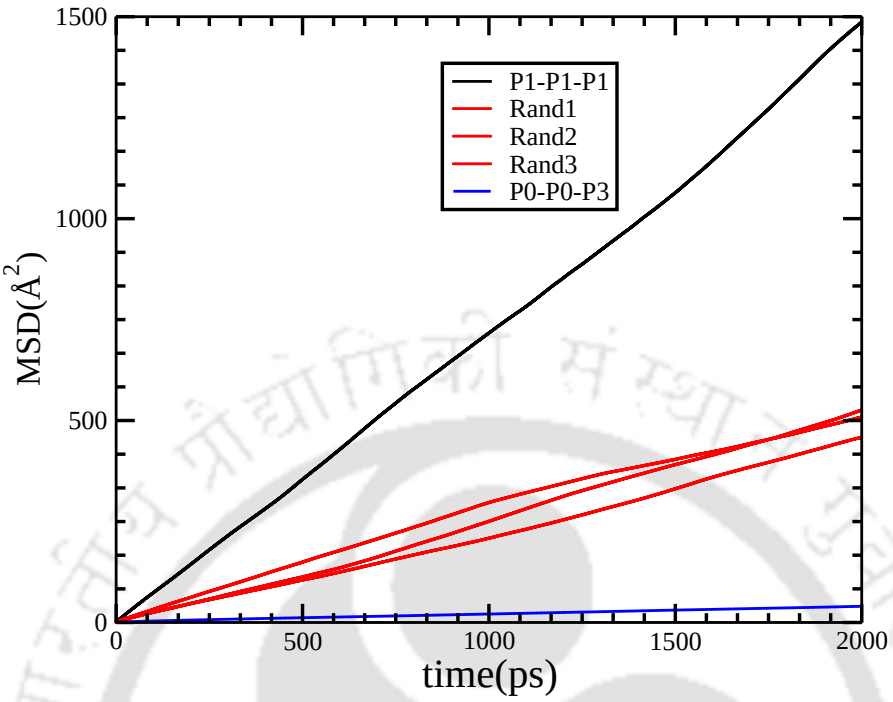

FIGURE 4.5: The mean squared displacement of Na^+ ions with time in the NASICON frameworks having different Si/P ordering from MD simulation at 623 K.

three random structures the conductivities show very similar values (σ_{dc} = 0.14, 0.138 and 0.111 $S.cm^{-1}$). This proves unambiguously that the Si/P order plays a very important role on the Na^+ transport in the NASICON framework.

It shall be noted that several previous experimental studies have measured the activation energies and conductivities of NASICONs at variance[1, 2, 16, 19, 23]. Colomban showed that samples heat treated at higher temperatures systematically measured higher conductivities [17]. The present simulation results complement their observation proposing that higher sintering temperatures not only improve their X-ray crystallinity but also alter the Si/P ordering in favour of the P1-P1-P1 structure, with an evenly distributed phosphorous arrangement along the *c*-axis of the unit cell.

Microscopic details relating to the energetics, atomic density profiles, site energies and percolation pathways of Na^+ ions are analyzed to understand this effect. The radial distribution functions (RDFs) between the Si/P with Na^+ ions in the frameworks with different

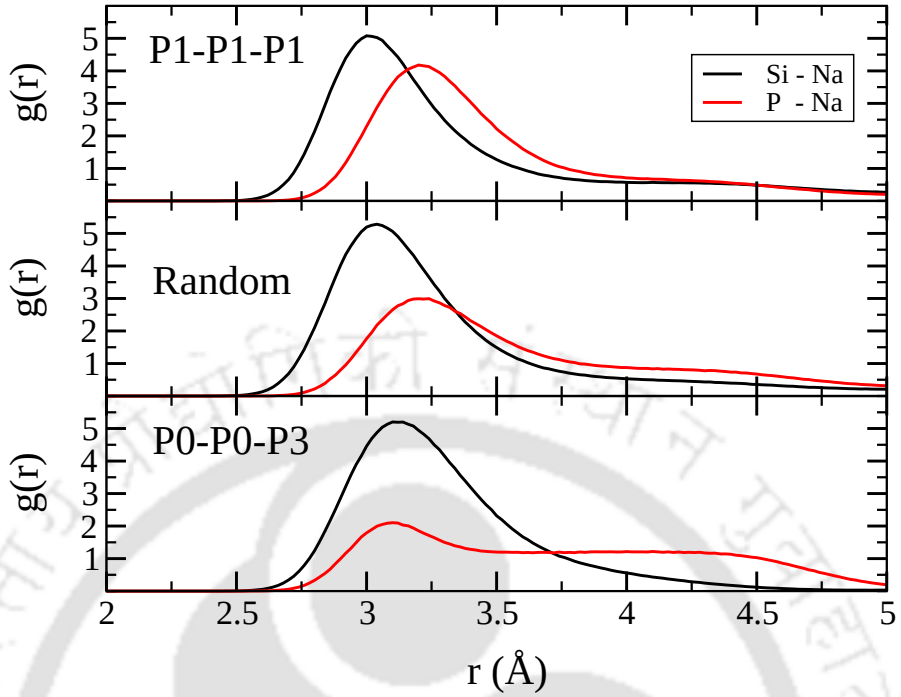

FIGURE 4.6: The radial distribution functions for Na^+ ions with respect to silicon and phosphorous positions calculated for the framework structures with different Si/P ordering from MD simulation at 623 K.

Si/P ordering is shown in figure 4.6. These functions are calculated with respect to Si and P ions as the origin so that their relative abundance in the system (2:1) are not reflected in the intensities. The first peak of the P-Na RDF are either lower in intensity or occur at a larger distance compared to the Si-Na RDF in all three case, despite the fact that Si/P share crystallographically equivalent positions in the structure. Thus the Na^+ ions prefer to move away from the phosphorous locations, suggesting the stronger coulombic repulsion between the Na^+ and phosphorous ions is operative in the system.

Originating dominantly from coulombic interaction this effect was quiet natural to expect, though eluded previous studies. Probably, thought of having no significant impact on ion transport as the framework cations are screened away by the oxygen environment from the Na^+ conducting channels; neither any quantification of the effects were available nor controlling Si/P locations were amenable to experiments for systematic investigation.

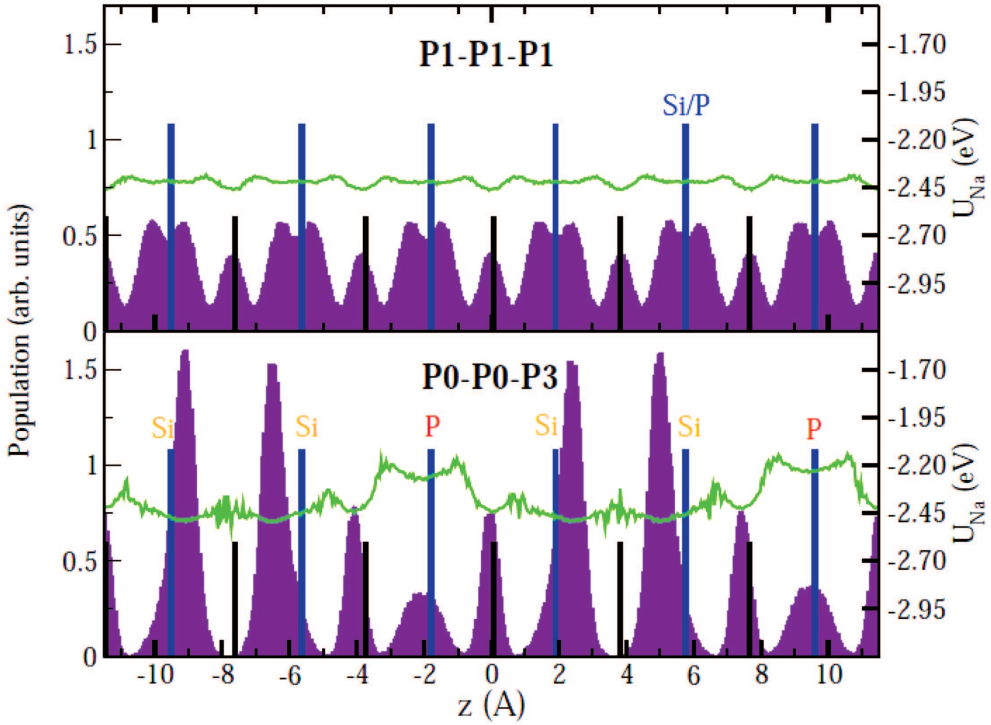

FIGURE 4.7: The potential energy of Na^+ along the *z*-axis (green) averaged over the MD trajectory at 623 K, for the two structures P1-P1-P1 and P0-P0-P3. The averaged atomic density profile for the Na^+ ions projected on the *z*-axis is shown. The Si/P and Na(2) locations along the *z*-axis is shown as vertical blue bars, and the Na(1) locations are shown as black bars.

The potential energy of individual Na^+ ions due to its interaction with the rest of the system, including other Na^+ ions as well as the framework ions, provides the most direct information on the barriers to ion transport. The quantity can be calculated as,

$$u_i = \frac{1}{2} \sum_{j=1_{j\neq i}}^{N} u_{ij}(r_{ij}) \tag{4.2}$$

such that the total potential energy u_{tot} of the system is written as,

$$u_{tot} = \sum_{i=1}^{N} u_i \tag{4.3}$$

where u_i is the potential energy of the i^{th} ion, N is the total number of ions in the system,

and r_{ij} the separation between a pair of ions under periodic boundary conditions. Employing this equation the potential energy profile of Na^+ ions along the *z*-axis of the rhombohedral cell, averaged over all the Na^+ ions and over the stored trajectory (after folding it back in to a single unit cell), is calculated. Shown in figure 4.7, the energies show significant differences between the frameworks having different Si/P order.

Evidently, the high conducting P1-P1-P1 structure offers smoother potential energy profile with relatively low barriers to the Na^+ ions. Consequently a smoother distribution of Na^+ along the *z*-axis that is reminiscent of high ion mobility is observed. The low conducting P0-P0-P3 structure, on the other hand, exhibits larger undulations in the potential energy profile, thus greater energy barriers to Na^+ transport in the framework. The P0-P0-P3 structure evidently results in well resolved peaks in the Na^+ distribution suggesting localization of sodium ions. Thus an uniform distribution of Si/P ions along the *z*-axis, as in the case of the P1-P1-P1 structure, results a smoother potential energy profile favourable to ion transport.

The three dimensional distribution of Na^+ in the rhombohedral cell is demonstrated in figure 4.8 for the two Si/P orders, by collapsing their stored positions in to a single unit cell. For the P1-P1-P1 structure a well developed percolation path of Na^+ ions connecting the Na(1)-Na(2) channel is evidenced consistent with the high conductivity observed. The P0-P0-P3 structure results in islands of Na^+ population with rather poor connectivity across them.

This phenomenon could be one of the major reasons for the significant variations in measurements of conductivity of NASICONs samples differently heat treated[17]. Further, we note the plausibility, that the anomalous variation in the conductivity of $Na_{1+x}Zr_2Si_xP_{3-x}O_{12}$, which peaks around x=2, is related to a smoothening of the potential energy barrier for Na^+ ions due, partially to different Si/P distributions, among other previously proposed factors such as the opening of bottlenecks[19] and Na^+- Na^+ correlations[16, 24] a proposal calling for further investigations.

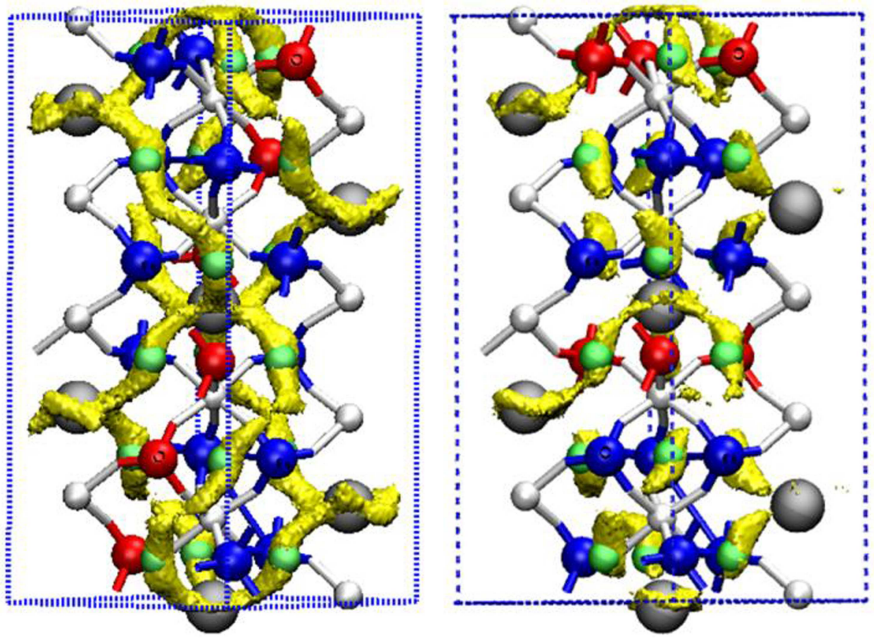

FIGURE 4.8: Three dimensional distributions of Na^+ ions (yellow) in the rhombohedral cell for the two framework structures with different Si/P orders, P1-P1-P1 (left-panel) and P0-P0-P3 (right-panel), from MD simulation at 623 K. The ball-stick model shows one configuration of the framework cations, Zr (light grey), Si (blue) and P (red), bridged through oxygen (not shown). The locations of the predominant Na^+ sites Na(1) (dark grey) and Na(2) (green) are also shown.

Finally, some insight into the Na^+ distributions on basal planes perpendicular to the c-axis for the frameworks with different Si/P orders is gained by collecting ions in a thin slab of 0.3 $\AA$ around a chosen height, z. In figure 4.9(a) qualitative demonstration of Na^+ distribution on select basal planes of P1-P1-P1 (top-panel) and P0-P0-P3 structures (bottom-panel) are shown. Figure 4.9(a) shows the Na^+ distribution for one of the basal planes containing Na(1) sites ($z = nc/6$, where n can be $0, 1, 2, ..., 5$). In figure 4.9(b) the distribution on one of the planes containing the Na(2) sites ($z = (2n+1)c/12, n = 0, 1, 2, ..., 5$) are shown (compare with figure 4.8), along with distributions for the coplanar Si and P ions. Larger thermal amplitudes of Na^+ are observed along the basal planes at Na(1) sites consistent with figure 4.8. In figure 4.9(c) Na^+ population on one of the basal plane containing Na(1) sites (at $z = 0, c/3, c/2$ or $5c/6$, in figure 4.8) located between an Si-rich and a P-rich planes of the P0-P0-P3 structure are shown. No appreciable Na^+ population is observed on cross sections through Na(1) sites

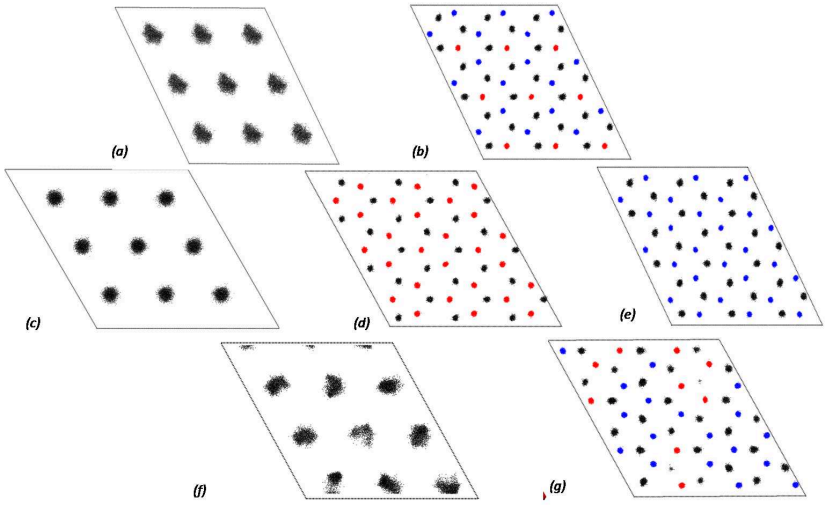

FIGURE 4.9: The distribution of Na^+ ions (black) in the rhombohedral simulation cell (of $3 \times 3 \times 1$ unit cells) on select cross sections of the c-axis for the three framework structures, P1-P1-P1 (top panel), P0-P0-P3 (middle panel), random (bottom panel) from MD simulation at 623 K. The in-plane Si and P distributions are shown in blue and red respectively. See text for details.

falling between two Si rich planes (at $z = c/6$ or $2c/3$, in figure 4.8), hence not shown in figure 4.9. The in-plane distributions of Na^+ at Na(2) sites of the P0-P0-P3 structures are qualitatively similar irrespective of their coplanar neighbors are (phosphorous figure 4.9(d)) or silicon (figure 4.9 (e)). However, from figure 4.7, the preference of Na^+ ions in favour of Na(2) sites on Si-rich layers, though somewhat off-centered, is evident. The large occupancies at these Na(2) sites, presumably, result in the low occupancy at Na(1) sites located in between the Si-rich layers owing to $Na^+ - Na^+$ repulsion. Figure 4.9(f) shows the distribution of Na^+ ions on an arbitrarily chosen basal plane containing Na(1) sites of the Rand1 structure. It shows non uniform population density at different Na(1) sites which is reflecting the effect of random Si/P neighboring to these Na(1) sites. In figure 4.9(g) Na^+ distribution at some randomly picked Na(2) planes is shown. The population of different Na(2) sites are observed to be influenced by their local Si/P coordination. The Na(2) sites surrounded by three P atoms shows very little occupancy while surrounded by lesser no of P atoms shows gradually more occupancy. Overall, the Na^+ distributions at Na(1) sites suggests larger thermal amplitude along the *ab*- plane compared to Na(2) sites, while the converse is true along the *c*-direction.

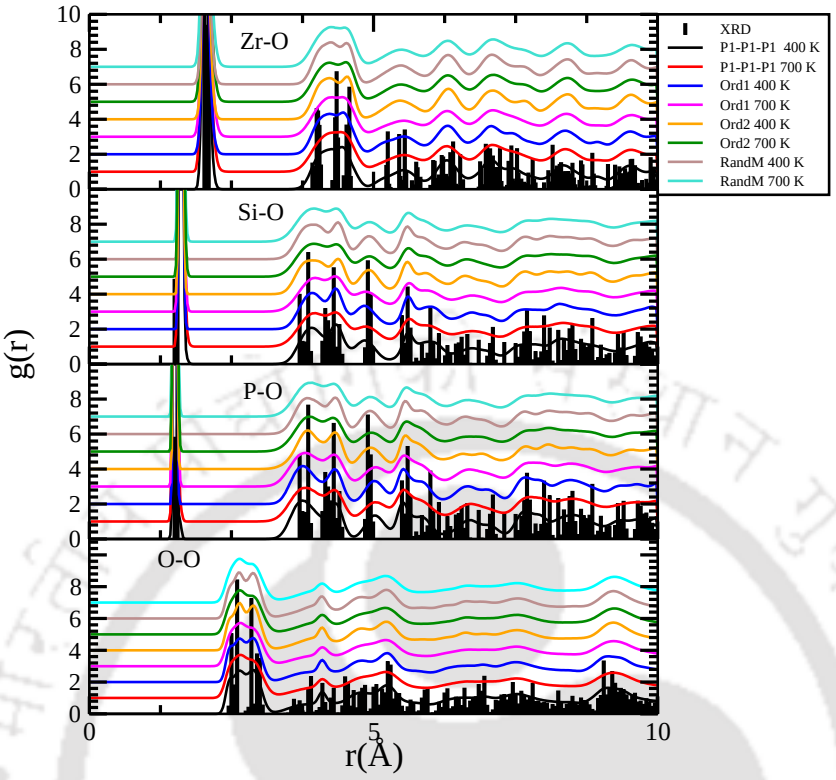

FIGURE 4.10: Radial distribution functions (RDFs) of ion pairs Zr-O, Si-O, P-O and O-O for different Si/P ordering at 400 K and 700 K. The corresponding RDFs calculated from the monoclinic X-ray structure (with their intensities scaled down for ease of comparison) are shown as bar-plots. The legend on the right of the top panel is common to all the plots.

4.3.2 Effect of Si/P distribution on activation energy

Having established the significance of Si/P ordering on ion transport in $Na_3Zr_2Si_2PO_{12}$, the effort was on bridging the present simulation results to available experimental observations. To this effect, the trajectories of isothermal-isobaric ensemble MD (NPT-MD) simulations starting from the different Si/P ordered structures, described in section 4.2.2, are analyzed for various structural, thermodynamics and dynamics properties.

The RDFs of select ion pairs, Zr-O, P-O, Si-O and O-O, for different Si/P-ordered structures over 300 - 800 K are calculated. The essential features of these RDFs are demonstrated in figure 4.10 with the help of one for the low (400 K) and one for high temperature (700 K). It shows no noticeable changes suggesting that the frameworks of all the different Si/P

ordered $Na_3Zr_2Si_2PO_{12}$ remain intact across the temperature range. The unit cell parameters of the simulation cell in all cases retained the symmetry of the respective starting structures across the entire temperature range examined. Thus no structural indicators of a monoclinic to rhombohedral transition was observed for any of the different Si/P ordered systems.

The systematic investigation by Colomban[17] showed that the thermodynamic signatures, such heat capacity, as well as the activation energy for ionic conductivity during the monoclinic to rhombohedral transition have a strong dependence on the thermal history of the samples. The samples sintered at high temperature (1200^oC) showed sharper features of the phase transition, including a prominent peak in the heat capacity and a significant change of slope in the Arrhenius curve around the transition temperature (~ 450 K). In sharp contrast to this, no significant thermodynamic signatures of phase change was observed[17] for samples heat treated at lower temperatures (900 and 600^oC). The activation energies for ionic conductivity of the samples heat treated at 900^oC, fitted to the high and low temperature regions of the Arrhenius plot are very close, 0.22 and 0.29 eV respectively [17]. However, the average energy, heat capacity (C_p) and isothermal compressibility estimated over the range of 300-800 K (not shown here) from the present MD simulations did not present any convincing signatures for a phase transformation that was expected.

Figure 4.11 shows the Arrhenius plot of conductivity from present MD simulations starting from the different Si/P ordered framework structures detailed in section 4.2.2. The experimental conductivity data for $Na_3Zr_2Si_2PO_{12}$ samples sintered at 1200^oC and 900^oC, extracted from Colomban's work[17] is presented for comparison. Interestingly, the NPT-MD simulations starting from the monoclinic structures having ordered Si/P arrangements, Ord1 and Ord2 (refer to section 4.2.2), show sharp change of slope in the Arrhenius plot around 500 K (figure 4.11). This behaviour closely resembles the high-temperature sintered samples of $Na_3Zr_2Si_2PO_{12}$, examined by Colomban. The NPT-MD simulations starting from the RandM (having a randomly distributed Si/P arrangement) exhibits a nearly linear behaviour across the entire temperature range, in striking qualitative resemblance to the low-temperature sintered

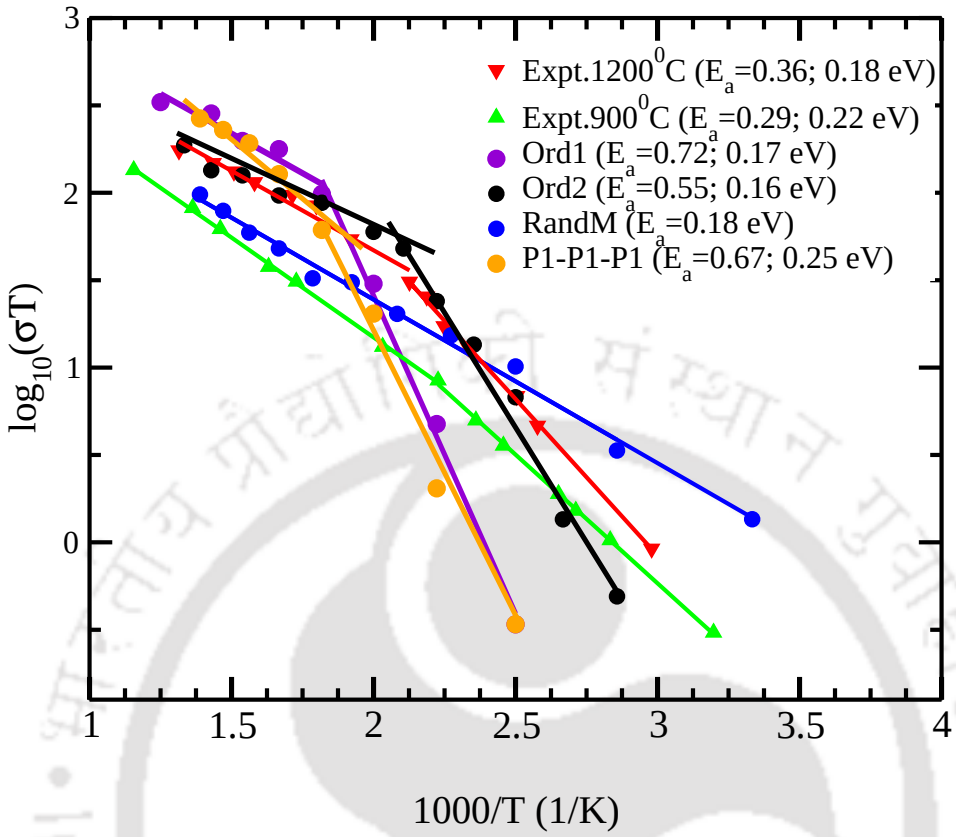

FIGURE 4.11: Arrhenius plot for different Si-P ordering from simulation as well as the data extracted from the Colomban's experimental work.

samples. The NPT-MD results for the P1-P1-P1 (the best conducting rhombohedral structure having an ordered arrangement of Si/P - refer to section 4.3.1) and Ord1 (monoclinic) structures are very similar owing to the closeness in their Si/P arrangements. The quantitative agreement in the Arrhenius plots between simulation and experiments are impressive in the high temperatures, where the typical error bars in the conductivity estimated from simulation are lower due to frequent ion hops. Over all, these results suggest that the Si/P ordering in $Na_3Zr_2Si_2PO_{12}$ is sensitive to the sintering temperatures; higher the sintering temperature (and for longer durations as well) better the ordering. The thermodynamics of these systems may marginally favour an ordered Si/P arrangement, which is attainable at higher sintering temperatures due to higher diffusive mixing of silicon and phosphorous ions.

Based on his spectroscopic studies Colomban also discussed the influence of sintering on

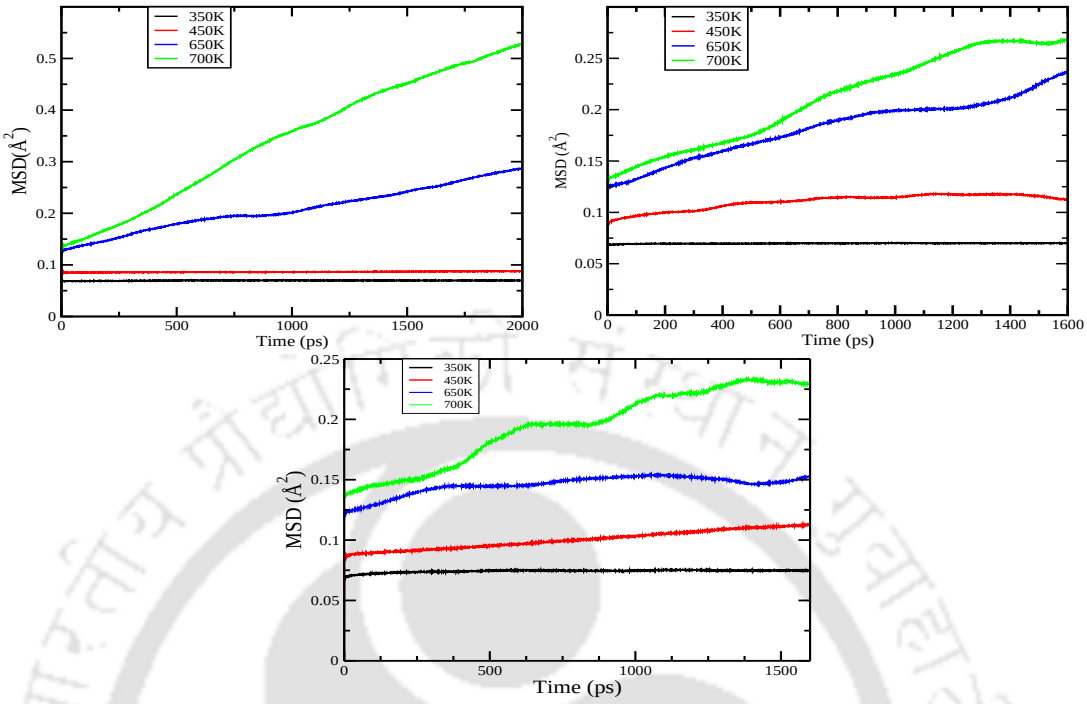

FIGURE 4.12: Means square displacement for oxygen atoms for high and low temperatures for different Si-P Ordering (a)Ord1 (b) Ord2 (c) random.

polyhedral disorder in $Na_3Zr_2Si_2PO_{12}$ systems [17]. It was proposed that high temperature sintered material is found to show low static disorder at low temperature and high dynamical disorder above the 423 K transitions. The converse was found true for the low- temperature sintered samples. In figure 4.12 mean square displacement (MSD) of oxygen for $Na_3Zr_2Si_2PO_{12}$-frameworks having different Si/P orders are plotted for low (400 K) and high (700 K) temperatures. For all the three cases a slow convergence of oxygen msd is evidenced at the higher temperature. These slow convergence of MSDs suggest the large amplitude motion of oxygens, associated possibly with low-frequency librational modes of the polyhedra similar to those discussed in Chapter 3 of this thesis. It shall be noted that these are not diffusive modes of oxygens, for (1) the (Si/P)-O and Zr-O bond lengths and the corresponding coordination numbers are intact and (2) the amplitudes of these MSD are very small 0.5 to 0.7 Å, which was further confirmed through visual examinations of the final structure after long NPT-MD runs. Interestingly, the higher values of MSD correspond to the Ord1 and Ord2 having ordered Si/P arrangements, in agreement with Colomban's proposal.

The transport mechanism that results in the change in activation energy of $Na_3Zr_2Si_2PO_{12}$ is not clear yet. It would be interesting to investigate if the observed polyhedral disorder plays any role in dictating the high temperature Na^+ transport in these systems.

4.4 Conclusion

The results presented here demonstrate, for the first time, that the Si/P order in $Na_3Zr_2Si_2PO_{12}$ has a profound influence on Na^+ conductivity in the system. The Si/P arrangement with one phosphorous and two silicon in each of the six basal planes perpendicular to the *c*-axis of the rhombohedral cell offers low energy barriers thus promoting the Na^+ transport in the system. The origin of this phenomenon is traced back to the stronger coulombic repulsion between Na^+ and P relative to that with Si.

This Si/P arrangements also found to be controlling the activation energy of this material. Present MD simulations on $Na_3Zr_2Si_2PO_{12}$ having ordered Si/P arrangements shows sharp changes in activation energies around 500 K, in good qualitative agreement with high-temperature sintered samples examined by Colomban [17]. Framework with random Si/P arrangement leads to a single activation energy across the temperature range (300 -800 K), and compares well with the low-temperature sintered samples of Colomban [17]. Thus the present simulation results suggest that different sintering temperature influence the Si/P ordering of $Na_3Zr_2Si_2PO_{12}$ material and thus, in turn, the conductivity behaviour. Evidence for dynamical orientational disorder of the polyhedra is provided, the role of which on the high conductivity in $Na_3Zr_2Si_2PO_{12}$ systems calls for further experimental and theoretical investigation.

The present molecular dynamics studies recognizes a new structural feature that control fast ion transport in $Na_3Zr_2Si_2PO_{12}$. Originating out of simple coulombic interactions, it is expected that, this effect will be omnipresent in all fast ion conductors having aliovalent

substitutions, though with varying tenacity. This phenomenon thus bears far-reaching significance, beyond the NASICON family, in the understanding of fast ion transport in solids and their tailor making.

Bibliography

[1] H.-P. Hong, Mater. Res. Bull. **11**, 173 (1976).

[2] J. Goodenough, H.-P. Hong, and J. Kafalas, Mater. Res. Bull. **11**, 203 (1976).

[3] H. Xie, Y. Li, and J. B. Goodenough, RSC Adv. **1**, 1728 (2011).

[4] N. Anantharamulu et al., J. Mater. Sci. **46**, 2821 (2011).

[5] H. Kabbour, D. Coillot, M. Colmont, C. Masquelier, and O. Mentré, J. Am. Chem. Soc. **133**, 11900 (2011).

[6] R. Roy, D. Agrawal, J. Alamo, and R. Roy, Mater. Res. Bull. **19**, 471 (1984).

[7] R. Roy, D. K. Agrawal, and H. A. McKinstry, Annu. Rev. Mater. Sci. **19**, 59 (1989).

[8] V. Pet'kov and E. Asabina, Glass Ceram. **61**, 233 (2004).

[9] A. Yaroslavtsev and I. Stenina, Russ. J. Inorg. Chem. **51**, S97 (2006).

[10] B. Scheetz, D. Agrawal, E. Breval, and R. Roy, Waste Management **14**, 489 (1994).

[11] R. Roy, E. Vance, and J. Alamo, Mater. Res. Bull. **17**, 585 (1982).

[12] K. Frank, H. Kohler, and U. Guth, Ionics **14**, 363 (2008).

[13] A. Hetznecker, H. Kohler, U. Schönauer, and U. Guth, Sens. Actuators, B **99**, 373 (2004).

[14] A. Hetznecker, H. Kohler, and U. Guth, Sens. Actuators, B **120**, 378 (2007).

[15] H. Aono, Y. Sadaoka, L. Montanaro, E. Bartolomeo, and E. Traversa, J. Am. Ceram. Soc. **85**, 585 (2002).

[16] J.-P. Boilot, G. Collin, and P. Colomban, J. Solid State Chem. **73**, 160 (1988).

[17] P. Colomban, Solid State Ionics **21**, 97 (1986).

[18] J. Boilot, G. Collin, and P. Colomban, Mater. Res. Bull. **22**, 669 (1987).

[19] H. Kohler, H. Schulz, and O. Melnikov, Mater. Res. Bull. **18**, 1143 (1983).

[20] P. P. Kumar and S. Yashonath, J. Am. Chem. Soc. **124**, 3828 (2002).

[21] P. P. Kumar and S. Yashonath, J. Phys. Chem. B **106**, 7081 (2002).

[22] S. Plimpton, J. Comput. Phys. **117**, 1 (1995).

[23] J.-S. Lee, C.-M. Chang, Y. I. Lee, J.-H. Lee, and S.-H. Hong, J. Am. Ceram. Soc. **87**, 305 (2004).

[24] S. H. Jacobson, M. A. Ratner, and A. Nitzan, Phys. Rev. B **23**, 1580 (1981).

Chapter 5

Influence of Cationic Ordering on Fast Ion Transport in Solids: Molecular Dynamics Investigation of NASICONs[†]

5.1 Introduction

The $Na_{1+x}Zr_2SiP_{3-x}O_{12}$, $0 \leq x \leq 3$, series forms one of the most extensively investigated systems, and is known to exhibit a maximum in ionic conductivity around x=2, for $Na_{1+x}Zr_2SiP_{3-x}O_{12}$ (dc conductivity, $\sigma_{dc} \approx 10^{-1} S/cm$ at 573 K), while the end members x=0 and x=3 show significantly lower conductivity (of the order of $\sigma_{dc} \approx 10^{-4} S/cm$) [1–6]. The intermediate composition with $x = 1$, $Na_2Zr_2SiP_2O_{12}$ is also a good ionic conductor with $\sigma_{dc} = 0.018\ S/cm$ at 573 K. This composition does not show any phase transition and stabilizes in rhombohedral crystal symmetry for all the temperature range. It should be mentioned that the compostions of $Na_{1+x}Zr_2SiP_{3-x}O_{12}$ series in the the range $1.6 \leq x \leq 2.2$ shows slight monoclinic distortions at room temperature.

[†]Publication based on this work: S. Roy and P. Padma Kumar, *Solid State Ionics.*(under review)

In the previous chapter, based on our NVE-molecular dynamics study we proposed that Si/P order in the NASICON framework plays an important role on Na^+ transport in the high conducting $Na_3Zr_2Si_2PO_{12}$. The stronger Coulombic repulsion between Na^+ and P^{5+} ions modify the local electrostatic potential energy barrier for Na^+ along the conduction channel, depending on the P^{5+} locations in the unit cell. Thus certain Si/P arrangements result in more than one order of magnitude conductivity over other, suggesting a new structural feature that control fast ion transport in solids. The effect of this Si/P ordering on the activation energy behavior of $Na_3Zr_2Si_2PO_{12}$ has also been studied using constant pressure, constant temperature molecular dynamics method. Two of the ordred structures showed sharper changes in the slope of Arrhenius plot similar to high temperature sintered material reported by Colomban et al.[7], while the framework structure with randomly distributed Si/P showed no change in slope thus behaving similar to the low temperature sintered material. Motivated by these results described in Chapter 4 is extended to the $x = 1$ composition $Na_2Zr_2SiP_2O_{12}$. The investigation on the role of Si/P ordering on $Na_2Zr_2SiP_2O_{12}$ predicts predominantly two dimension Na^+ transport for certain Si/P ordering in the NASICON framework which is otherwise known to be isotropic.

5.1.1 Method

Microcanonical molecular dynamics (NVE-MD) simulations are performed at 623 K employing the inter atomic potential,[8, 9]

$$U(r_{ij}) = \frac{q_i q_j}{r_{ij}} + \frac{A_{ij}(\sigma_i + \sigma_j)^{n_{ij}}}{r_{ij}^{n_{ij}}} - \frac{C_{ij}}{r_{ij}^6} \tag{5.1}$$

where q_i and σ_i are respectively the effective charge and ionic radius of i^{th} ion. r_{ij} is the interatomic distance, A_{ij} and C_{ij} are the overlap-repulsive energy and dispersion terms respectively between ion pairs i and j. These parameters are listed in table 1 of chapter 4.

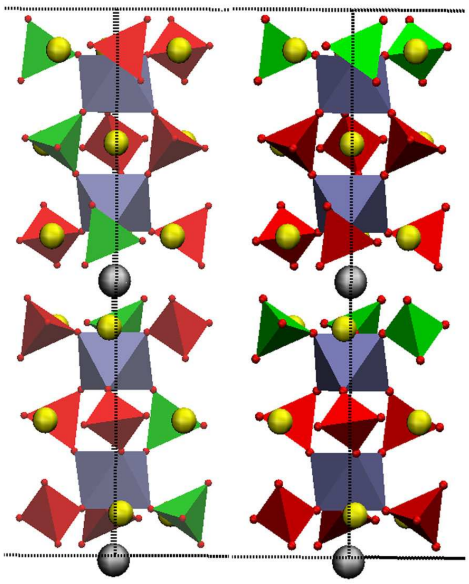

(S1-S1-S1) (S0-S0-S3)

FIGURE 5.1: The two Si/P ordered frameworks of $Na_2Zr_2SiP_2O_{12}$; S1-S1-S1 structure (on left) and S0-S0-S3 (on right). One column of 'lantern units along the *c*-axis is shown along with all the SiO_4(green) and PO_4tetrahedra (red), and few a ZrO_6 octahedra (violet) in a unit cell. A few of the prominent Na^+ sites, Na(1) (grey) and Na(2) (yellow), are also shown.

The simulations are performed on 3×3×1 rhombohedral $R\bar{3}c$ unit cells of $Na_2Zr_2SiP_2O_{12}$ containing a total of 1026 ions, starting from the X-ray structure at 623 K[1]. However, in the absence of specific knowledge on the Si and P locations in the unit cell, three structural models (figure 5.1), differing only in their Si/P order in the framework, are investigated. The eighteen $(Si/P)O_4$ tetrahedra in a unit cell are located on six basal planes, parallel to the *a*-*b* plane, at a spacing of $c/6$ along the *c*-axis. The first structure, labelled S1-S1-S1 (left panel in figure 5.1), has one SiO_4 tetrahedron and two PO_4 tetrahedra on each of the basal planes. The second structure, labeled S0-S0-S3, has repeating units of two phosphorous rich planes sandwiching one silicon rich layer (right panel in figure 5.1) two such units per unit cell. One random (Si/P) structure is made by distributing Si/P atoms randomly on the simulation cell. It may be noted that the interchange of Si and P ions in these two frameworks correspond to the two ordered structures, P1-P1-P1 and P0-P0-P3, of the x=2 composition, $Na_3Zr_2Si_2PO_{12}$, where our previous investigations discussed in chapter 4 predicted more than one order higher

Na^+ conductivity for the former.

Periodic boundary conditions under minimum image convention are imposed for calculation of short range interactions, while Ewald summation technique is employed for convergence of long-range Coulombic interactions[10](discussed in chapter 2). Newtons equations of motion are integrated, for all the 1026 ions, using velocity-Verlet algorithm (discussed in chapter 2) at a time step of 2 femto seconds. For temperature control 0.5 nano seconds are dedicated through velocity scaling at the start of the simulation and 2 nanoseconds dedicated for equilibration of the system. The production runs are 6 nano seconds long, during which trajectory samples are stored at intervals of 0.4 pico seconds for analysis of structural and dynamical properties.

5.1.2 Result and Discussion

The radial distribution functions (RDF), g(r), between select ion pairs, Zr-O, Si-O, P-O and O-O for the S1-S1-S1 and S0-S0-S3 structures having different Si/P orders are shown in figure 5.2, along with those for the X-ray structure[1]. While the Zr-O and O-O distributions are nearly identical for the three Si/P orders, the corresponding Si-O and P-O distributions show slight differences at long ranges, owing to different locations of Si and P in the framework. The Zr-O, Si-O and P-O bond-lengths in the simulated system are respectively 2.07, 1.61 and 1.52 $\AA$ in agreement with previous X-ray studies[1]. Since Si/P locations are indistinguishable in X-ray study corresponding Si-O and P-O RDFs are identical, and their first peak positions reflect average Si/P-O bond lengths, not their individual values. Overall, the RDFs suggest that the Si/P order in the framework do not result in appreciable changes in the NASICON framework.

The mean squared displacements (MSD) of Na^+ ions at 623 K for $Na_2Zr_2SiP_2O_{12}$ having S1-S1-S1, S0-S0-S3 and random (Si/P) ordering are shown in figure 5.3. A comparison to the high conducting x=2 composition, $Na_3Zr_2Si_2PO_{12}$, of P1-P1-P1 and P0-P0-P3 structures are provided for comparison. It should be mentioned that Si/P ordering in the P1-P1-P1

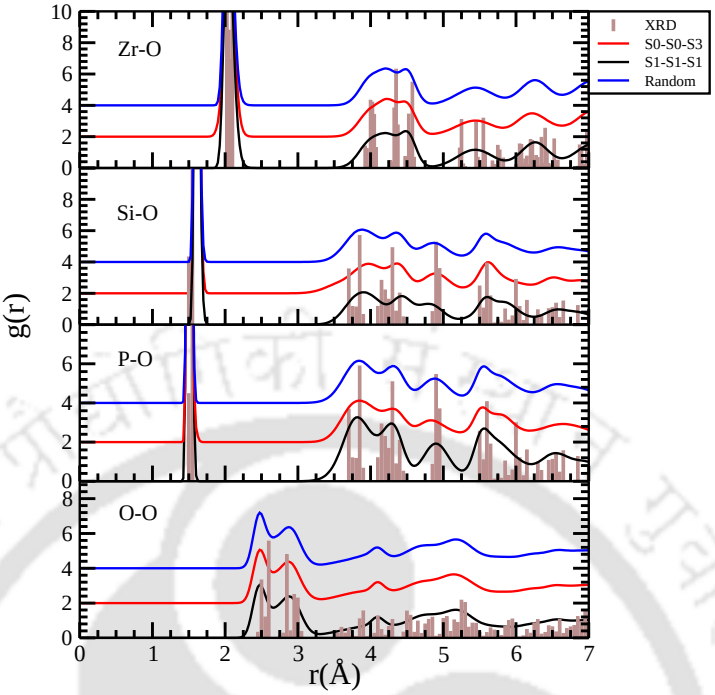

FIGURE 5.2: The radial distribution functions, g(r), between select ion pairs, Zr-O, Si-O, P-O and O-O, for $Na_2Zr_2SiP_2O_{12}$ frameworks with two different Si/P orders from MD simulation at 623 K. The intensities of the first peaks are truncated for optimal view of the function at long range. The vertical bars in brown are for the corresponding X-ray structure [5] in arbitrary units. The functions are uniformly displaced along the Y-axis for clarity.

and P0-P0-P3 structures are just the interchange of Si/P locations of S1-S1-S1 and S0-S0-S3 structures respectively. Self diffusion coefficient of Na^+ ions are conveniently calculated from the slope of the curve using eqn.2.53 in chapter 2.

Our previous MD simulation in chapter 4 showed that the msd of Na^+ ions in the P1-P1-P1 structure of $Na_3Zr_2Si_2PO_{12}$ (where one P and two Si are arranged on each of the six basal planes along the *c*-axis per unit cell) are more than an order higher than the P0-P0-P3 structure (where two Si-rich planes, followed by one P-rich plane are staked along the *c*-axis). In the present case of $Na_2Zr_2SiP_2O_{12}$ the highest Na^+ diffusivity is found in the S1- S1-S1 structure, minimum for the random structure and S0-S0-S3 structure shows medium diffusion. The diffusivity of Na^+ is six times higher in S1-S1-S1 compared to random Si/P ordering and $3/2^{rd}$ higher from the S0-S0-S3 structure. In the case of $Na_3Zr_2Si_2PO_{12}$ the where the

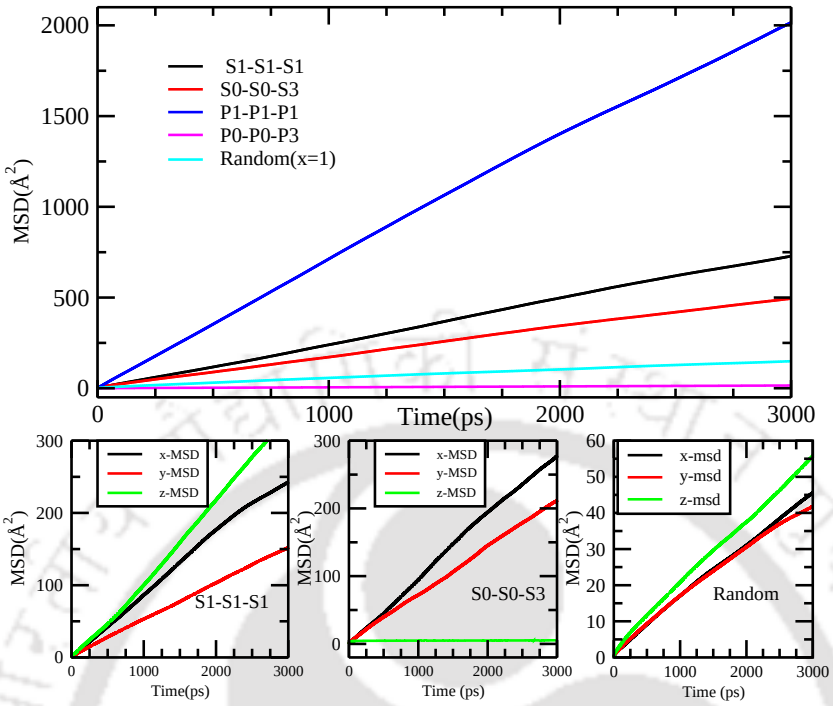

FIGURE 5.3: The mean squared displacements (MSD) of Na^+ ions with time for $Na_2Zr_2SiP_2O_{12}$ having different Si/P ordering from MD simulation at 623 K. Also shown are the corresponding MSDs for the two different Si/P orders, P1-P1-P1 and P0-P0-P3 for the $Na_3Zr_2Si_2PO_{12}$, in previous chapter 4 at 623 K. The lower panels show the MSDs resolved along the *x*-, *y*-, and *z*- directions for S1-S1-S1 and S0-S0-S3 structures.

variation in conductivity between the P1-P1-P1 and P0-P0-P3 structure is more than one order of magnitude. But in the case of $Na_2Zr_2SiP_2O_{12}$ the difference in conductivity in two ordered structures are less dramatic, quantitatively. The dc conductivity of Na^+ ions is calculated from the Nernst-Einstein relation from eqn.2.54 in chapter 2.

The conductivity of these three different Si/P ordered systems are 0.07, 0.045 and 0.01 ($S.cm^{-1}$) for S1-S1-S1, S0-S0-S3 and the random structure respectively. The conductivity of $Na_2Zr_2SiP_2O_{12}$ reported by Boilot et al. [1] is 0.0172 $S.cm^{-1}$ at 573 K. So in this structure the conductivity of random structure shows best agreement with experiment unlike the *x*=2 composition $Na_3Zr_2Si_2PO_{12}$, where the ordered strcuture P1-P1-P1 shows best agreement with experiment. The MSDs of these three structures of the *x*=1 composition, along *x*-, *y*- and *z*- directions are shown in the lower panels of figure 5.3.

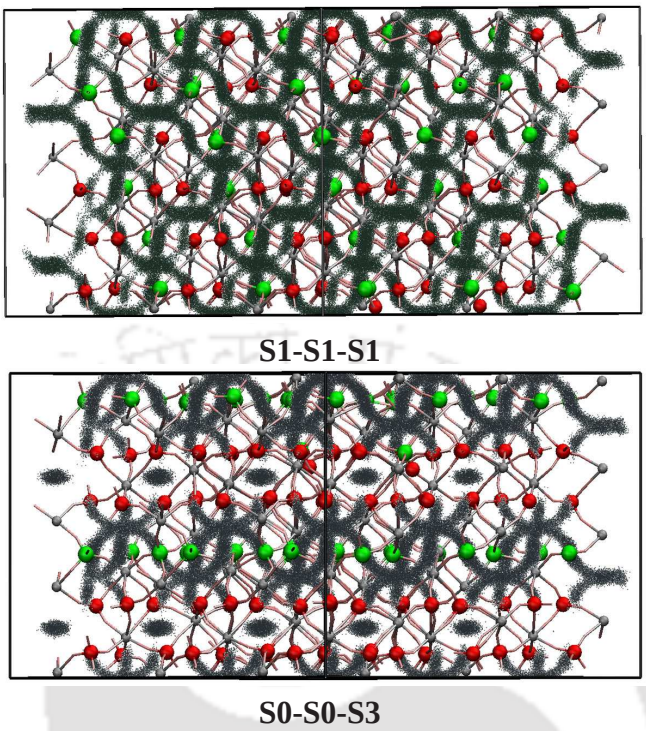

FIGURE 5.4: The three-dimensional distributions of Na^+ in the simulation cell snapshots superimposed over six nanoseconds long MD simulation of $Na_2Zr_2SiP_2O_{12}$ at 623 K. One MD configuration of the two framework structures, S1-S1-S1 (top panel) and S0-S0-S0-S3 (bottom panel), are shown in ball-and stick model (Si -green; P red; Zr grey; O not shown).

Interestingly, the MSDs calculated along the *z*- direction (identical to the *c*-axis of the rhombohedral cell), for the S0-S0-S3 structure is nearly zero, suggesting predominantly two dimensional transport of Na^+ in the framework. This is in contrast to the case of the S1-S1-S1 and random structures where the MSDs along all three axes are comparable. MSDs calculated along the *x*- axis (chosen along the *a*- axis of the rhombohedral cell), *y*- axis (chosen to lie on the *ab*-plane, 30° clock-wise to the *b*-axis of the rhombohedral cell) are comparable. We shall note in passing that, the y- component of the msd is expected to be lower than the *x*-component, by a fraction of $\cos^2 30°(= 3/4)$, as distances along *b*-direction when projected on the *y*-axis reduce by the fraction of $\cos 30°$, and MSDs involve squares of distances traversed by an ion.

Thus, the present MD simulations predict observation of two dimensional ion transport in

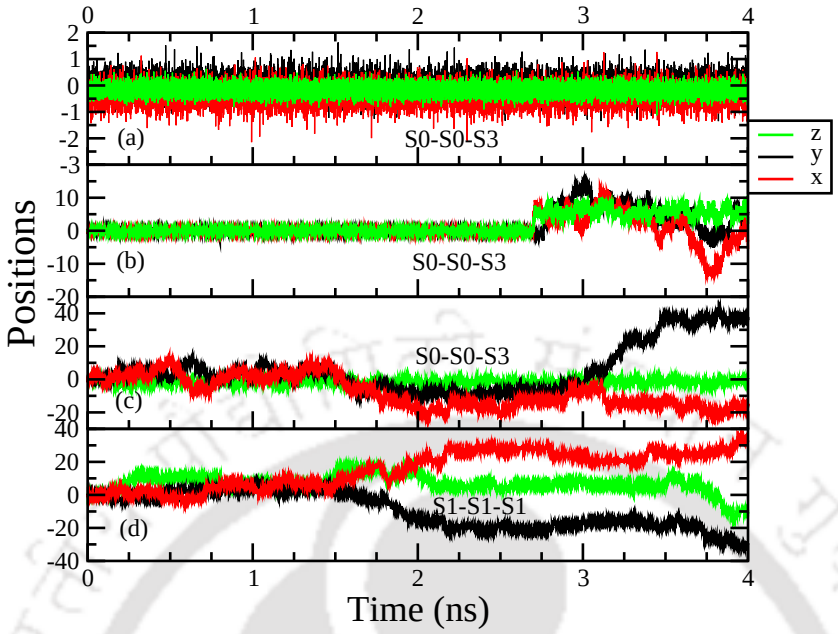

FIGURE 5.5: Variations of x, y and z co-ordinate of (a) an Na^+ ion trapped between two S0 layers of S0-S0-S3 (b) another Na^+ion from the same layer (c) Na^+ ion from the S0-S3-S0 layer of S0-S0-S3 structure. (d) Na^+ion arbitrarily chosen from S1-S1-S1 structure, plotted for the entire molecular dynamics simulation.

$Na_2Zr_2SiP_2O_{12}$ - system depending on the Si/P order in the framework. This result cautions that, though perceived isotropic for ion transport, the NASICON framework is not necessary so in general.

Detailed microscopic information related to the nature of ion transport in $Na_2Zr_2SiP_2O_{12}$ can be derived from the density and energy profiles of the Na^+ ions. Figure 5.4 has the statistical distribution of Na^+ in the simulation cell, consisting of $3 \times 3 \times 1$ rhombohedral unit cells, where coordinates of all Na^+ ions over the stored trajectory are collapsed into a single frame and visualized perpendicular to the c-axis, along with one configuration of the framework species. The Na^+ distribution for the S1-S1-S1 structure suggests well connected percolation pathways extending in all directions, and are very similar to that observed for the P1-P1-P1 structure of the $Na_3Zr_2Si_2PO_{12}$ system examined in chapter 4. Evidently, the six Na^+ migration channels originating from given a Na(1) site connecting to six neighbouring

Na(2) sites, can be seen. This explains the near isotropic nature of the Na^+ transport observed for the S1-S1-S1 structure.

The distribution for the S0-S0-S3 is most striking with bands of high and low populations of Na^+ ions stacked along the *c*-axis of the cells (figure5.4, lower panel). The bands with larger width of Na^+ populations are appearing systematically around the two Si-rich basal planes, and each extends over $c/3$ distance between two S0-basal planes (P-rich) below and above it. The high density bands include two layers of Na(1) sites each. The low density bands appear between neighboring S0-planes and include one layer of Na(1) sites which are nearly fully populated but remain largely disconnected islands of Na^+ in all three directions. On the other hand, the Na(1) sites in the high density bands are well connected with Na(2) sites on planes above and below it, forming pseudo-two-dimensional migration channels for Na^+ transport in the system. The Na^+ ions localized in Na(1) sites between the S0-planes, forms almost $1/3^{rd}$ of the total Na^+ ions in the system, and do not contribute appreciably to the average diffusivity calculated from the MSD. This accounts for the slightly lower value of overall Na^+ diffusivity in the S0-S0-S3 structure, roughly by a $2/3^{rd}$, relative to the S1-S1-S1 structure.

In figure 5.5 the variation of *x*, *y* and *z* coordinates of Na^+ ions from different bands of S0-S0-S3 structure, taken arbitrarily from S1-S1-S1 structure are shown in figure 5.5. The initial *x*, *y* and *z* co-ordinates (at t=0) of ions has been set as the origin for the convenience of plotting in all the four cases. In figure 5.5(a) the Na^+ ion taken from the Na(1) site appearing between two consecutive S0-S0 layers along *z*-axis of S0-S0-S3 structure. In this case the variation of *x*, *y* and *z* co-ordinates throughout the entire simulation is smaller less than $\approx 2\mathring{A}$ which indicates the ion is trapped in that Na(1) site and has not moved out of this band for the entire simulation the fluctuation is due to the thermal amplitudes of the ion around the Na(1) site. In figure 5.5(b) another Na^+ ion taken from an Na(1) site from the same band shows that the ion remain trapped in the Na(1) site up-to 2.75 nano-seconds after which it shows larger displacements ($20\mathring{A}$ along *z*-direction, more than the distance of the *z*-planes of two consecutive S0 layer). This indicates that the ion has jumped out of the band and moves in the

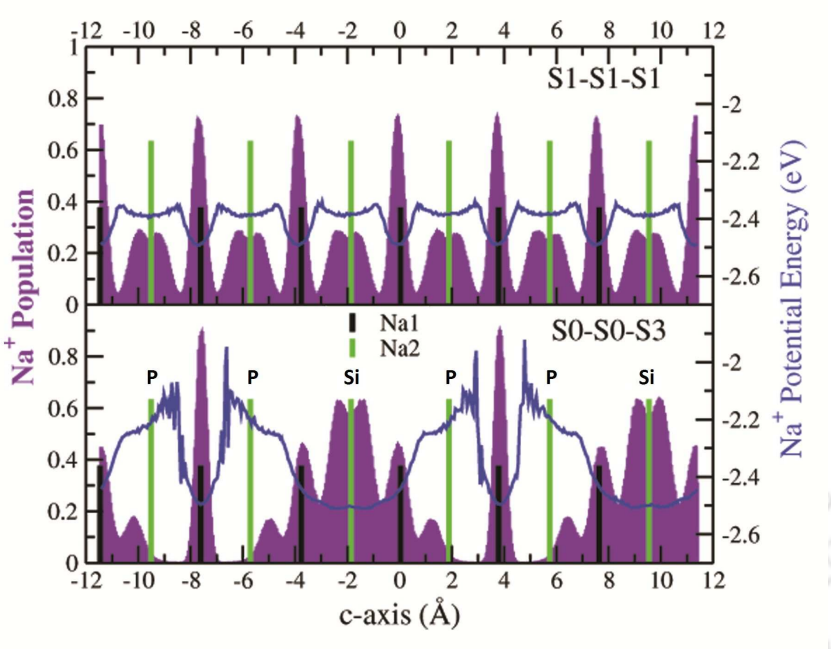

FIGURE 5.6: The potential energy profile and population of Na^+ ions along the c-axis for $Na_2Zr_2SiP_2O_{12}$having different Si/P ordering from MD simulation at 623 K. Locations of Na(1) and Na(2) sites are shown by vertical bars. For the S0-S0-S3 structure the location of P-rich (S3) basal planes are marked. The Na^+ populations are normalized to the total number of the species in the simulation cell.

conduction layer around S3. Overall it suggests that Na^+ ion from these Na(1) sites (between S0 layers) are not always trapped but it can jump out of these though very rarely. In figure 5.5(c) the Na^+ ion has been picked from the conducting S0-S3-S0 layer and the variation of its coordinates clearly shows that the movement of the ion along z-axis is restricted to $\approx 8\mathring{A}$ which is matching with the typical width of S0-S3-S0 layer along z-axis. But along x and y directions the displacements are quite higher than the z-axis which again supports that the conduction is predominantly on the x-y plane in S0-S0-S3 structure. In figure 5.5(d) the fluctuations of a Na^+ ion arbitrarily taken from the S1-S1-S1 structure is shown. It shows that the variations of all the three co-ordinates are quite higher than the other three cases discussed above. The net displacement along the three different directions are quite similar in this case unlike in the previous case of the S0-S0-S3 structure. This fact demonstrates that the ionic conduction in S1-S1-S1 structure is isotropic while that of S0-S0-S3 structure is anisotropic.

The potential energy profile of Na^+ ions moving in the interstitials of the framework helps identifying the microscopic energy barriers for ion transport in the system. The energy profile of the i^{th} ion due to its interaction with all the other ions in the system is computed similarly through the eqn. 4.2 in chapter 4. The energy profile with respect to their *z*-coordinates, averaged over the stored trajectory from MD simulation at 623 K, is shown in figure 5.6. The potential energy profile for the S1-S1-S1 structure is relatively flat with the minima appearing at Na(1) and Na(2) sites. The energy of Na(1) site is observed to be lower by about 0.1 eV relative to Na(2) site, and a barrier of about 0.15 eV can be estimated from figure 5.6. The width of the basins at Na(1) and Na(2) sites are in agreement with the corresponding breadth of Na^+ distribution at these sites along the *c*-axis (see figure 5.4). The energy profile for the S0-S0-S3 structure has large barriers along the *c*-axis, with a twin-maxima appearing between the P-rich (S0) basal planes, and a deep minimum at the centre coinciding with Na(1) sites encompassed by these P-rich planes. The near full occupancy of these Na(1) sites impose large barriers (due to Na^+ -Na^+ -repulsion) to the oncoming Na^+ ions, preventing long range transport of Na^+ along the *c*-axis. The broader basin observed around the Si-rich (S3) planes essentially constitutes the pseudo two-dimensional conduction channel along the *ab*-plane. The appearance of a few well defined peaks in the Na^+ density in the absence of well defined minimam in energy, suggests that the broad-shallow nature of basin is a result of dynamical smoothening due to significant Na^+-Na^+ correlations.

The Na^+ conduction channel in the S0-S0-S3 structure is visualized in figure 5.7, where a cross section of Na^+ population (in arbitrary scale) on the *ab*-plane corresponding to one of the two dense bands in a unit cell (refer to figure 5.4, as well) is shown. The population includes all Na^+ ions in a slab of 5.1 $\AA$ thickness, that covers the Na(2) sites on the Si-rich basal plane and Na(1) sites above and below this basal plane. The path ways from Na(1) to the terminating Na(2) sites on the P-rich planes (figure 5.4), which do not contribute to long range ion transport, are also visible. The well integrated network of Na^+ population on the *ab*-plane accounts for the long- range motion of Na^+ in the S0-S0-S3 structure. Thus the topology of the Na^+ channel in this structure can be described by, (1) Na(2)/S3 ↔(2) Na(1)/Si-P ↔ (3)

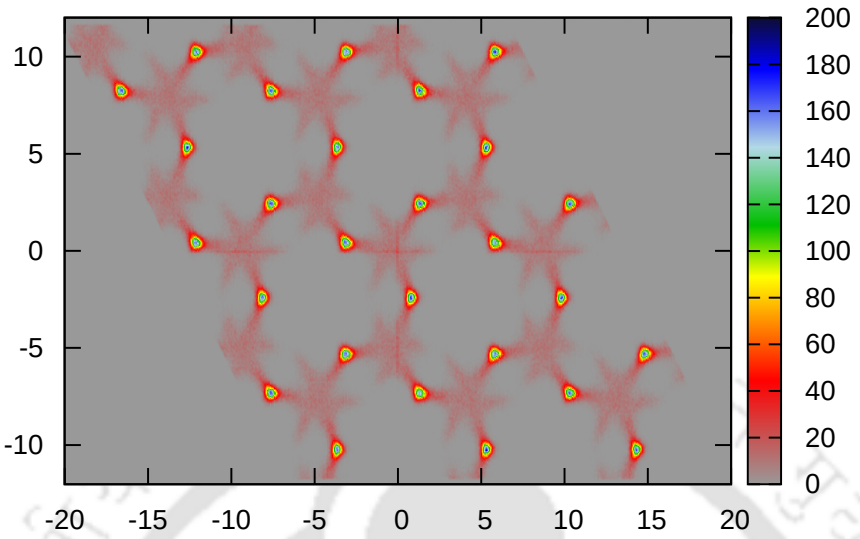

FIGURE 5.7: Population of Na^+ (in arbitrary scale) on the ab-plane from a slab of 5.1 $\AA$ thickness around the Si-rich plane demonstrates the migration pathway of ions in S0-S0-S3 structure. The locations of high Na^+ population correspond to the Na(2) sites and the tri- junctions are the Na(1) sites.

Na(2)/S3, meaning, every Na(2) site on Si-rich plane is connected to two Na(1) sites at the interlayer of Si and P rich planes that is connected to three Na(2) sites on Si-rich plane.

5.1.3 Conclusions

Molecular dynamics (MD) simulations of $Na_2Zr_2SiP_2O_{12}$ having three different Si/P orders highlights significance of the interaction between mobile species with the framework cations. The nature of Na^+ transport in $Na_2Zr_2SiP_2O_{12}$ is found sensitive to the Si/P order present in the framework owing to the increases in the coloumbic repulsion of Na^+ with P^{5+} relative to Si^{4+}. Interstingly, the framework with Si-rich basal planes sandwitched between two P-rich planes, stacked along the *c*-axis favours two dimensional conduction along the basal plane, while a “uniform” distribution of Si/P along the *c*-axis as well as the random distribution of

Si/P results nearly isotropic transport of Na^+. The topology of the Na^+ channel in the S0-S0-S3 structure is, Na(2)/S3 ↔(2) Na(1)/Si-P3 ↔ Na(2)/S3, where an Na(2) site on Si-rich plane is connected to two neighboring Na(1) sites above and below it, that is connected to three Na(2) sites on Si-rich plane. While there are no direct experimental evidence pertaining to Si/P order in NASICON frameworks, the variance in conductivity and activation energies across previous experimental reports, in the light of these molecular dynamics studies, suggests that the Si/P order is likely to be sensitive to synthesis roots and heat treatment of samples. The conductivity dependence on the order of framework cations, predicted in molecular dynamics studies, is expected to be a general phenomena, particularly in aliovalently substituted fast ion conductors. This effect will be important in the design and fabrication of energy materials, and calls for more experimental and theoretical efforts.

Bibliography

[1] J.-P. Boilot, G. Collin, and P. Colomban, J. Solid State Chem. **73**, 160 (1988).

[2] J. Boilot, G. Collin, and P. Colomban, Mater. Res. Bull. **22**, 669 (1987).

[3] D. T. Qui, J. Capponi, J. Joubert, and R. Shannon, J. Solid State Chem. **39**, 219 (1981).

[4] H. Kohler, H. Schulz, and O. Melnikov, Mater. Res. Bull. **18**, 1143 (1983).

[5] H.-P. Hong, Mater. Res. Bull. **11**, 173 (1976).

[6] U. Von Alpen, M. Bell, and W. Wichelhaus, Mater. Res. Bull. **14**, 1317 (1979).

[7] P. Colomban, Solid State Ionics **21**, 97 (1986).

[8] P. P. Kumar and S. Yashonath, J. Am. Chem. Soc. **124**, 3828 (2002).

[9] P. P. Kumar and S. Yashonath, J. Phys. Chem. B **106**, 7081 (2002).

[10] M. P. Allen and D. J. Tildesley, *Computer simulation of liquids*, Oxford university press, 1989.

Chapter 6

Conclusion

The phenomenon of fast ion transport in solids forms one of the thrust areas of current day research owing to its potential applications in materials for energy storage and conversion. As reviewed in Chapter 1 of the thesis significant progress have been achieved in the field in the last two decades and varieties of promising matrices having good ionic conductivities have been realized. It is, however, very important to gain microscopic understanding of the mechanism of fast ion transport and factors that influence the phenomena for the further advancement of the field. Atomistic computer simulation techniques outlined in Chapter 2 of the thesis are, for example, among some of the most power tools to gain such insights on this phenomenon. The thesis reports fresh insights on structure and ion transport in one of the potential family of fast ion solids, namely NASICONs, based on these atomistic simulation techniques. Atomistic computer simulation studies employing previously reported interatomic potential[1, 2] have been carried out on the three compositions of the NASICON series $Na_{1+x}Zr_2Si_xP_{3-x}O_{12}$ ($x = 0,\ 1$ and 2). The structural response of the $x = 0$ composition $MZr_2P_3O_{12}$, varying different alkali ions, $M = Li^+, Na^+, K^+, Rb^+$ and Cs^+ are investigated over a wide range of temperatures (300- 900 K) using isothermal isobaric Monte Carlo (NPT-MC) simulations. The insertion of the larger alkali ion M results increment in the *c*-parameter

and decrement of the *a*- parameter of the unit cell across the series of substitution. The variation of *c*-parameter shows excellent agreement while for the *a*- parameter the agreement is qualitative with previous experiment [3].

Zr-O and P-O bond lengths do not show any significant changes across the series in the entire temperature range. Significant increase in the MO_6 octahedra at the 6*b* site is observed, with the size of the alkali ion, *M*. The gross variations in lattice parameters could be explained qualitatively within the Alamo's structural model involving coupled polyhedral rotations[5, 6]. However, the present simulation results, which are better quantitative agreement with experiments, do not support the "rigid polyhedra" assumption invoked in Alamo's model.

Our simulation results suggest that the distortions of the polyhedra contributes about $1/3^{rd}$ of the observed change in lattice parameters. Our simulation study also shows that the variations of lattice parameters with temperature follow the similar pattern though less intense, as for the insertion of larger cations. The larger thermal amplitudes of the alkali ion create more pressure on the framework and thus effect the lattice variations similar way as for the larger cation size. In his experiment Colomban proposed the influence of the nature of the polyhedral rotations on thermodynamic properties of these system. In the present study nature of the polyhedral rotations are found to be dynamic in nature and further theoretical investigations needed in this point.

It is also noted that entire temperature range (300 - 900 K), the alkali ions remain populated at the M(1) sites (6*b* sites of $R\bar{3}c$) which reflects "non-diffusive" nature of the alkali ions in these systems, except for Li^+ system at higher temperatures above 600 K, for which some population are present at Na(2) sites (18*e* sites of $R\bar{3}c$) also, mimics alkali ion "conduction" in the system. The conducting nature of Li^+ system is in qualitative agreement with the experiment reported earlier by Petit et al [4].

Molecular dynamics (MD) studies on the $x = 2$, $Na_3Zr_2Si_2PO_{12}$, composition reported in Chapter 4 highlight the significance of Si/P ordering on the Na^+ conductivity in the system. Due to the similar sizes of silicon and phosphorous, the X-ray have not distinguished their

exact locations across the 18*e* crystallographic positions[7]. The MD studies carried out with different Si/P ordering in the frameworks, predicts over one order of magnitude change in ionic conductivity, among them. These observations are in agreement with potential energy profiles of Na^+ calculated for these structures. The high conducting framework offers low-barrier migration pathways for Na^+ and the three dimensional distribution of the ions were more spread out in the unit cell. Evidence that the Na^+ ions prefer to move away from the P^{5+} ions of the framework is provided; which suggest that the Coulombic interactions are responsible for the observed conductivity variation across frameworks with different Si/P orders. This effect is proposed to be one of the reasons for the large scatter in the experimentally measured conductivities.

The Si/P arrangements can also influence the activation energy behavior of this material. NPT-MD simulations are carried out to study the activation energy of $Na_3Zr_2Si_2PO_{12}$ in the temperature range of 300 - 800 K for different Si/P arrangements. The framework structure having ordered Si/P arrangements shows sharp changes in the slope of Arrhenius plot of conductivities around 500 K. This behavior is qualitatively similar with the high temperature sintered material reported in Colomban's experiment [8]. On the other hand the framework with randomly distributed Si/P shows a single activation energy without any significant change in the Arrhenius plot for the entire temperature range (300 K- 800 K) and thus behaving similarly with the low temperature sintered samples reported by Colomban [8]. Thus present simulation studies predicted that the different sintering temperature can control the Si/P ordering of the material and consecutively conductivities. The polyhedra for all the Si/P arrangements show dynamical disorder at higher temperatures 500 K and the role of this on the conductivity of the materials needed further experimental and theoretical investigations.

Motivated by the above findings the study has been extended to the $x = 1$ composition $Na_2Zr_2SiP_2O_{12}$. MD simulations on the different Si/P-ordered structures, only small changes in the overall conductivities. However, evidence for highly anisotropic, two-dimensional transport is evidenced for certain Si/P ordered structures. This planar conductivity is a surprising effect for NASICON-type structures, which are well known to have three-dimensional

ion channels. Again, the difference in the strength of Coulombic interaction of Na^{+} with P^{5+} and Si^{4+} is found responsible for the effect. Thus the effect of cationic ordering of framework ions on ion transport is verified within the NASICON family.

The most important findings in the present thesis is a new structural feature (Si/P ordering) which has a significant influence on the ion transport in the NASICON family of solids. The reason of this has been traced back to the stronger columbic repulsion between P^{5+}-Na than Si^{4+} -Na. It is expected that this effect will be present on the other fast ion conductors having aliovalent substitutions, though with varying tenacity. The variations of conductivity and activation energies across the different Si/P ordering from these molecular dynamics studies, when compared with the similar results from the Colomban's experiment it can be concluded that different sintering temperatures are having an profound effect on the Si/P arrangement present on these systems though no direct experimental evidence is available. This phenomenon thus vary significant beyond NASICON family in understanding of fast ion transport in solids and their tailor making. This effect carries importance in design and fabrication of energy materials and calls for more experimental and theoretical efforts.

Bibliography

[1] P. P. Kumar and S. Yashonath, J. Am. Chem. Soc. **124**, 3828 (2002).

[2] P. P. Kumar and S. Yashonath, J. Phys. Chem. B **106**, 7081 (2002).

[3] D. Agrawal, C.-Y. Huang, and H. McKinstry, Int. J. Thermophys. **12**, 697 (1991).

[4] D. Petit, P. Colomban, G. Collin, and J. Boilot, Mater. Res. Bull. **21**, 365 (1986).

[5] G. E. Lenain, H. A. McKinstry, J. Alamo, and D. Agrawal, J. Mater. Sci. **22**, 17 (1987).

[6] J. Alamo, Solid State Ionics **63**, 547 (1993).

[7] J.-P. Boilot, G. Collin, and P. Colomban, J. Solid State Chem. **73**, 160 (1988).

[8] P. Colomban, Solid State Ionics **21**, 97 (1986).